Magnetic Optical Scatterers and Backaction

Andrej Kwadrin

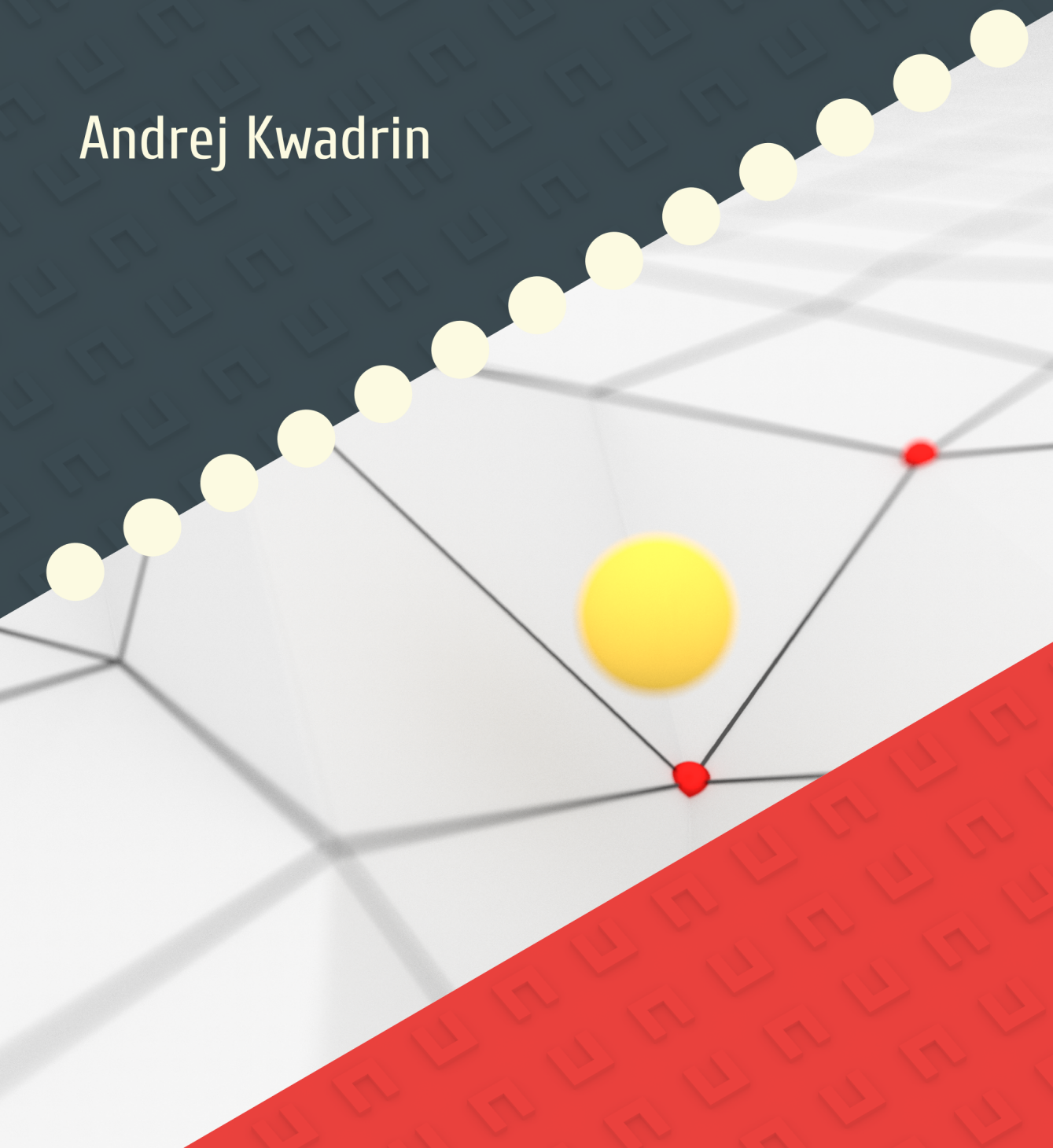

Magnetic optical scatterers and backaction

Ph.D. thesis University of Amsterdam, September 2014
Magnetic Optical Scatterers and Backaction
Andrej Kwadrin

ISBN/EAN: 978-90-77209-86-8

A digital version of this thesis can be downloaded from
http://www.amolf.nl.

Magnetic optical scatterers and backaction

ACADEMISCH PROEFSCHRIFT

ter verkrijging van de graad van doctor
aan de Universiteit van Amsterdam
op gezag van de Rector Magnificus
prof. dr. D. C. van den Boom
ten overstaan van een door het college voor promoties
ingestelde commissie,
in het openbaar te verdedigen in de Agnietenkapel
op woensdag 10 september 2014, te 12.00 uur

door

Andrej Kwadrin

geboren te Dresden in Duitsland

Promotor:	prof. dr. A. F. Koenderink
Overige leden:	prof. dr. H. Bakker dr. M. P. van Exter prof. dr. M. S. Golden prof. dr. H. B. van Linden van den Heuvell prof. dr. C. Rockstuhl

Faculteit der Natuurwetenschappen, Wiskunde en Informatica

The work described in this thesis is part of the research program of the
"Stichting voor Fundamenteel Onderzoek der Materie (FOM)"
which is financially supported by the
"Nederlandse Organisatie voor Wetenschappelijk Onderzoek (NWO)".

This work was carried out at the
Center for Nanophotonics,
FOM Institute AMOLF,
Science Park 104, 1098 XG Amsterdam, The Netherlands,
where a limited number of copies of this dissertation is available.

Contents

1 Introduction **7**
- 1.1 Refractive index . . . 8
- 1.2 Effective media and metamaterials . . . 9
- 1.3 Local density of optical states . . . 12
- 1.4 Motivation and thesis outline . . . 16
- 1.5 References . . . 19

2 Calibrating radiative and nonradiative decay constants of fluorophores **23**
- 2.1 Introduction . . . 24
- 2.2 Gray-tone lithography . . . 26
- 2.3 Wedge profile characterization . . . 28
- 2.4 Preparation of fluorophores . . . 30
- 2.5 Experiment . . . 31
- 2.6 Results . . . 32
- 2.7 Conclusions and outlook . . . 38
- 2.8 References . . . 40

3 Probing the electrodynamic LDOS with magnetoelectric point scatterers **45**
- 3.1 Introduction . . . 46
- 3.2 Magnetic LDOS near metallic and dielectric interfaces . . . 47
- 3.3 Green function . . . 49
- 3.4 Radiative linewidth near an interface . . . 51
- 3.5 Magnetoelectric LDOS . . . 54
- 3.6 Finite element modelling example . . . 58
- 3.7 Conclusion . . . 59
- 3.8 References . . . 61

4 Diffractive stacks of metamaterial lattices **65**
4.1 Introduction 66
4.2 Starting point: 2D lattice-sum theory 67
4.3 Complex base and stacks of 2D layers 70
4.4 Diffractive calculation 72
4.5 Fourier microscopy setup 74
4.6 Diffraction measurement 75
4.7 Angle-resolved transmission and pseudochirality 77
4.8 Stacked lattices 82
4.9 Conclusion 82
4.A Lattice sum 83
4.10 References 85

5 Backaction on a lattice of scatterers in front of a reflective interface **89**
5.1 Introduction 90
5.2 Theory 91
5.3 Results 93
5.4 Experiment 104
5.5 Conclusion 106
5.6 References 108

Summary **109**

Samenvatting **113**

Acknowledgments **117**

Chapter 1

Introduction

To predict and explain the propagation of light through a medium, one particular quantity plays a major role: the mediums' refractive index. As the first section of this chapter shows, its value, and how refractive index is spatially distributed is omnipresent in the explanation of a plethora of optical phenomena. How a refractive index comes about in natural materials is usually discussed in terms of the underlying response of the mediums' constituent polarizable atoms to impinging electromagnetic waves. In the last decade, a new field of 'metamaterials' emerged, in which unconventional effective medium responses are generated by nanostructured 'meta-atoms'. This thesis studies metamaterials in the near field through a quantity called 'local density of optical states' (LDOS). In the second section of this Chapter, we introduce the reader to the concept of the LDOS and its universal role in phenomena such as fluorophore emission and light scattering. Based on both concepts, we end by giving a motivation and outline of the topics covered within this thesis.

1.1 Refractive index

This thesis is set in a field of physics that is called 'nanoscale-optics'. Optics is the branch of physics that deals with light, i.e., how light is emitted, how it propagates from A to B, and how it is absorbed. Optics, however, really is as much about matter as it is about light. Indeed, solutions of Maxwell's equations in vacuum are simply unconfined plane waves that exhibit rectilinear propagation [1]. For useful phenomena to occur, such as reflection and refraction of rays in a lens, image formation in a camera, guiding of light in a telecommunications fiber, or the appearance of diffraction orders in a spectrometer, light must interact with polarizable matter. In particular, the material parameter that enters the problem is usually introduced in textbooks through the concept of refractive index [2]. To describe and predict the propagation of light one naturally follows the concept of rays traveling in straight lines from A to B, experiencing refraction as a ray traverses from one medium to the next. The key parameter describing the process, as formulated by Snellius in the 17th century is, in the simplest case, a single real-valued quantity: the refractive index $n \equiv c/v$ defined as the ratio of the light's speed in vacuum c and its speed in the medium v [3].

The concept of refractive index turns out to be an exceptionally powerful simplification of the processes taking place. In fact, electric and magnetic fields that are oscillating in time and space interact with large amounts of atoms, typically 10^{23} in a cm^3 for a solid, that each have many degrees of freedom [4]. Yet the behavior of light is very well described by just one effective parameter for the medium, namely n. Delving somewhat deeper into electrodynamics it turns out that it would be more appropriate to say that one deals with the effective medium parameters 'dielectric permittivity' ε and 'magnetic permeability' μ [5]. To show the wealth of phenomena that the concept of effective medium parameter, or refractive index, explains, just consider that by lumping all the degrees of freedom of a material in one parameter, the making of layers, powders, fibers, etc. is sufficient to describe lensing, scattering, why clouds, paint and snow appear white, why one should buy polarizing sunglasses, the colorful reflection of opals and oil films, interference filters, etc. In fact, if one adapts the refractive index to be dispersive in frequency, or to be a tensorial quantity depending on propagation direction and polarization, one can extend its validity to deal with more complex materials such as metals and birefringent crystals [3].

The only two regimes where the effective medium approach is taken to break down is when either features in the material distribution become atomic in size, so that quantum confinement corrections set in [6], or when electric fields strengths are so large that nonlinear responses occur [7]. A range of interesting phenomena appear, such as harmonic generation, and

the optical Kerr effect which both are based on an intensity dependent refractive index. However, throughout this thesis, we will work in a regime where a material's response to electromagnetic radiation depends linearly on the electromagnetic-field strengths. As a consequence, our chosen material parameters will not depend on the intensity of the light field. Furthermore, we note here that throughout this thesis light-matter interaction is treated in the classical (non-quantum) sense.

Microscopically, the overall response of a medium to electromagnetic radiation stems from the combined responses of the materials' individual constituents, e.g., molecules of a gas or atoms of a solid dielectric described by their polarizability or electrons of a metal explained by a Drude model [8, 9]. For instance, the simplest textbook description of the permittivity of a crystalline insulating material would read

$$\varepsilon = 1 + \rho\alpha \tag{1.1}$$

where ρ is the number density of atoms, and α is their *polarizability*, a number with units of volume, which quantifies how large a dipole moment is induced per unit strength of incident electric field. We refer to Jackson [1], Chapter 4 for further treatments of microscopic formulas to approximate ε. Based on this logical assumption, it is valid to ask when it is feasible to cover such an 'effective' response in a single quantity such as a refractive index. Surely, to be able to give a reasonable answer one has to assess and compare the characteristic length- and time-scales of the wave phenomenon of electromagnetic energy propagation to the characteristic values of the medium under investigation. In the optical regime, the typical wavelength of light is a μm, which is more than three orders of magnitude larger than the typical spacing of atoms in a crystal. It should be noted how in nature, at optical frequencies materials have an electric response ε, which could be either positive or negative, and no magnetic response, i.e., $\mu = 1$ as in vacuum. At this point it is interesting to summarize effective material parameter ranges available in nature in Fig. 1.1, a.

1.2 Effective media and metamaterials

Historically, there has been a large interest to extend the idea of an effective response also to nanostructured composites. In particular, suppose you create a mixed topology, such as by etching air holes in a solid material to obtain a nanoporous sponge, or when putting colloids in a liquid, then a logical question is how you estimate the refractive index of the mixture from that of the constituents. Since the separation of length scales is absent, an improved approach is required. Specifically, Bruggeman [10] and Maxwell-Garnett [11] have derived expressions for the effective refractive index of

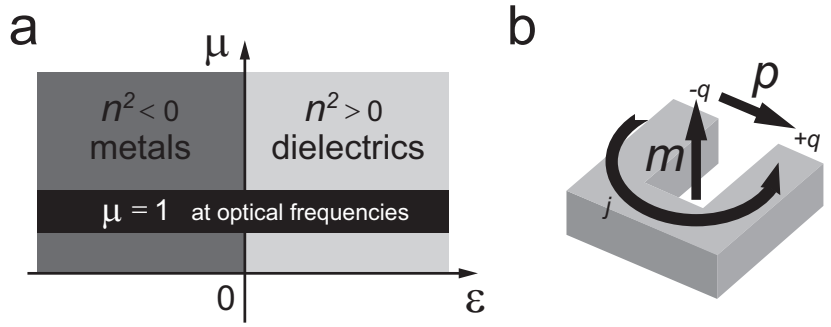

Figure 1.1: (a) Natural materials cover a range of permittivities ε and permeabilities μ. At optical frequencies, the permeability is limited to $\mu = 1$. Dielectric polarization allows for positive ε, while metals offer negative ε for frequencies below their respective plasma frequency. Therefore, the squared refractive index $n^2 = \varepsilon\mu$ can either be positive or negative, corresponding to transparent media, respectively, media in which propagation is exponentially damped. (b) An archetypical meta-atom is the split ring resonator (SRR). When being driven at the SRR's resonant frequency, charge separation ($\pm q$) along the split gives rise to an electric dipole moment $\boldsymbol{p}$. In turn, a circulating current $\boldsymbol{j}$ give rise to a magnetic dipole moment $\boldsymbol{m}$, pointing out of the SRR plane.

mixtures of materials, for instance often used to predict the optical properties of powders and suspensions. For instance, the simplest effective medium theory would estimate the effective permittivity of a composite simply by averaging as

$$\varepsilon = \varepsilon_1\phi + \varepsilon_2(1-\phi) \tag{1.2}$$

where ϕ is the volume fraction of material of permittivity ε_1, with the remaining material having permittivity ε_2. This approach is equivalent to simply adding up the polarizabilities of constituents in vein of Eq. 1.1. Evidently, this would be a poor approximation for some topologies. For instance for a nanoporous metal film, you would expect a response that strongly depends on whether the metal forms a conductive percolating network or not, meaning that a dielectric host with metal inclusions would be very different from its inverted counterpart. Maxwell-Garnett's formula

$$\varepsilon_{\text{eff}} = \varepsilon_m \frac{2(1-\phi)\varepsilon_m + (1+2\phi)\varepsilon_i}{(2+\phi)\varepsilon_m + (1-\phi)\varepsilon_i} \tag{1.3}$$

is an example of a mixing formula that treats isolated inclusions (volume fraction ϕ, permittivity ε_i) very differently from the backbone ε_m. However,

note that since these are all averaging formulas, taking volume-fraction averages, these composites are always predicted to have ε between those of the constituents, hence being constrained to the same range of refractive index values as achievable with unstructured materials.

In 1967, Veselago discussed the intriguing consequences of being able to utilize media with effective material parameters outside those available in nature [12]. Since the year 2000, many efforts have been devoted to make structures that appear to respond as if they are effective media with ε and μ far from that of their constituents, in particular having μ different from one [13, 14, 15, 16, 17]. The central paradigm has been to generate so called meta-atoms that are subwavelength sized metallic resonators that have a resonant response that involves oscillating charge distributions (Fig. 1.1, b). If these oscillations include a circulating component, an effective magnetic dipole moment is set up. Most meta-atoms are hence loop-shaped particles with a gap that present an LC-resonance owing to the inductance of the loop and capacitance of the gap. The LC-resonance means that each building block has a very large polarizability α, compensating for the low density ρ of objects. Moreover, the resonant response embodied in α can be both positive and negative, depending on how the driving frequency is chosen relative to the LC-resonance frequency. Thereby, sizeable changes in permittivity and permeability can be achieved, with values outside the scope of traditional averaging formulas. In this way, optical magnetism was reported even at visible wavelengths [18, 19, 20].

A key question is how valid the assignment of parameters ε and μ is for structures accessible in experiment. Naturally, it is evident that a system with length scales exceeding the characteristic wavelength will diffract, and have grating orders. Thereby, it will not be 'effective'. However, suppose a reflection/transmission measurement on a slab of material would tell us that it appears to be an effective medium. Are the same retrieved parameters then valid for all possible measurements, e.g., for incidence under any angle? This question has triggered a revisiting of theories of homogeneous media, in particular examining in how far the response of metamaterials can be captured as spatial dispersion in ϵ [21]. And supposed that a metamaterials' response in any far-field experiment can indeed be parametrized — through possibly tensorial effective dielectric and magnetic constants, in which experiments is it then discernibly *not* an effective medium. In particular, one expects that when one moves a probe to within a wavelength distance, comparable to the meta-atom size, effective medium parameters must break down. Exactly how this cross over occurs is highly interesting. The philosophy of this thesis is to address this question in the near field. As the key concept in this region, we will employ the local density of optical states which we introduce in the following section.

1.3 Local density of optical states

Processes in nature which involve the conversion of the energy light 'carries' to change the state of an interacting piece of matter are manifold. One particularly relevant phenomenon is the process of photoluminescence [22]. An electron in the ground state of an atom, quantum dot, molecule, or impurity in a solid, might be promoted to an excited state in its energy level scheme, for instance by absorption of an incident photon or electrically as occurs in a LED. Relaxation to a lower-energy state via the re-emission of a photon can happen on different timescales depending on the probability of this high- to low-level electronic energy state transition to take place. A likely transition between two singlet states happens on the typical timescale of nanoseconds and is termed fluorescence. A much less likely spin-forbidden transition from a triplet to a singlet state happens on timescales of milliseconds, and is termed phosphorescence. This difference in timescale indicates that the transition probability per unit of time depends on the excited state and final state electronic wave functions, and in particular on their overlap as embodied in the dipole matrix elements. It should be realized that the process of photon absorption can be considered as instantaneous as it is orders of magnitude faster (typically 10^{-15} s) than the relaxation process.

The time scale of the relaxation process does not solely depend on the transition-dipole matrix elements of the involved electronic wave functions of the emitting object. The environment 'into' which the photon is released is of equal importance as transition probabilities incorporate not only the objects' electronic level scheme, but also the available photonic states of the environment into which the photon can be released [23]. Transition rates for dipolar transitions from an initial state $|i\rangle$ to a final state $|f\rangle$ can be deduced from Fermi's Golden Rule

$$\gamma = \frac{2\pi}{\hbar^2} \sum_{|f\rangle} \left| \langle f | \, \hat{\mu} \cdot \hat{\mathbf{E}} \, | i \rangle \right|^2 \delta(E_f - E_i) \tag{1.4}$$

which sums matrix elements of the product of transition-dipole operator $\hat{\mu}$ and radiation-field operator $\hat{\mathbf{E}}$ over all available final states under conservation of energy represented by the δ-term. The final state $|f\rangle$ encompasses the fate of both the fluorophore, ending up in a lower energy ground state, as well as the radiation field, now carrying an additional photon emitted from the fluorophore, after the transition process. All relevant information about the fluorophore is found within the electronic structure and wave function, i.e., the knowledge of excited and ground state energies separated by an energy difference of $\hbar\omega$. However, the sum of Eq. 1.4 has to be carried out taking all available final states of the radiation field (with an additional photon of energy $\hbar\omega$) into account as well. Particularly in the context of

so-called 'photonic crystals', a field developed in the late 1990's and early 2000's, it was realized that the availability of final states for the photon, as counted by $\delta(E_f - E_i)$ can be strongly modified and even completely suppressed over large frequency bands [24, 25, 26]. Moreover, this availability of modes should not just count if a mode exists in the system (as embodied in the density of states), but also how strong each mode is at the location of a fluorophore. A canonical example is that of an emitter in a microcavity, where it is evident that coupling of the fluorophore to the cavity requires precise alignment with the cavity mode field maximum [27, 28, 29, 30]. This can be summarized by formulating the fluorescence transition rate as a quantity depending on transition-matrix elements μ and a spatially dependent quantity called the local density of optical states (LDOS) $\rho(\mathbf{r}, \omega)$ fully characterizing the fluorophore's environment [23]

$$\gamma = \frac{\pi\omega}{3\hbar\varepsilon_0} |\mu|^2 \rho(\mathbf{r}, \omega). \tag{1.5}$$

The optical LDOS has been exploited in three ways. First, in particular photonic systems a controlled variation of LDOS $\rho(\mathbf{r}, \omega)$ can be generated, which allows to quantify the photophysics of an unknown fluorophore simply by varying its position in the LDOS landscape [31, 32, 33, 34, 35, 36, 37]. Second, if one has known fluorophores one can use them to map the LDOS of an unknown photonic system by measuring decay rate as a function of $\mathbf{r}$ and ω [38, 39, 40, 41]. Third, for the fabrication of efficient single-photon sources and quantum-optics devices, there is a large demand for controlled engineering of $\rho(\mathbf{r}, \omega)$ in order to ensure that an emitter couples selectively to a given mode, in order to completely control how fast a photon is emitted after excitation, and in order to reach strong light-matter interaction [42]. We will now review the first two of these three uses.

Monitoring the influence of a non-uniform environment on the fluorescence behavior of an emitter allows one to calibrate the emitters' fluorescence properties. Indeed, a common question when desiring to quantify an unknown fluorophore is what its quantum efficiency and oscillator strength (embodied in μ) is. A non-unity quantum yield comes about when the excited state has a nonradiative decay channel (decay rate γ_{nonrad}) in addition to the radiative decay, for instance due to the generation of phonons, i.e., heat. Since the nonradiative decay does not involve a photon it has a rate independent of the photonic mode structure, meaning that the total fluorescence decay rate one would measure in a fluorescence decay-rate measurement that maps intensity $I(t) = I_0 \exp(-\gamma t)$ is

$$\gamma = \gamma_{\text{nonrad}} + \rho(\mathbf{r}, \omega)\gamma_{\text{rad}}. \tag{1.6}$$

The first experimental realization of this approach by Drexhage et al. [43] studied the fluorescence lifetime of europium ions as a function of the dis-

tance to a silver mirror and showed that solely the radiative decay rate of the emitter was affected by the environment, leaving the nonradiative decay rate unchanged. Knowledge of both decay rates allows for quantitative assessment of the fluorescence process in the form of an intrinsic quantum efficiency. This approach lent the name to a plethora of Drexhage-type experiments and the study of fluorophores [31, 32, 33], quantum dots [34], nitrogen vacancy centers [35, 36] in diamond and magnetic dipole transitions [37]. Figure 1.2 shows the decay rate enhancement Γ compared to vacuum LDOS for a dipole oriented perpendicular and parallel to a perfect mirror ($\varepsilon = -\infty$).

Furthermore, the same qualitative effect of the environment's LDOS is found in the scattering properties of plasmonic particles (introduced in the previous section). If one has a plasmonic scatterer of sufficient size (radius above 20 nm), it is a resonant polarizable object that has as dominant loss channel radiation of its excitation as scattered light into the far field. Since the LDOS modifies the number of channels available to radiate into, one expects that the radiation damping of a scatterer varies as a function of LDOS. Indeed Buchler et al. [44] showed that a plasmonic particle's extinction cross section linewidth plotted as a function of particle-mirror distance follows an LDOS lineshape. This effect of a mirror on the scattering properties of a plasmon particle can be viewed as a backaction, whereby the particle is not only driven by an incident field, but also by its own mirror image. This backaction essentially renormalizes the particle's polarizability tensor. In contrast to the transition-dipole picture in the fluorophore case, here, the radiation of externally driven dipole(s) (spatial charge separation in the classical sense) is affected by the presence of a mirror, again allowing for characterization of the radiating dipole(s) quantum efficiency and the particle's plasmon spectrum.

Turning to the second exploitation of LDOS, once one has full knowledge of the behavior of an emitter embedded in a homogeneous reference medium (for simplicity: vacuum) allows one to use this characterized emitter as a reference probe. Bringing such an emitter in proximity to an unknown, possibly inhomogeneous and therefore more intricate structure, one can map the LDOS in the structures' surrounding. Examples range from the study of plasmonic nanowires with scanning tips featuring fluorescent molecules [38] or nitrogen vacancy centers [39] to the complete mapping of photonic crystals with quantum dots [40] and mode structure analysis of photonic cavities by cathodoluminescence spectroscopy [41].

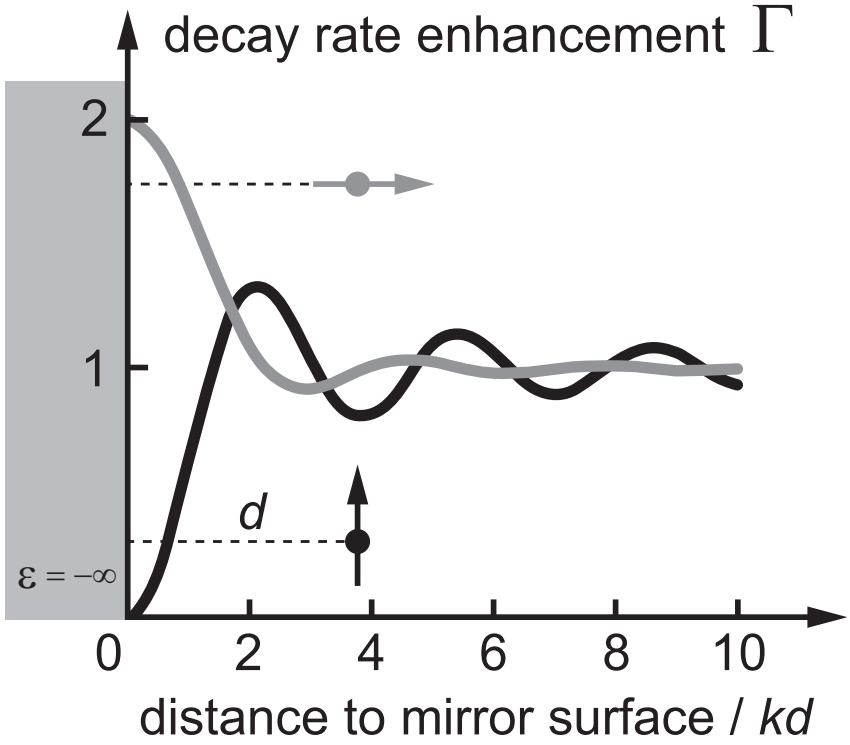

Figure 1.2: A radiating dipole separated from a perfect mirror ($\varepsilon = -\infty$) at a geometrical distance d will experience a decay rate enhancement Γ (compared to the dipole in vacuum) depending on the dipole orientation. We plot Γ for two particular dipole orientations with distances presented in units of wavenumber×distance: kd. A dipole oriented parallel to the mirror surface experiences a total inhibition of its radiative decay when touching the mirror surface (black). In contrast, a dipole oriented perpendicular to the mirror surface experiences a decay rate enhancement of factor 2 when being brought close to the surface (gray). For ever larger distances, the decay rate will not be affected by the mirror and will reach the value for vacuum, independent of the dipole orientation.

1.4 Motivation and thesis outline

Having given a very brief introduction into first, the field of effective media and the realization of artificial metamaterials based on resonant plasmonic building blocks and second, the concept of the local density of optical states in the context of the fluorescence phenomenon, we want to state our motivation. The philosophy of the Ph.D. research project presented in this thesis was to obtain a better understanding of what a metamaterial, and what a metamaterial scatterer is, through LDOS. In particular, at the time this research was initiated, far-field normal-incidence transmission spectra measured on 2D arrays of split-ring scatterers were reported and interpreted as implying effective medium behavior with negative ε and μ [20, 21, 45, 46]. This behavior was attributed to individual building blocks, i.e., the split rings, and the notion that these are subwavelength polarizable dipoles with a coupled electric and magnetic response [19, 20, 47, 48, 49]. From these assertions the following questions emerge:

1. What should the LDOS for a dipole with an electric-dipole allowed transition actually be if one would have a hypothetical *magnetic* mirror or magnetic and electric metasurface (Fig. 1.3, a)?

2. Up to what point are effective ε and μ derived from far-field normal-incidence data actually good descriptors for a metamaterial, as one brings a probe from the far field into the near field to measure LDOS?

3. Can we strengthen or refute the claim that a single split ring is a magnetic dipole scatterer by probing if its radiation damping actually traces out magnetic LDOS (Fig. 1.3, b)?

4. How do single building-block magnetism on the one hand, and packing of objects in 2D periodic arrays on the other hand that must have collective Bloch modes conspire to give magnetic signatures in LDOS, and in far-field observables?

Since proposed metamaterial applications are mainly near-field applications, i.e., perfect lensing, cloaking, and transformation optics, experiments towards answering these four questions force one to come much closer to understanding metamaterials than far-field transmission and reflection experiments alone [50, 51, 52, 53, 54, 55].

In this thesis, we report on research intended to provide answers to the four key questions posed above. A first prerequisite to probe LDOS near surfaces is to establish a method to controllably separate LDOS probes and the surfaces that provide the LDOS change. An effective way of realizing a structure fulfilling the requirements of controlled distances on the

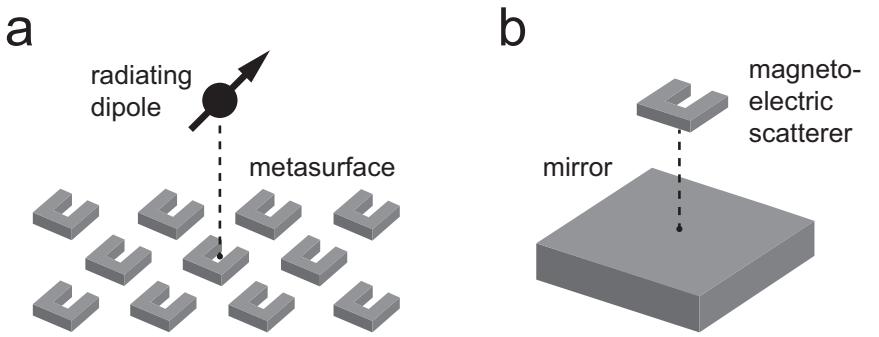

Figure 1.3: Questions raised and addressed within this thesis include: (a) What is the LDOS at the position of a radiating (transition) dipole above a metasurface? (b) How does the presence of a mirror affect the scattering properties of a magneto-electric scatterer such as a SRR?

nanometer scale over a large sample area on the micrometer scale is presented in Chapter 2. We show how, by applying gray-tone UV-lithography, a wedge-shaped dielectric can serve as a spacer layer between a silver mirror and a layer of fluorophores (dyes, quantum dots). Covering a range of distances up to about the respective fluorophores' emission wavelength, we effectively implement Drexhage's method to conduct quantitative decay rate measurements on emitter ensembles and can calibrate and compare intrinsic quantum efficiencies.

In Chapter 3, we discuss the concept of introducing a magneto-electric scatterer such as a split ring resonator (SRR) into a photonic environment with a well-known density of optical states such as a mirror. We predict that the scatterer's extinction cross-section linewidth depends on its distance to the mirror-surface due to a combination of electric, and magnetic local density of states effect, in accordance with earlier claims that split rings have both an electric and a magnetic dipole contribution to their scattering. Moreover, split rings have been predicted to have nonzero cross-coupling, meaning that electric fields can drive magnetic responses and vice versa. This effect is coined 'bi-anisotropy', and is strongly related to chiral responses of scatterers. Strikingly, the nonzero cross-coupling components in the scatterer's polarizability tensor will be reflected in the extinction cross-section lineshape. For a SRR, this lineshape differs from a lineshape expected from a purely electric or magnetic dipole. We show how this difference is stemming from the interplay of both dipole components as predicted by our analytical magneto-electric point-dipole model and support our finding by finite-element simulation.

Chapter 4 covers periodic two-dimensional arrangements of split ring resonators. We compare two types of lattices, indistinguishable by the individual split ring orientation within their respective unit cell. Transmission measurements conducted on (i) diffractive and (ii) nondiffractive realizations of both types of lattices reveal (i) the background-free signature of magnetic dipole response in Fourier imaging on illumination on resonance and (ii) a reduction of the apparent bi-anisotropy effect for off-normal illumination. A general model for metamaterial lattices with complex 2D unit cell of poly-atomic basis is introduced and explains experimentally observed phenomena. Furthermore, we extend this model to treat finite stacks of 2D lattices and calculate reflection and transmission spectra as a function of the number of layers. This model provides all the essential ingredients required to predict the LDOS change that metasurfaces will induce.

We combine our experience of sub-100 nm distance control and our comprehension of metasurfaces in Chapter 5 by studying combined systems of lattices formed by periodic arrangements of magneto-electric scatterers in front of a mirror. Combining the lattice-sum formalism with the interface Green-function approach we analytically calculate the renormalization of the per-particle polarizability and extract reflection coefficients. Calculated reflection and transmission coefficients for the individual interfaces serve as input parameters in a simple Fabry-Pérot model and apparent differences to the analytical approach are discussed that are interpreted in terms of back-action. A system comprised of SRR lattices separated from a silver mirror by a dielectric wedge spacer is fabricated and reflectivity data is acquired as a function of separation and frequency for different pitches. The experimentally acquired distance dependent reflectivity is compared to predictions of our lattice-sum magnetoelectric point-dipole model. Both find clear discrepancies to a simple Fabry-Pérot model which neglects the near-field influence on the single lattice atom's polarizability.

1.5 References

[1] J. D. Jackson, *Classical Electrodynamics*, Wiley, New York, 1999.

[2] L. Novotny and B. Hecht, *Principles of Nano-Optics*, Cambridge University Press, Cambridge, 2006.

[3] M. Born and E. Wolf, *Principles of Optics*, Cambridge University Press, Cambridge, 2002.

[4] C. Kittel, *Introduction to Solid State Physics*, Wiley, 2005.

[5] L. Landau, E. Lifshitz, and L. Pitaevskii, *Electrodynamics of Continuous Media, 2nd edition*, Elsevier, Amsterdam, 1984.

[6] R. Loudon, *The Quantum Theory of Light*, Oxford Science Publications, 1983.

[7] R. Boyd, *Nonlinear Optics*, Electronics & Electrical, Academic Press, London, 2003.

[8] P. Drude, *Zur Elektronentheorie der Metalle*, Annalen der Physik **306**, 566 (1900).

[9] N. Ashcroft and N. Mermin, *Solid State Physics*, Saunders College Publishing, 1976.

[10] D. Bruggeman, *Berechnung verschiedener physikalischer Konstanten von heterogenen Substanzen*, Ann. Phys. **24**, 636 (1935).

[11] J. Garnett, *Colours in metal glasses and in metallic films*, Phil. Trans. R. Soc. Lond. **203**, 385 (1904).

[12] V. G. Veselago, *The electrodynamics of substances with simultaneously negative values of epsilon and mu*, Physics-Uspekhi **10**, 509 (1968).

[13] J. B. Pendry, *Negative refraction makes a perfect lens*, Phys. Rev. Lett. **85**, 3966 (2000).

[14] D. R. Smith, W. J. Padilla, D. C. Vier, S. C. Nemat-Nasser, and S. Schultz, *Composite medium with simultaneously negative permeability and permittivity*, Phys. Rev. Lett. **84**, 4184 (2000).

[15] C. M. Soukoulis, S. Linden, and M. Wegener, *Negative refractive index at optical wavelengths*, Science **315**, 47 (2007).

[16] G. Dolling, C. Enkrich, M. Wegener, C. M. Soukoulis, and S. Linden, *Simultaneous negative phase and group velocity of light in a metamaterial*, Science **312**, 892 (2006).

[17] V. M. Shalaev, *Optical negative-index metamaterials*, Nat. Photon. **1**, 41 (2007).

[18] C. Enkrich, M. Wegener, S. Linden, S. Burger, L. Zschiedrich, F. Schmidt, J. F. Zhou, T. Koschny, and C. M. Soukoulis, *Magnetic metamaterials at telecommunication and visible frequencies*, Phys. Rev. Lett. **95**, 203901 (2005).

[19] C. Rockstuhl, T. Zentgraf, H. Guo, N. Liu, C. Etrich, I. Loa, K. Syassen, J. Kuhl, F. Lederer, and H. Giessen, *Resonances of split-ring resonator metamaterials in the near infrared*, Appl. Phys. B **84**, 219 (2006).

[20] M. W. Klein, C. Enkrich, M. Wegener, C. M. Soukoulis, and S. Linden, *Single-slit split-ring resonators at optical frequencies: limits of size scaling*, Opt. Lett. **31**, 1259 (2006).

[21] C. Rockstuhl, C. Menzel, T. Paul, T. Pertsch, and F. Lederer, *Light propagation in a fishnet metamaterial*, Phys. Rev. B **78**, 155102 (2008).

[22] J. R. Lakowicz, *Principles of Fluorescence Spectroscopy*, Springer, 2006.

[23] R. Sprik, B. A. van Tiggelen, and A. Lagendijk, *Optical emission in periodic dielectrics*, Eur. Phys. Lett. **35**, 265 (1996).

[24] V. Bykov, *Spontaneous emission in a periodic structure*, Sov. Phys. JETP **35** (1972).

[25] E. Yablonovitch, *Inhibited spontaneous emission in solid-state physics and electronics*, Phys. Rev. Lett. **58**, 2059 (1987).

[26] S. John, *Strong localization of photons in certain disordered dielectric superlattices*, Phys. Rev. Lett. **58**, 2486 (1987).

[27] S. Dutra, *Cavity Quantum Electrodynamics: The Strange Theory Of Light In A Box*, Wiley Series in Lasers and Applications, J. Wiley, 2005.

[28] S. Haroche and J. Raimond, *Exploring the Quantum: Atoms, Cavities, And Photons*, Oxford graduate texts in mathematics, Oxford University Press, 2006.

[29] F. D. Martini, G. Innocenti, G. R. Jacobovitz, and P. Mataloni, *Anomalous spontaneous emission time in a microscopic optical cavity*, Phys. Rev. Lett. **59**, 2955 (1987).

[30] R. J. Thompson, G. Rempe, and H. J. Kimble, *Observation of normal-mode splitting for an atom in an optical cavity*, Phys. Rev. Lett. **68**, 1132 (1992).

[31] E. Snoeks, A. Lagendijk, and A. Polman, *Measuring and modifying the spontaneous emission rate of erbium near an interface*, Phys. Rev. Lett. **74**, 2459 (1995).

[32] R. M. Amos and W. L. Barnes, *Modification of the spontaneous emission rate of* Eu^{3+} *ions close to a thin metal mirror*, Phys. Rev. B **55**, 7249 (1997).

[33] M. J. A. de Dood, L. H. Slooff, A. Polman, A. Moroz, and A. van Blaaderen, *Modified spontaneous emission in erbium-doped* SiO_2 *spherical colloids*, Appl. Phys. Lett. **79**, 3585 (2001).

[34] M. D. Leistikow, J. Johansen, A. J. Kettelarij, P. Lodahl, and W. L. Vos, *Size-dependent oscillator strength and quantum efficiency of cdse quantum dots controlled via the local density of states*, Phys. Rev. B **79**, 045301 (2009).

[35] M. Frimmer, A. Mohtashami, and A. Femius Koenderink, *Nanomechanical method to gauge emission quantum yield applied to nitrogen-vacancy centers in nanodiamond*, Applied Physics Letters **102**, (2013).

[36] A. Mohtashami and A. F. Koenderink, *Suitability of nanodiamond nitrogen vacancy centers for spontaneous emission control experiments*, New Journal of Physics **15**, 043017 (2013).

[37] S. Karaveli and R. Zia, *Spectral tuning by selective enhancement of electric and magnetic dipole emission*, Phys. Rev. Lett. **106**, 193004 (2011).

[38] M. Frimmer, Y. Chen, and A. F. Koenderink, *Scanning emitter lifetime imaging microscopy for spontaneous emission control*, Phys. Rev. Lett. **107**, 123602 (2011).

[39] A. W. Schell, P. Engel, J. F. M. Werra, C. Wolff, K. Busch, and O. Benson, *Scanning single quantum emitter fluorescence lifetime imaging: Quantitative analysis of the local density of photonic states*, Nano Letters **14**, 2623 (2014).

[40] Q. Wang, S. Stobbe, and P. Lodahl, *Mapping the local density of optical states of a photonic crystal with single quantum dots*, Phys. Rev. Lett. **107**, 167404 (2011).

[41] R. Sapienza, T. Coenen, J. Renger, M. Kuttge, N. F. van Hulst, and A. Polman, *Deep-subwavelength imaging of the modal dispersion of light*, Nat. Materials **11**, 781 (2012).

[42] P. Lodahl, S. Mahmoodian, and S. Stobbe, *Interfacing single photons and single quantum dots with photonic nanostructures*, arXiv:1312.1079 (2013).

[43] K. H. Drexhage, H. Kuhn, and F. P. Schäfer, *Variation of the fluorescence decay time of a molecule in front of a mirror*, Ber. Buns. f. Phys. Chem. **72**, 329 (1968).

[44] B. C. Buchler, T. Kalkbrenner, C. Hettich, and V. Sandoghdar, *Measuring the quantum efficiency of the optical emission of single radiating dipoles using a scanning mirror*, Phys. Rev. Lett. **95**, 063003 (2005).

[45] J. Valentine, S. Zhang, T. Zentgraf, E. Ulin-Avila, D. A. Genov, G. Bartal, and X. Zhang, *Three-dimensional optical metamaterial with a negative refractive index*, Nature **455**, 376 (2008).

[46] J. Yang, C. Sauvan, H. T. Liu, and P. Lalanne, *Theory of fishnet negative-index optical metamaterials*, Phys. Rev. Lett. **107**, 043903 (2011).

[47] C. Rockstuhl, T. Zentgraf, E. Pshenay-Severin, J. Petschulat, A. Chipouline, J. Kuhl, T. Pertsch, H. Giessen, and F. Lederer, *The origin of magnetic polarizability in metamaterials at optical frequencies - an electrodynamic approach*, Opt. Express **15**, 8871 (2007).

[48] M. Husnik, M. W. Klein, N. Feth, M. Koenig, J. Niegemann, K. Busch, S. Linden, and M. Wegener, *Absolute extinction cross-section of individual magnetic split-ring resonators*, Nat. Photon. **2**, 614 (2008).

[49] N. Feth, M. König, M. Husnik, K. Stannigel, J. Niegemann, K. Busch, M. Wegener, and S. Linden, *Electromagnetic interaction of split-ring resonators : The role of separation and relative orientation*, Opt. Expr. **18**, 215 (2010).

[50] J. B. Pendry, D. Schurig, and D. R. Smith, *Controlling electromagnetic fields*, Science **312**, 1780 (2006).

[51] A. Alù and N. Engheta, *Plasmonic and metamaterial cloaking: physical mechanisms and potentials*, J. Opt. A **10**, 093002 (2008).

[52] N. Liu, H. Guo, L. Fu, S. Kaiser, H. Schweizer, and H. Giessen, *Three-dimensional photonic metamaterials at optical frequencies*, Nat Mater **7**, 31 (2008).

[53] J. Valentine, J. Li, T. Zentgraf, G. Bartal, and X. Zhang, *An optical cloak made of dielectrics*, Nat. Mater. **8**, 568 (2009).

[54] C. M. Soukoulis and M. Wegener, *Past achievements and future challenges in the development of three-dimensional photonic metamaterials*, Nat. Photon. **5**, 523 (2011).

[55] C. Pfeiffer and A. Grbic, *Metamaterial huygens surfaces: Tailoring wave fronts with reflectionless sheets*, Phys. Rev. Lett. **110**, 197401 (2013).

Chapter 2

Calibrating radiative and nonradiative decay constants of fluorophores

We present a method that is accurate yet fast to implement to realize non-planar dielectric structures with a controlled height profile for use in calibration of fluorophores. Calibration of fluorescence quantum efficiency and intrinsic radiative and nonradiative decay rates of emitters is possible by using changes in the local density of optical states, provided one can control the emitter-surface distance with nanometer accuracy. We fabricate PMMA wedges (4 mm×4 mm×2 µm) by gray-tone UV-lithography of Shipley S1813G2. Its applicability as dielectric spacer is demonstrated in Drexhage experiments for three different emitters in the visible and near-infrared wavelength regime. The decay-rate dependence of the fluorescent state of emitters on the distance to a silver mirror is observed and compared to calculations of the local density of states. Quantitative values for (non)radiative decay rates and quantum efficiencies are extracted. Furthermore, we discuss how Drexhage experiments can help to scrutinize the validity of effective material parameters of metamaterials in the near-field regime.

2.1 Introduction

A key contribution of photonic technology to society is the realization of light sources with desirable properties, such as controlled spectrum, brightness, improved wall-plug efficiency, or coherence properties. The creation of such novel light sources, i.e., LED's and lasers, heavily depends on two types of innovation. These are firstly the realization of cheap materials that have optical transitions of high efficiency and desired frequency, and secondly the integration of these source materials with photonic structures that further improve the performance. Among the material developments, innovations in the last decade range from organic dyes and light-emitting polymers in organic LEDs [1], to the use of epitaxially grown III-V semiconductor quantum dots [2] and quantum wells [3] in common laser diodes and LED's, to colloidally fabricated II-VI quantum dots [4] that are size tunable throughout the entire visible spectrum. To improve the performance of the bare sources, or homogeneous thin layers of the luminescent materials, many groups pursue nanophotonic techniques to improve light extraction, as well as to increase the spontaneous emission rate in favor of undesired nonradiative decay constants. Both photonic crystals [5] as well as patterning with arrays of plasmonic antennas [6, 7, 8, 9] have been shown to succesfully contribute to light extraction, and optimization of the radiative time constants [10]. The key quantity that quantifies the possible improvement of the radiative decay is the local density of optical states (LDOS) enhancement that a nanophotonic structure provides [11, 12]. The LDOS counts the total number of optical modes, weighted by their amplitude right at the emitter, that are available to the source for radiative transitions, and hence directly appears in Fermi's Golden Rule for spontaneous emission [12]. Optimization of LDOS is not only important for macroscopic classical light sources, such as LEDs, but is also key for quantum optical applications where a single quantum emitter is to be strongly coupled to a single optical mode [13, 14].

A method to reliably measure the intrinsic time constants of arbitrary emitters is of large importance both for quantifying improvements in emissive materials, and for quantifying the LDOS enhancing potential of a nanophotonic structure. For an emissive material, the challenge is to determine rapidly and accurately the intrinsic radiative rate, nonradiative rate and quantum efficiency of emitters as a tool to guide material improvement and to understand the mechanisms behind, e.g., unwanted nonradiative decay. Conversely, if one wishes to benchmark the local density of states improvement that a structure can intrinsically provide, it is important to probe the structure with a source that has first been quantified in terms of its radiative and nonradiative rate constants. Unfortunately, commonly used

fluorescence decay measurements only provide the *sum* of rates [15], while quantum efficiency measurements are usually based on brightness comparisons. Such comparisons are prone to imprecision if one has to rely on comparison to a fluorescence quantum efficiency standard, and yield erroneous results when a sample consists of a heterogeneous ensemble in which fluorophores exhibit large brightness variations. On basis of an experiment first performed by Drexhage [16, 17], many authors have realized that intrinsic rate constants can be reliably measured by applying a known, controlled LDOS variation to an emitter [18, 19, 20]. Drexhage studied the radiative decay rate of europium ions as a function of distance to a silver mirror. The observed variation in decay rate, stemming from interference of emitted and reflected light, can be explained by a change in the LDOS at the emitter position [21]. Since the LDOS is exactly known, the data can be quantitatively separated into an intrinsic nonradiative rate that does not vary with LDOS, and a radiative rate that does. This technique has been used for organic dyes, rare-earth ions [19, 22], and more recently for II-VI quantum dots [23], III-V quantum dots [24, 25], and even single emitters when using a nanomechanically scanned mirror [20]. Unfortunately, the techniques to controllably vary distance are generally elaborate, and material specific. For instance, Leistikow et al. [23] required fabrication of a large set of samples with evaporated layers of calibrated heights. In the case of Stobbe et al. [24], a single substrate could be used, but an elaborate reactive ion etching step specific for III-V chemistry, and using a complicated masking procedure was required to fabricate discrete steps. In this work, we report an easily implemented method to realize Drexhage experiments on top of arbitrary planar structures.

In this chapter, we propose that gray-tone optical lithography [26] allows to attach very shallow wedges on top of arbitrary substrates. Drexhage experiments can then be performed either by depositing the wedge on the emitter and evaporating a mirror on it, or conversely by placing the wedge on a mirror, and distributing sources on the wedge (Fig. 2.1). The key requirement for the optical wavelength regime is that the wedge has a shallow angle so that the mirror is almost parallel to the emissive substrate, yet also to have nanometer control over the wedge height and roughness that sets the spatial separation of the emitter and the substrate. We fabricated wedge-shaped dielectric spacers by gray-tone lithography and performed Drexhage experiments to calibrate three different emitters: fluorescent polystyrene beads emitting at 605 nm, CdSeTe/ZnS (core/shell) quantum dots emitting at 800 nm, and Dibenzoterrylene molecules in anthracene crystals emitting at 750 nm. While these emitters were chosen for their promising use in nanoscale quantum optics with plasmon antennas [27, 28, 29, 30] and metamaterials [31, 32, 33], the method is easily applied to any emitter that can

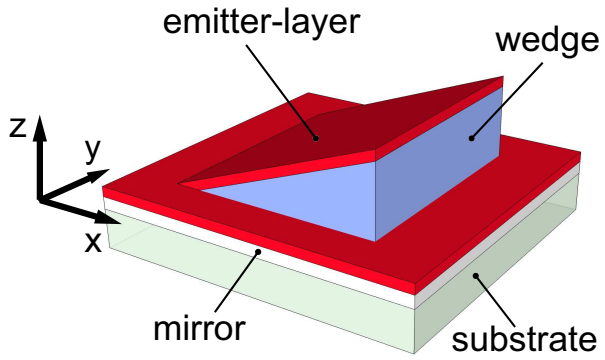

Figure 2.1: A wedge shaped dielectric separates a layer of emitters from a mirror. This geometry allows to conduct a Drexhage experiment — observing the fluorescent decay rate of emitters as a function of distance to a mirror — on a single sample.

be reasonably homogeneously distributed in a planar layer. The wedges can also be used with calibrated emitters, to measure LDOS near unknown substrates, such as gratings and plasmon antenna arrays. The chapter is structured as follows. In section 2.2 we discuss gray-tone UV-lithography, wedge-profile characterization and emitter layer spin-coating steps. Section 2.5 covers the optical measurement procedure. Lifetime measurements and derived intrinsic rate constants for the three emitters are presented in section 2.6. Finally, along with our conclusion we provide an outlook.

2.2 Gray-tone lithography

In this chapter, we discuss four samples: three samples featuring emitters with specific emission wavelengths and fluorescent lifetime characteristics and one benchmark sample to check the height profile using a variety of techniques. All samples feature an optically thick ($\approx 100\,\mathrm{nm}$) layer of silver that is evaporated on silicon wafer pieces (each $\approx 20\,\mathrm{mm}\times 20\,\mathrm{mm}$). The silver layer, which we characterized by ellipsometry, serves as mirror for the Drexhage experiments. The essential step is the fabrication of a dielectric spacer with controlled and graded height profile using optical lithography. Since optical lithography resists tend to fluoresce themselves, we create two types of samples, namely samples with and without an intermediate, considerably less fluorescent, PMMA layer. For samples of the first type a $2\,\mu\mathrm{m}$ thick layer of PMMA ($M = 950\,000\,\mathrm{g/mol}$, 8 % in Anisole) is spincoated ($45\,\mathrm{s}$ at $1000\,\mathrm{rpm}$, baking for $2\,\mathrm{min}$ at $180^\circ\mathrm{C}$). For all samples (with and

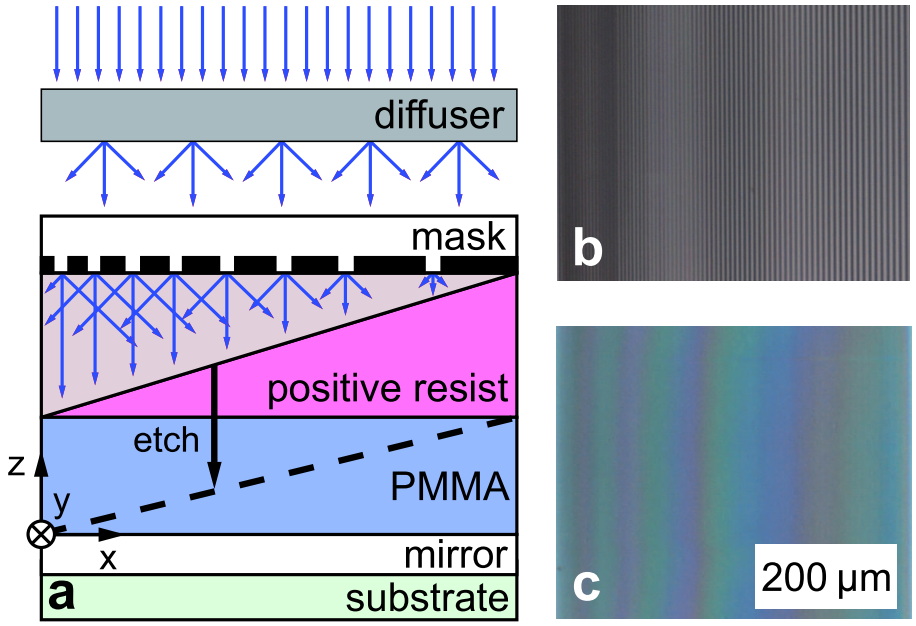

Figure 2.2: Diffuse UV-illumination of a 'gray-tone' chromium mask generates a wedge shaped zone with doses above the critical dose of the positive resist. After development, the wedge can be transferred into a different material, such as PMMA, via reactive oxygen ion etching (a). Differential interference contrast microscopy images of developed Shipley S1813G2 resist without diffusive element during UV-exposure, resembling the chromium mask pattern (b), and with diffusive element, showing a 'smoothed out' continuously sloping surface (c). The interference color change along x implies varying distances to the silver mirror.

without PMMA) we then spincoat a 2 µm thick layer of Shipley Microposit S1813 G2 positive UV-resist (45 s at 1000 rpm, baking for 2 min at 115°C). To define the wedge shape in the resist, we perform UV-lithography using a Süss MJB3 mask aligner with a binary chromium mask that consists of parallel lines, at varying surface coverage similar to Christophersen et al. [26]. The mask for each dielectric wedge is a 4 mm×4 mm area, made up of 4 mm long chromium lines in the y-direction with increasing width in the x-direction from 1.5 µm (low end of the wedge) up to 12 µm (high end of the wedge). All lines are spaced in the x-direction by gaps of 3 µm. Thereby, the average density continuously varies from 33 % surface coverage to 80 % surface coverage. To generate a graded illumination, we use an opal glass diffuser (Edmund Optics, NT02-149) placed in a filter holder ≈ 1 cm above the sample and mask. The resist is exposed with a dose of 300 mJ/cm^2

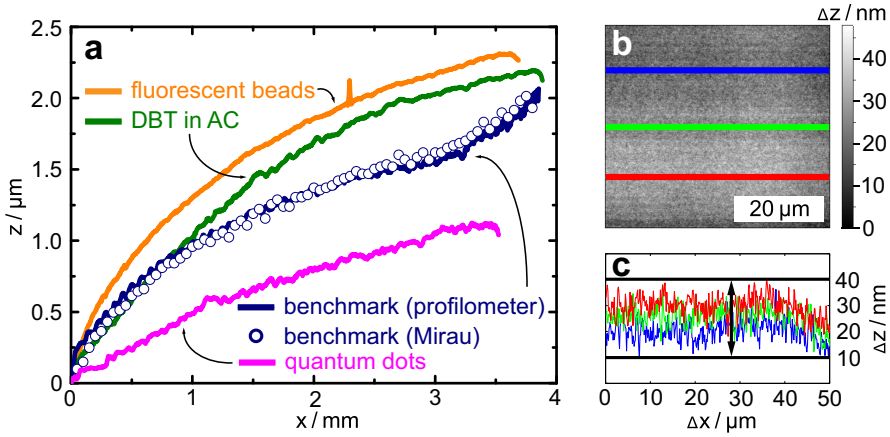

Figure 2.3: Panel (a): height profiles of 4 different wedges, used for fluorescent beads, quantum dots, DBT, and a topographic benchmark sample. For the benchmark we also performed Mirau-interferometry (round symbols) and find good agreement with profilometry. The fluorescent bead and DBT in AC samples feature an additional PMMA layer underneath the S1813 UV-resist. The wedge for the quantum dot sample consists solely of S1813 (a). Panel (b): an atomic force microscopy scan is conducted to retrieve a roughness estimate of the typical wedge surface. Line traces in (c) show a sub-30 nm roughness as indicated by the double-arrow.

and developed in Microposit MF-319 for 15 s (Fig. 2.2). At this point, we have a wedge profile in S1813 on top of Ag or a Ag/PMMA stack. For the samples with PMMA, the wedge profile, defined in S1813, is transferred into the PMMA layer by reactive oxygen ion etching (Oxford Instruments Plasmalab 80+, 20 sccm O_2 gas flow, 50 W forward power, 292 K operating temperature). After approx. 35 min of etching the S1813 is completely removed from the lower end of the wedge. The etch rate of PMMA is twice the etch rate of S1813, therefore the slope of the original profile is changed and the upper end of the PMMA wedge will be covered with residual S1813.

2.3 Wedge profile characterization

We characterize the wedge profiles by profilometry (KLA-Tencor Alpha-Step 500) and compare the profilometry data set of a benchmark sample to Mirau-interferometry data (Nikon 20x CF IC Epi Plan DI) (Fig. 2.3, a). Mirau interferometry is a purely optical method in which one places the sample in a standard white light reflection microscope. However, rather than

using a standard objective one uses a so-called Mirau objective that fits in a standard objective thread, yet contains in a addition to a standard glass lens a reference mirror. In more detail, halfway between lens and sample, a 50/50 beam splitter reflects part of the incident halogen light on to the reference mirror. The reflection off the mirror recombines with the reflection off the sample at the same 50/50 beam splitter. Imaging the sample on a CCD camera hence shows a fringe pattern that encodes height differences in the sample versus lateral coordinate. While for monochromatic illumination one can only measure heights modulo half integer wavelengths as zero crossings in the fringe pattern, for white light illumination one can actually measure absolute heights in relation to the reference mirror conjugate plane. Indeed, for white light illumination, the fringes are strongly chromatic, except when the sample plane is exactly conjugate to the reference mirror, in which case a black fringe results. In our work we trace the height of the wedge relative to the substrate by monitoring when the black fringe appears on the bare substrate, respectively on the wedge as we scan the sample upwards using a calibrated piezo.

As regards profilometry, in this technique height is determined by scanning a sharp stylus laterally over a horizontal surface while applying a constant vertical load and monitoring vertical stylus displacement. We note that the KLA-Tencor Alpha-Step 500 is not designed to scan such large lateral areas (for the wedges in question: $4\,\mathrm{mm}\times 4\,\mathrm{mm}$). Hence raw profilometry data showed apparent sample curvature as well as apparent roughness that in fact turned out not to be intrinsic to the sample, but to be systematic and reproducible artefacts that are due to the stylus scanner mechanics. However, once one uses a flat optical substrate, such as an optical grade silver mirror (Thorlabs PF10-03-P01), as reference in the profilometer, a good agreement between profilometry and interferometry is obtained (Fig. 2.3, a, dots and curve). This supports the sole use of the profilometer as a tool to acquire (x,z)-profiles of all the other samples. Typically, the base of a wedge, in contact to the silver mirror, is 4 mm wide in the x- and y- (scan-) directions, as inherited from the mask. The (x,z)-profiles resemble a 'fin'-shape starting off with a steeper slope at the low end and ending with a shallower height increment per sideways displacement at the upper end of the wedges. The overall slope remains well below $1.5\,\mu\mathrm{m/mm}$, meaning that the wedge angle is so shallow that effectively constant-height data can be obtained in micro-fluorescence experiments. Since neither profilometry nor Mirau-interferometry can resolve roughness reliably on lateral length scales below $1\,\mu\mathrm{m}$, we also performed atomic force microscopy measurements. We extract a typical surface roughness of $\Delta z/\Delta x < 30\,\mathrm{nm}/50\,\mu\mathrm{m}$ (Fig. 2.3 b, c). Compared to established methods for Drexhage experiments, which are usually based on controlled stepwise RIE etching, or on controlled evapora-

tion of different thicknesses, our method has the advantage that all desired source-mirror distances are created on a single substrate with a single simple optical lithography step. The roughness and shallow slope of the wedge imply that Drexhage experiments can be performed for wavelengths down to $\approx 500\,\mathrm{nm}$ ($< \lambda/10$ roughness). Finally, we note that Fig. 2.3(a) shows that while all samples have a smooth wedge, not all wedges have the same overall height profile. In general etching from S1813 into PMMA steepens the height profile due to a factor two difference in etch rate. In our work differences in height profile also occur due to minor variations in the spin-coated thickness and in the UV exposure dose, as a result of adjustments in the mask aligner illumination alignment between runs. In this work we use individual z-profile calibrations for each wedge, though improvements in processing could render this procedure unnecessary.

2.4 Preparation of fluorophores

A succesful Drexhage experiment not only requires smooth dielectric spacers of controlled height, as characterized above, but also that the emitters can be homogeneously dispersed on the wedge. We present measurements on three types of fluorophores. Firstly, we use fluorescent polystyrene beads (Invitrogen Fluospheres F8801), with a nominal bead diameter of $0.1\,\mu\mathrm{m}$ containing about 10^3 randomly oriented dye-molecules each, that are completely chemically shielded from the bead's environment. We estimate this number of dye molecules on the basis of intensity measurements taken in a single molecule sensitive microscope of known collection efficiency as reported by Frimmer et al. [34]. Their fluorescence intensity peaks at 605 nm. Since S1813 wedges in themselves fluoresce in the same wavelength range, with comparable time constants, we use a nonfluorescent PMMA wedge. To counteract agglomeration of beads we sonicate the stock solution (2 % solids) for 2 minutes prior to mixing $1\,\mu\mathrm{l}$ of the bead solution with 1 ml of deionized water. This mixture is spin-coated for 10 s at 500 rpm (100 rpm/s acceleration) followed by a second spin step of 45 s at 1500 rpm (500 rpm/s). From a typical confocal fluorescence microscopy image (Fig. 2.5, left) we deduce a bead concentration of $\approx 0.15\,\mu\mathrm{m}^{-2}$.

As a second emitter, we study CdSeTe/ZnS (core/shell) quantum dots (Invitrogen Qdot 800 ITK carboxyl) as they were recently proposed as light sources for plasmonic applications [29, 27]. In comparison to more common CdSe/ZnS quantum dot nanocrystals for visible emission, these quantum dots feature longer lifetimes [35]. The quantum dots are diluted in a borate buffer solution ($\mathrm{pH} = 8.0$) to a molar concentration of $8\,\mu\mathrm{M}$. We mix $4\,\mu\mathrm{l}$ of this solution with 1 ml of deionized water and spincoat a droplet of the mix-

ture on top of the S1813 wedge-sample for 45 s at 4000 rpm (4000 rpm/s). Here, the use of an S1813 wedge is justified, since the fluorescence of the quantum dots and of the polymer can be separated easily via spectral selection, and a factor 10 contrast in fluorescence decay constants.

As third type of emitter, we investigate Dibenzoterrylene (DBT) molecules in Anthracene (AC) crystals [36, 37]. DBT molecules have been found to feature great photostability and brightness at room temperature (10^{12} emitted near-infrared photons before photobleaching) while also fluorescing in the near-infrared around 750 nm [37]. We dissolve 0.6 mg of DBT powder (Dr. W. Schmidt, PAH Research Institute, Greifenberg, Germany) in 1 ml of Toluene. In accordance with the recipe by Toninelli [37], we use 5.3 mg of AC dissolved in 2 ml of Diethylether and 20 µl of Benzene. Finally, 80 µl of DBT-solution is mixed with 0.5 ml of AC-solution. The resulting solution is spin-coated for 40 s at 3500 rpm (500 rpm/s acceleration).

2.5 Experiment

Fig. 2.4 depicts the basic components of the confocal fluorescence lifetime scanning microscope, in which we perform the Drexhage experiments. Light from the excitation laser is focused to the diffraction limit, and emitted light from fluorescent objects in the focus is collected via the same objective (Nikon 100×, NA = 0.90, Plan Fluor) in a confocal arrangement. The fluorescent light is separated from the excitation at a dichroic beamsplitter and passes additional long-/bandpass filters chosen according to the absorption and emission spectrum of the emitter of interest. The fluorescent beads as well as the quantum dots are pumped by a pulsed laser (Time-Bandwidth Products) operating at 532 nm emission wavelength (green), 10 MHz repetition rate with pulse widths < 10 ps. Dibenzoterrylene molecules have a 25 times higher absorption cross section in the red compared to the green part of the spectrum. Therefore, we choose a different pump source for this emitter: a pulsed laser diode (Edinburgh Instruments EPL) at 635 nm, operated at 10 MHz repetition rate featuring pulse widths of < 100 ps.

Achromatic optics focuses the fluorescent light onto a silicon avalanche photodiode (APD) (ID Quantique id100-20ULN) with an active area diameter of 20 µm, using an effective magnification from objective to APD of 20×. The APD-pulses and the reference pulses from a trigger diode (green laser) or electrical trigger output (red laser) are registered by a picosecond, 16 channel, pulse correlator (Becker&Hickl DPC-230), which records absolute timestamps at 165 ps resolution for each event. The sample is mounted on a (x,y)-piezo stage. By scanning the sample with respect to the objective we acquire fluorescence intensity maps of 100 × 100 pixels ($\approx 10\,\mu m \times 10\,\mu m$)

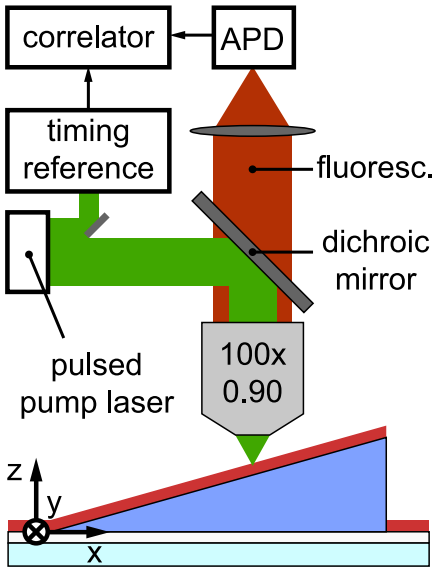

Figure 2.4: Sketch of the time correlated single photon counting setup. Light from a pulsed pump laser is focused onto the emitter layer. A dichroic mirror is used to separate the fluorescent light stemming from the emitters and the pump light. Depending on the emission wavelength of the emitters, appropriate long-/bandpass filters are added to the beam path. In that way only light stemming from fluorescent objects of interest is focused onto the APD. The photon arrival times with respect to the pump pulse together with the (x,y)-piezo stage position generate a fluorescent lifetime image of the sample at a certain emitter-mirror separation z.

with a pixel scan rate of 100 Hz. For each scan we sum the single photon events of a chosen region of interest in a time-histogram. These areas are so small that no appreciable height gradient occurs in the wedge. The images hence serve to assess local homogeneity in fluorophore intensity only. For each scan we correlate the single photon detection events and laser pulses to form a fluorescence decay histogram, which we sum either over the full image or over a chosen region of interest (e.g., to select isolated beads) in the 2D scan. Different positions along the height gradient of the wedge are reached by a manually operated micromechanical stage.

2.6 Results

Fig. 2.5, left shows a typical scan of beads on top of the wedge aquired by fluorescence-lifetime imaging microscopy (FLIM). The intensity map shows

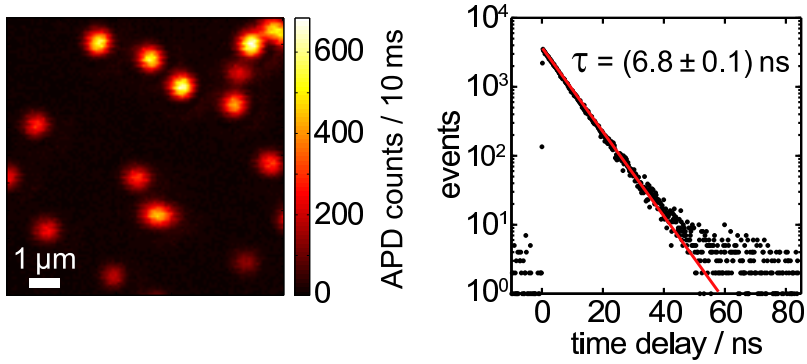

Figure 2.5: Typical fluorescence intensity image of beads on top of the PMMA wedge (left) and corresponding fluorescence decay histogram (accumulated events from diffraction limited bright spots in intensity image) (right). We clearly see a single exponential decay for which intensity and lifetime τ are fitted in the maximum likelihood sense assuming Poissonian counting statistics for each time bin.

isolated diffraction limited bright spots on a very dark background, which is consistent with having a dilute sprinkling of isolated beads. Although the slight top-bottom intensity gradient in this particular image suggests a small focus drift during the measurement, our method is robust against such drift. Raster scanning excludes photophysical changes in the sample, such as bleaching as artifact. Since our quantum efficiency calibration does not rely on extracting brightness, but on extracting lifetimes, we are not prone to, e.g., the small setup drifts that can cause brightness artifacts. Selecting only those events that appear in the diffraction limited bright spots we obtain a histogram of photon counts versus arrival time after the pump pulse, i.e., a fluorescence decay curve, for all beads within the scanned image. One such histogram is shown in Fig. 2.5, right, taken from the fluorescence image Fig. 2.5, left, recorded around position $x = 340\,\mu\text{m}$ along the wedge length (i.e., $z \approx 700\,\text{nm}$). For each position along the wedge profile, i.e., for each sample-source distance where we acquired a FLIM image, we fit the observed fluorescence decay histogram with a single exponential decay. In our fit we assumed the background to be fixed (set to the mean events per bin in the time bins with time delay $< 0\,\text{s}$, before pump pulse arrival) and fit only a decay rate and an initial amplitude. We find the most probable set of these two parameters by using the maximum-likelihood method under the assumption of Poissonian counting statistics for each time bin [38]. In Fig. 2.6, left, we plot the experimentally retrieved fluorescent decay rate as a function of bead-mirror distance z. We find an increase of the decay rate

up to $0.27\,\mathrm{ns}^{-1}$ for $z \approx 90\,\mathrm{nm}$. We did not resolve decay rates for values closer to the mirror which, predicted by LDOS theory, would first decrease to a minimum at around $z = 25\,\mathrm{nm}$ before rising again for $z \to 0$. For $z > 100\,\mathrm{nm}$, the decay rate dependency resembles a damped oscillation around $0.18\,\mathrm{ns}^{-1}$ with a periodicity of $\approx \lambda_{\mathrm{bead}}^{\mathrm{em}}/(2n_{\mathrm{PMMA}}) \approx 200\,\mathrm{nm}$ as expected when considering the interference condition for emitted and reflected field amplitudes.

In order to extract a quantitative calibration of the intrinsic decay constants of the emitters, i.e., their intrinsic nonradiative decay rate and their radiative decay rate when held in vacuum, we fit the experimentally acquired total decay rate $\gamma_{\mathrm{tot}}(z)$, dependent on the emitter-mirror separation z, to

$$\gamma_{\mathrm{tot}}(z) = \gamma_{\mathrm{rad}} \cdot \rho(z) + \gamma_{\mathrm{nonrad}} \tag{2.1}$$

where $\rho(z)$ equals the relative local density of states $\rho = \mathrm{LDOS}/\mathrm{LDOS}_{\mathrm{vac}}$ for a dipole above a silver mirror. Note that the intrinsic nonradiative decay γ_{nonrad} acts as an offset that is not affected by the mirror. Any quenching *induced by the mirror* is contained in the term proportional to the intrinsic radiative decay rate, i.e., in ρ. We use established theory [21, 18, 39, 12] to calculate ρ on basis of the refractive indices for S1813, PMMA and the silver mirror that were acquired from ellipsometry measurements.

Since in our experiment, we acquire fluorescence intensity from an ensemble of $\approx 10^3$ dye molecules within each bead, we assume an isotropic distribution of dipole orientations. Therefore we use the orientation averaged

$$\rho_{\mathrm{iso}}(z) = \frac{1}{3}\rho_{\perp}(z) + \frac{2}{3}\rho_{\parallel}(z) \tag{2.2}$$

where $\rho_{\perp}(z)$ and $\rho_{\parallel}(z)$ are the relative local density of states for dipoles oriented perpendicular and parallel to the mirror surface, respectively [40].

The fitted $\gamma_{\mathrm{tot}}^{\mathrm{iso}}(z)$ (calculated for dipoles embedded 10 nm below the PMMA/air interface to account for the bead material) is plotted as the red line in Fig. 2.6, left. We find fair agreement with the experimental data. For distances exceeding the vacuum emission wavelength of the emitter (due to the wedge index this encompasses several oscillations in the LDOS) the oscillation amplitude of the local density of states decreases and becomes comparable to the uncertainty in fitted total decay rates. We hence use the emitter's emission wavelength as upper bound on distances plotted. By plotting decay rate versus LDOS, instead of decay rate versus z, we can directly find the radiative and nonradiative decay rate from the slope and ordinate intersection of the linear dependence, respectively (Fig. 2.7). Throughout this work, error bars on rates and efficiencies result from the LDOS fit, taking into account error bars on the decay rate fitted at each

vertical distance. For the fluorescent beads, we find an intrinsic radiative decay rate of $(0.10 \pm 0.01)\,\mathrm{ns}^{-1}$ and a nonradiative decay rate of $(0.07 \pm 0.01)\,\mathrm{ns}^{-1}$. The hypothetical radiative decay rate for this emitter in vacuum, extrapolates to a radiative rate of $(0.15 \pm 0.01)\,\mathrm{ns}^{-1}$ in its PMMA host. We extract a quantum efficiency

$$q.e. \equiv \gamma_{\mathrm{rad}}/(\gamma_{\mathrm{rad}} + \gamma_{\mathrm{nonrad}}) \tag{2.3}$$

of $61\% \pm 7\%$ for the emitter hypothetically in vacuum, and around $70\% \pm 6\%$ for the emitter embedded in its bulk host material, i.e., bulk PMMA.

In many applications targeting the use of metamaterials and plasmonics to control emitters, one preferentially does not use emitters with emission wavelengths at 605 nm, such as the beads, but rather emitters emitting further into the near-infrared. Recent reports by Curto et al. [29] propose that CdSeTe/ZnS quantum dots emitting at around 800 nm are ideally suited single emitters for plasmonic applications, as they are ultrabright. The fluorescence time delay histogram retrieved from a FLIM image of an ensemble of Invitrogen Qdot 800 ITK carboxyl quantum dots does not resemble a single exponential decay. In order to fit these traces, we make use of the fact that an ensemble of quantum dots should be modeled with a continuous distribution of decay rates [41, 42]. More precisely, the natural logarithm of decay rates γ is assumed to be normally distributed—as verified by Lunnemann et al. [43]—according to the log-normal distribution

$$p(\gamma) = A \cdot \exp\left(-\frac{\ln^2(\gamma/\gamma^{\mathrm{mf}})}{w^2}\right). \tag{2.4}$$

The normalization constant A is given by the condition $\int_0^\infty p(\gamma)d\gamma = 1$. The dimensionless width w can be rewritten as the width of the rate distribution for which $p = 1/e$:

$$\Delta\gamma = 2\gamma^{\mathrm{mf}} \sinh w. \tag{2.5}$$

Hence, the two free parameters of our fit-model are the most frequent decay rate γ^{mf}, at which the log-normal distribution is centered, and the rate distribution width $\Delta\gamma$. The fitted most frequent decay rates are shown in Fig. 2.6, center, and Fig. 2.7, center, together with a fit to the LDOS for isotropically oriented dipoles. We would like to point out that as we fit the Drexhage model to just the retrieved γ^{mf}, the extracted values we quote quantify only the most frequently occurring decay rates and quantum efficiencies, and not the width of the underlying distribution. For the quantum dots we find a most frequent intrinsic radiative decay rate of $(5.46 \pm 0.51)\,\mu\mathrm{s}^{-1}$, a most frequent nonradiative decay rate of $(0.62 \pm 0.66)\,\mu\mathrm{s}^{-1}$ and a most frequent quantum efficiency of $90\% \pm 11\%$ for the emitter hypothetically in vacuum. In its actual bulk host material, i.e., bulk S1813 we find

a most frequent radiative decay rate of $(9.00 \pm 0.84)\,\mu s^{-1}$ and a quantum efficiency of around $94\% \pm 7\%$.

The high quantum efficiency for these quantum dots makes them exceptionally promising for plasmon quantum optics, since operating at 800 nm optimizes the emission frequency to be at the intersection of low plasmon loss, yet efficient silicon detection. The high quantum efficiency is surprising given that the solvent/ligand exchange to aqueous condition, and operation of quantum dots unprotected against oxygen as in our experiment usually adversely affects the photophysical properties. Here we note that measuring quantum efficiency via modulation of radiative lifetime selectively measures the quantum efficiency of the ensemble of dots that radiate, i.e., that are not temporarily or permanently dark due to (photo)chemical processes such as bleaching or blinking. This property should be contrasted to absorption/emission brightness measurements that report quantum efficiency as the fraction of absorbed photons that is converted into radiated photons by an ensemble of nanocrystals. In such measurements a mixture of a dark subensemble that absorbs but does not emit with a subensemble of unit-efficiency emitters is indistinguishable from a homogeneous sample of emitters with below-unit quantum efficiency. The conclusion from our measurement is that those dots that are not (photo)chemically altered by an oxygen-rich or aqueous environment, retain high quantum efficiency. A similar conclusion that the quantum efficiency of those dots that radiate is much higher than the ensemble efficiency obtained from a absorption/emission brightness measurements was also reached by Leistikow [23], for CdSe quantum dots emitting around 600 nm, with efficiencies between 66% and 89%. Evidently, the CdSeTe/ZnS core shell dots emitting at 800 nm have a 6-fold longer lifetime compared to CdSe quantum dots, consistent with observations by Vion et al. [35]. It is remarkable that the (bright) 800 nm dots in our work manage to retain a very high quantum efficiency, despite this 6-fold longer lifetime [23].

An interesting alternative to the quantum dots, which while efficient, have a slow and non-single exponential decay, could be DBT with an emission wavelength of ≈ 750 nm [36, 37]. DBT was recently reported to be ultrastable and ultrabright as an emitter at room temperature [37]. In contrast to Toninelli's observations on single molecules, we observe a non-single exponential decay trace for ensembles of DBT molecules. Therefore, we apply the same analysis scheme as for the quantum dots: log-normally distributed decay rates [41]. In this manner we find a most frequent intrinsic radiative decay rate of $(0.05 \pm 0.01)\,ns^{-1}$, a most frequent nonradiative decay rate of $(0.27 \pm 0.01)\,ns^{-1}$ and a most frequent quantum efficiency of $16\% \pm 3\%$, when calculating with the radiative rate extrapolated to vacuum. Decay rate data and LDOS fit for DBT are shown in Fig. 2.6, right

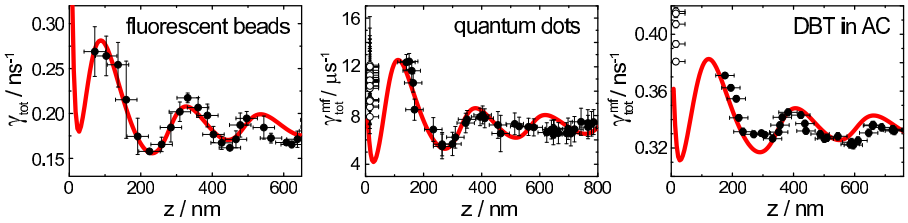

Figure 2.6: Fitted total decay rates $\gamma_{\mathrm{tot}}^{\mathrm{mf}}$ vs distance to the mirror z (black dots). White circles are fitted values to decay traces gathered right on top of the mirror (next to the wedge, $z \approx 0$) and plotted at a fixed height offset from zero for good visibility. The lines indicate fitted relative LDOS ρ_{iso} for isotropically oriented dipoles.

and Fig. 2.7, right. Since DBT is always used in anthracene, it is useful to extract the quantum efficiency in bulk anthracene. Correcting for the index of refraction of anthracene, we find a most frequent radiative decay rate of $(0.09 \pm 0.02)\,\mathrm{ns}^{-1}$ and a quantum efficiency around $24\% \pm 4\%$.

The moderate to low quantum efficiency that our measurement retrieves for DBT is surprising, since Toninelli et al. [37] have reported very high count rates from single DBT molecules in anthracene at room temperature. In saturation, they reported detecting photons at a rate of up to 0.5% of the inverse lifetime. A quantum efficiency of around 25% is within, but at the low end of, the range of values that are consistent with the observation of Toninelli et al. [37], depending on the actual microscope collection efficiency (state of the art: a few percent at 800 nm). We note that the observations of Toninelli et al. [37] are strictly for individual molecules selected to be ideal in the sense of being long lived, which likely selects molecules from those 10% best incorporated in the anthracene matrix. While agreement with LDOS theory for isotropic dipole orientations is good, we found poor agreement of decay rate data to LDOS lineshapes for specific dipole orientations, despite reports of preferential orientation for this system [37]. This further highlights that we probe a heterogeneously distributed ensemble of emitters, as opposed to selecting particular emitters as in single molecule experiments [37]. From observation of the film quality, we note that it was difficult to obtain homogeneous anthracene crystal films throughout the entire wedge length, both on the wedge material as well as on clean cover slips.

Tab. 2.1 summarizes the retrieved radiative and nonradiative decay constants and respective quantum efficiencies for all three fluorophores.

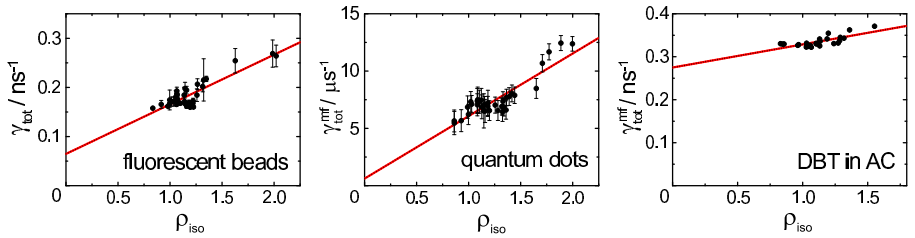

Figure 2.7: Total decay rates $\gamma_{\mathrm{tot}}^{\mathrm{mf}}$ vs relative LDOS ρ_{iso} for isotropically oriented dipoles. The lines indicate fits according to eq.2.1.

	Invitrogen Fluospheres F8801	Invitrogen Qdot 800 ITK carboxyl	DBT in AC
$\gamma_{\mathrm{rad,host}}^{\mathrm{mf}}$	$(0.15\pm0.01)\,\mathrm{ns}^{-1}$	$(9.00 \pm 0.84)\,\mu\mathrm{s}^{-1}$	$(0.09\pm0.02)\,\mathrm{ns}^{-1}$
$\gamma_{\mathrm{nonrad}}^{\mathrm{mf}}$	$(0.07\pm0.01)\,\mathrm{ns}^{-1}$	$(0.62 \pm 0.66)\,\mu\mathrm{s}^{-1}$	$(0.27\pm0.01)\,\mathrm{ns}^{-1}$
$q.e._{\mathrm{host}}^{\mathrm{mf}}$	$71\% \pm 6\%$	$94\% \pm 7\%$	$24\% \pm 4\%$

Table 2.1: Table of emitter properties retrieved from our Drexhage experiments. As we assumed a log-normal distribution of decay rates for the probed Invitrogen Qdot and DBT ensembles, the stated decay rates and quantum efficiencies are the ones which are most-frequent (superscript 'mf'). Radiative decay rates and quantum efficiencies are quoted for the emitters embedded in their respective host medium: PMMA (Fluospheres), S1813 (quantum dots), and anthracene (DBT).

2.7 Conclusions and outlook

In conclusion, we have demonstrated that gray-tone UV-lithography [26] provides a facile method to create samples to calibrate ensembles of emitters. The essential steps of this method are (1) gray-tone lithography to create S1813 or PMMA polymer wedges on flat reflective substrates, such as an Ag or Au mirror, (2) a homogeneous dispersal method to distribute fluorophores on the wedge, and (3) lifetime measurements along the length of the wedge to effectuate Drexhage experiments [19]. Previous methods rather used controlled stepped etching into substrates that had the light sources embedded in them, i.e., a material-specific technique suited for III-V sources [24], or depended on the creation of a large but discrete set of substrates with different deposition thicknesses of dielectric spacer layer [23]. Instead, our method allows to create a continuous wedge on a single sub-

strate. Our method can thus be of large use for calibrating a range of fluorophores for applications ranging from quantum optics, to organic and inorganic light emitting diodes. We note that a large range of variations is easily implemented. For instance, if surface chemistry means it is advantageous to first deposit the fluorophores on glass, then create a wedge, and then deposit a mirror, this is equally easily implemented. Beyond calibration of unknown emitters using a known LDOS, the same method is also of large interest to do the reverse, i.e., to measure an *unknown* LDOS using a calibrated emitter. Indeed, in plasmonics, metamaterials, and the new field of metasurfaces, one frequently encounters questions that revolve around the LDOS at controlled distance. Consider for instance the optimization of light emitting diodes by plasmon particle array surfaces [6, 8, 9] or extraordinary transmission gratings [44]. The question at which distance one should optimally place the emitters to both enhance outcoupling, radiative rate, and quantum efficiency is of key importance, yet difficult to address experimentally. Likewise, the fundamental study of effective medium parameters of metamaterials come to mind. Photonic metamaterials are artificial materials with periodic arrangements of subwavelength scatterers aimed at arbitrary control of permittivity ϵ and permeability μ to realize perfect lenses and invisibility cloaks via transformation optics [45, 46, 47, 48]. For a wide range of metamaterials ϵ and μ have been reported [49, 50, 51], showing that it is indeed possible to obtain, e.g., effectively negative μ. Effective medium constants are commonly retrieved from *far-field* experiments. Since metamaterials have intrinsic near-field benefits, it is interesting to test whether these effective material parameters retrieved from far-field measures such as transmittance and reflectance, are still valid in the near field. Using our wedge technique one can continuously sweep source height through the near field zone to examine the transition from resolving individual building blocks to resolving just the effective parameters [52, 53]. The polymer wedges that we fabricate can indeed also be readily made on patterned surfaces, thereby opening the road to controllably vary the near-field spacing and measure the metamaterial LDOS. This method is complementary to elaborate near-field scanning methods [34]. The loss of lateral resolution in our method compared to near-field scanning is offset by the ease of use of the gray-tone lithography wedge technique, and the fact that in many applications (e.g., plasmon enhanced LEDs) the only useful quantity would anyway be of ensemble averaged nature.

2.8 References

[1] R. H. Friend, R. W. Gymer, A. B. Holmes, J. H. Burroughes, R. N. Marks, C. Taliani, D. D. C. Bradley, D. A. D. Santos, J. L. Bredas, M. Logdlund, and W. R. Salaneck, *Electroluminescence in conjugated polymers*, Nature **397**, 121 (1999).

[2] A. P. Alivisatos, *Semiconductor clusters, nanocrystals, and quantum dots*, Science **271**, 933 (1996).

[3] S. Nakamura, III − V *nitride based light-emitting devices*, Sol. Stat. Comm. **102**, 237 (1997).

[4] C. B. Murray, D. J. Norris, and M. G. Bawendi, *Synthesis and characterization of nearly monodisperse* CdE *(*E = *sulfur, selenium, tellurium) semiconductor nanocrystallites*, J. Am. Chem. Soc. **115**, 8706 (1993).

[5] C. M. Soukoulis, editor, *Photonic Crystals and Light Localization in the 21st Century*, Kluwer Academic Publishers, 2001.

[6] A. V. Zayats, I. I. Smolyaninov, and A. A. Maradudin, *Nano-optics of surface plasmon polaritons*, Phys. Rep. **408**, 131 (2005).

[7] P. Mühlschlegel, H.-J. Eisler, O. J. F. Martin, B. Hecht, and D. W. Pohl, *Resonant optical antennas*, Science **308**, 1607 (2005).

[8] O. L. Muskens, V. Giannini, J. A. Sánchez-Gil, and J. Gómez Rivas, *Strong enhancement of the radiative decay rate of emitters by single plasmonic nanoantennas*, Nano Lett. **7**, 2871 (2007).

[9] G. Vecchi, V. Giannini, and J. Gómez Rivas, *Shaping the fluorescent emission by lattice resonances in plasmonic crystals of nanoantennas*, Phys. Rev. Lett. **102**, 146807 (2009).

[10] P. Lodahl, A. F. van Driel, I. S. Nikolaev, A. Irman, K. Overgaag, D. Vanmaekelbergh, and W. L. Vos, *Controlling the dynamics of spontaneous emission from quantum dots by photonic crystals*, Nature **430**, 654 (2004).

[11] R. Sprik, B. A. van Tiggelen, and A. Lagendijk, *Optical emission in periodic dielectrics*, Eur. Phys. Lett. **35**, 265 (1996).

[12] L. Novotny and B. Hecht, *Principles of Nano-Optics*, Cambridge University Press, Cambridge, 2006.

[13] P. Bertet, A. Auffeves, P. Maioli, S. Osnaghi, T. Meunier, M. Brune, J. M. Raimond, and S. Haroche, *Direct measurement of the wigner function of a one-photon fock state in a cavity*, Phys. Rev. Lett. **89**, 200402 (2002).

[14] B. Lounis and M. Orrit, *Single-photon sources*, Rep. Prog. Phys. **68**, 1129 (2005).

[15] J. R. Lakowicz, *Principles of Fluorescence Spectroscopy*, Springer, 2006.

[16] K. H. Drexhage, H. Kuhn, and F. P. Schäfer, *Variation of the fluorescence decay time of a molecule in front ofa mirror*, Ber. Buns. f. Phys. Chem. **72**, 329 (1968).

[17] K. Drexhage, *Influence of a dielectric interface on fluorescence decay time*, J. Lumin. **1 & 2**, 693 (1970).

[18] R. M. Amos and W. L. Barnes, *Modification of the spontaneous emission rate of* Eu^{3+} *ions close to a thin metal mirror*, Phys. Rev. B **55**, 7249 (1997).

[19] E. Snoeks, A. Lagendijk, and A. Polman, *Measuring and modifying the spontaneous emission rate of erbium near an interface*, Phys. Rev. Lett. **74**, 2459 (1995).

[20] B. C. Buchler, T. Kalkbrenner, C. Hettich, and V. Sandoghdar, *Measuring the quantum efficiency of the optical emission of single radiating dipoles using a scanning mirror*, Phys. Rev. Lett. **95**, 063003 (2005).

[21] R. R. Chance, A. Prock, and R. Silbey, *Molecular fluorescence and energy transfer near interfaces*, Adv. Chem. Phys. **37**, 1 (1978).

[22] M. J. A. de Dood, L. H. Slooff, A. Polman, A. Moroz, and A. van Blaaderen, *Modified spontaneous emission in erbium-doped* SiO_2 *spherical colloids*, Appl. Phys. Lett. **79**, 3585 (2001).

[23] M. D. Leistikow, J. Johansen, A. J. Kettelarij, P. Lodahl, and W. L. Vos, *Size-dependent oscillator strength and quantum efficiency of cdse quantum dots controlled via the local density of states*, Phys. Rev. B **79**, 045301 (2009).

[24] S. Stobbe, J. Johansen, P. T. Kristensen, J. M. Hvam, and P. Lodahl, *Frequency dependence of the radiative decay rate of excitons in self-assembled quantum dots: Experiment and theory*, Phys. Rev. B **80**, 155307 (2009).

[25] Q. Wang, S. Stobbe, and P. Lodahl, *Mapping the local density of optical states of a photonic crystal with single quantum dots*, Phys. Rev. Lett. **107**, 167404 (2011).

[26] M. Christophersen and B. F. Phlips, *Gray-tone lithography using an optical diffuser and a contact aligner*, Appl. Phys. Lett. **92**, 194102 (2008).

[27] A. V. Akimov, A. Mukherjee, C. L. Yu, D. E. Chang, A. S. Zibrov, P. R. Hemmer, H. Park, and M. D. Lukin, *Generation of single optical plasmons in metallic nanowires coupled to quantum dots*, Nature **450**, 402 (2007).

[28] D. E. Chang, A. S. Sørensen, E. A. Demler, and M. D. Lukin, *A single-photon transistor using nanoscale surface plasmons*, Nat. Phys. **3**, 807 (2007).

[29] A. G. Curto, G. Volpe, T. H. Taminiau, M. P. Kreuzer, R. Quidant, and N. F. van Hulst, *Unidirectional emission of a quantum dot coupled to a nanoantenna*, Science **329**, 930 (2010).

[30] A. F. Koenderink, *Plasmon nanoparticle array waveguides for single photon and single plasmon sources*, Nano Lett. **9**, 4228 (2009).

[31] J. B. Pendry and D. R. Smith, *Reversing light with negative refraction*, Physics Today **57**, 37 (2004).

[32] V. M. Shalaev, *Optical negative-index metamaterials*, Nat. Photon. **1**, 41 (2007).

[33] C. M. Soukoulis and M. Wegener, *Past achievements and future challenges in the development of three-dimensional photonic metamaterials*, Nat. Photon. **5**, 523 (2011).

[34] M. Frimmer, Y. Chen, and A. F. Koenderink, *Scanning emitter lifetime imaging microscopy for spontaneous emission control*, Phys. Rev. Lett. **107**, 123602 (2011).

[35] C. Vion, C. Barthou, P. Bénalloul, C. Schwob, L. Coolen, A. Gruzintev, G. Emel'chenko, V. Masalov, J.-M. Frigerio, and A. Maître, *Manipulating emission of cdtese nanocrystals embedded in three-dimensional photonic crystals*, J. Appl. Phys. **105**, 113120 (2009).

[36] F. Jelezko, P. Tamarat, B. Lounis, and M. Orrit, *Dibenzoterrylene in naphthalene: A new crystalline system for single molecule spectroscopy in the near infrared*, J. Phys. Chem. **100**, 13892 (1996).

[37] C. Toninelli, K. Early, J. Bremi, A. Renn, S. Götzinger, and V. Sandoghdar, *Near-infrared single-photons from aligned molecules in ultrathin crystalline-films at room temperature*, Opt. Express **18**, 6577 (2010).

[38] Ž. Bajzer, T. M. Therneau, J. C. Sharp, and F. G. Prendergast, *Maximum likelihood method for the analysis of time-resolved fluorescence decay curves*, Eur. Biophys. J. **20**, 247 (1991).

[39] M. Paulus, P. Gay-Balmaz, and O. J. F. Martin, *Accurate and efficient computation of the Green's tensor for stratified media*, Phys. Rev. E **62**, 5797 (2000).

[40] W. L. Vos, A. F. Koenderink, and I. S. Nikolaev, *Orientation-dependent spontaneous emission rates of a two-level quantum emitter in any nanophotonic environment*, Phys. Rev. A **80**, 053802 (2009).

[41] A. F. van Driel, I. S. Nikolaev, P. Vergeer, P. Lodahl, D. Vanmaekelbergh, and W. L. Vos, *Statistical analysis of time-resolved emission from ensembles of semiconductor quantum dots: Interpretation of exponential decay models*, Phys. Rev. B **75**, 035329 (2007).

[42] I. S. Nikolaev, P. Lodahl, A. F. van Driel, A. F. Koenderink, and W. L. Vos, *Strongly nonexponential time-resolved fluorescence of quantum-dot ensembles in three-dimensional photonic crystals*, Phys. Rev. B **75**, 115302 (2007).

[43] P. Lunnemann, F. T. Rabouw, R. J. A. van Dijk-Moes, F. Pietra, D. Vanmaekelbergh, and A. F. Koenderink, *Calibrating and controlling the quantum efficiency distribution of inhomogeneously broadened quantum rods by using a mirror ball*, ACS Nano **7**, 5984 (2013).

[44] T. W. Ebbesen, H. J. Lezec, H. F. Ghaemi, T. Thio, and P. A. Wolff, *Extraordinary optical transmission through sub-wavelength hole arrays*, Nature **391**, 667 (1998).

[45] J. B. Pendry, *Negative refraction makes a perfect lens*, Phys. Rev. Lett. **85**, 3966 (2000).

[46] J. Valentine, J. Li, T. Zentgraf, G. Bartal, and X. Zhang, *An optical cloak made of dielectrics*, Nat. Mater. **8**, 568 (2009).

[47] T. Ergin, N. Stenger, P. Brenner, J. B. Pendry, and M. Wegener, *Three-dimensional invisibility cloak at optical wavelengths*, Science **328**, 337 (2010).

[48] T. Zentgraf, J. Valentine, N. Tapia, J. Li, and X. Zhang, *An optical "Janus" device for integrated photonics*, Adv. Mater. **22**, 2561 (2010).

[49] R. A. Shelby, D. R. Smith, and S. Schultz, *Experimental verification of a negative index of refraction*, Science **292**, 77 (2001).

[50] G. Dolling, C. Enkrich, M. Wegener, C. M. Soukoulis, and S. Linden, *Simultaneous negative phase and group velocity of light in a metamaterial*, Science **312**, 892 (2006).

[51] J. Valentine, S. Zhang, T. Zentgraf, E. Ulin-Avila, D. A. Genov, G. Bartal, and X. Zhang, *Three-dimensional optical metamaterial with a negative refractive index*, Nature **455**, 376 (2008).

[52] J. Kästel and M. Fleischhauer, *Suppression of spontaneous emission and superradiance over macroscopic distances in media with negative refraction*, Phys. Rev. A **71**, 011804 (2005).

[53] H. T. Dung, S. Y. Buhmann, L. Knöll, D.-G. Welsch, S. Scheel, and J. Kästel, *Electromagnetic-field quantization and spontaneous decay in left-handed media*, Phys. Rev. A **68**, 043816 (2003).

Chapter 3

Probing the electrodynamic LDOS with magnetoelectric point scatterers

In a scattering experiment, the induced dipole moments of a magnetoelectric point scatterer in response to driving fields are given by its polarizability tensor $\boldsymbol{\alpha}$. Its linewidth will be dictated by the local density of optical states (LDOS) at the scatterer's position. To retrieve the magnetoelectric cross-coupling components of $\boldsymbol{\alpha}$ for an archetypical magnetoelectric scatterer—a split ring resonator—we study the frequency dependent extinction cross section σ_{ext} as a function of distance to an interface. Rather than following a purely electric or purely magnetic LDOS, we find a dependence which reflects the interplay of both dipole moments in a 'mixed' magnetoelectric LDOS. For a strongly magnetoelectric cross-coupled microwave scatterer, we compare analytical point dipole with finite element method calculations.

3.1 Introduction

While electricity and magnetism are inextricably connected in optics, the interaction of light with matter is generally considered to be almost entirely mediated by the photon's electric field and the electric polarizability of matter [1]. In the last decade, this paradigm has shifted with the emergence of the field of metamaterials [2, 3, 4]. In this field of research, complete control over the flow of light is promised by transformation optics [5], provided one can engineer arbitrary AC (optical frequency ω) permittivity $\varepsilon(\omega)$ and permeability $\mu(\omega)$ of the medium it passes through. To reach this goal, many workers nanostructure materials that intrinsically have $\mu = 1$ and $\varepsilon \neq 1$ to create effective media that *spoof* a magnetic response μ. The workhorse object in the field is the so called split ring resonator [6, 7, 8, 9, 10, 11, 12, 13, 14, 15, 16], a metallic ring of an overall size of around $\lambda/10$ with a single cut that provides a magnetic response through a circulating charge mode that corresponds to an LC-resonance. At telecom frequencies, experiments indicate that split rings, and similar metamaterial building blocks, have a strong magnetic polarizability of several times their physical volume [10, 13, 14]. Therefore, it is possible to induce a strong magnetic dipole in such scatterers upon driving with the incident magnetic field of light. At the same time, metamaterial scatterers often feature a strong electric, and a so-called 'magnetoelectric' polarizability, whereby electric driving sets up a strong magnetic response and vice versa [17].

Parallel to the development of metamaterials, interest recently emerged in engineering magnetic fluorescent transitions [18, 19, 20, 21]. Just as the response of materials to light is dominated in nature by ε, the fluorescence of deeply subwavelength objects like atoms, quantum dots and molecules, is usually entirely dominated by electric dipole transitions [22]. Thus, researchers in the field of spontaneous emission control conventionally take the local density of optical states (LDOS), that quantifies how many photon states are available for an emitter to decay into, as strictly meaning the local density of *electric field* vacuum fluctuations. This electric field LDOS not only governs spontaneous emission, but is also commonly associated to, e.g., light generation by cathodoluminescence [23, 24], or the radiative damping of plasmonic, i.e., purely electrically polarizable, scatterers as measured by Buchler et al. [25]. While in context of spontaneous emission, the magnetic LDOS, i.e., the local density of *magnetic field* vacuum fluctuations, usually plays a negligible role, it was already recognized to be equally important as the electric LDOS in determining the local energy density of the thermal field as reviewed by Joulain et al. [26, 27, 28]. Very recently Taminiau et al. [21] demonstrated that in rare earth elements magnetic transition dipoles

can be sufficiently strong for magnetic LDOS to be cleanly observed.

In this chapter, the two developments described above come together in a single question and its answer. If a scatterer such as a split ring is indeed a magnetic, or even a magnetoelectric scatterer of mixed electric-magnetic character, which LDOS actually sets the radiative linewidth? To formalize this question, we ask how radiation damping affects a split ring if we abstract it to a point scatterer with a formally 6×6 polarizability [29, 7] of the form

$$\begin{pmatrix} \boldsymbol{p} \\ \boldsymbol{m} \end{pmatrix} = \begin{pmatrix} \boldsymbol{\alpha}_E & \boldsymbol{\alpha}_C \\ -\boldsymbol{\alpha}_C^T & \boldsymbol{\alpha}_H \end{pmatrix} \begin{pmatrix} \boldsymbol{E} \\ \boldsymbol{H} \end{pmatrix}. \tag{3.1}$$

Here, the electric response to electric fields and magnetic response to magnetic fields are given by the 3×3 tensors $\boldsymbol{\alpha}_E$ and $\boldsymbol{\alpha}_H$, respectively. The off-diagonal quantifies how strongly a magnetic dipole can be set up by an electric field and vice versa. A polarizability such as Eq. (3.1) contains very nontrivial features, such as optical activity, pseudochirality, and handed radiation patterns, depending on the amount of magnetoelectric cross-coupling $\boldsymbol{\alpha}_C$ [30, 17, 31]. In how far this polarizability truly describes experiments is a matter of debate. Matching of far-field transmission spectra of periodic arrangements of such metamaterial scatterers to a lattice model for point dipoles is excellent [32] but one may wonder if the dipole picture stands up to scrutiny in a near-field experiment. A particular near-field experiment would be to test if a split ring responds to the LDOS, a quantity specific to dipole transitions and scattering. In this chapter, we first answer the question how a split ring's radiative linewidth is modified by the LDOS, and show that in addition to the electric and magnetic LDOS, a third quantity emerges in the form of a magnetoelectric LDOS. Secondly, we show that controlled variations in LDOS should allow one to measure the magnitude and test the conceptual validity of the point scatterer's polarizability. Finally, we benchmark our proposal to finite element calculations.

3.2 Magnetic LDOS near metallic and dielectric interfaces

The effect of the LDOS on a point scatterer is well understood by first considering a polarizable dipole in front of a perfect mirror. As first demonstrated in a groundbreaking experiment by Buchler et al. [25], the scattering resonance of a plasmon particle can be modified in width by mechanically approaching a planar reflective substrate. This effect can be interpreted in exactly the same manner as the explanation usually given to Drexhage's experiment on the radiative transition rate of a fluorophore near a mirror [33, 34, 35, 36, 37]. The scattering resonance carries an electric dipole

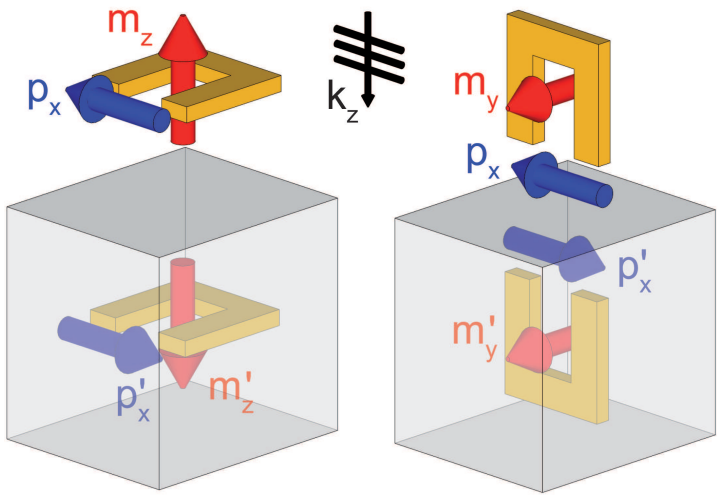

Figure 3.1: Split ring resonators with two distinct orientations are placed above a perfect mirror. In the point dipole picture each split ring is described by an electric dipole $\boldsymbol{p}$ along the split ring gap and a magnetic dipole $\boldsymbol{m}$ pointing out of the split ring plane. The mirror images for both split ring orientations are depicted together with their respective image dipoles $\boldsymbol{p'}$ and $\boldsymbol{m'}$.

that hybridizes with its mirror image, which for a dipole moment parallel (perpendicular) to a perfect mirror interface has reverse (identical) orientation according to image charge analysis (Fig. 3.1). The two electric dipoles together correspond to either a subradiant or superradiant configuration, depending on dipole orientation and distance. Consequently, the radiative linewidth oscillates with distance to the mirror in proportion to the electric LDOS. It is not immediately obvious that this method can be useful to also probe linewidth changes in objects such as split rings, with both an electric and magnetic dipole moment. While the rule for choosing the image dipole orientation reverses in the magnetic case, compared to the electric case, one should also consider that in a split ring the electric and magnetic dipole are at 90° relative orientation. In most experiments, the magnetic dipole is perpendicular to the substrate (labelled z-oriented from hereon), while the electric dipole is in-plane (x-oriented). An image dipole analysis assuming a perfect mirror predicts essentially no discernible difference between the linewidth of an in-plane electric dipole and an out-of-plane magnetic dipole. That electric and magnetic LDOS have essentially the same dependence for the perpendicular dipole orientations in a mirror charge analysis was also noted by Karaveli et al. [18]. Discerning magnetic and electric LDOS effects

hence either implies that one rotates the scatterer (Fig. 3.1, right) to have both electric and magnetic dipoles in plane, or requires that one finds an LDOS with distinct electric and magnetic spatial dependence for the desired polarizations.

3.3 Green function

To calculate LDOS, we require the 6×6 dyadic Green function near a planar interface where source $\mathbf{r}'$ and observation point $\mathbf{r}$ are in the same halfspace.We separate the Green function in a free part (in absence of an interface) and a reflected part

$$\mathbf{G}(\mathbf{r}, \mathbf{r}') = \mathbf{G}_{\text{free}}(\mathbf{r}, \mathbf{r}') + \mathbf{G}_{\text{reflected}}(\mathbf{r}, \mathbf{r}')$$

with

$$\mathbf{G}_{\text{free}}(\mathbf{r}, \mathbf{r}') = \begin{pmatrix} \mathbb{I}k^2 + \nabla\nabla & -ik\nabla\times \\ ik\nabla\times & \mathbb{I}k^2 + \nabla\nabla \end{pmatrix} G(\mathbf{r}, \mathbf{r}') \tag{3.2}$$

where $k = \omega n/c$ is the wave number in the medium of index n that contains both $\mathbf{r}$ and $\mathbf{r}'$, c is the speed of light, and $G(\mathbf{r}, \mathbf{r}')$ is the scalar Green function. The reflected part of the Green function reads

$$\begin{aligned} \mathbf{G}_{\text{reflected}}(\mathbf{r}, \mathbf{r}') &= \frac{ik^2}{2} \int_0^\infty k_{||} dk_{||} [j_0(k_{||}R)\mathbf{M}_0 + \\ &\quad j_1(k_{||}R)\mathbf{M}_1 + j_2(k_{||}R)\mathbf{M}_2] e^{ik_z z} \end{aligned} \tag{3.3}$$

where if $\mathbf{r} = (x, y, z)$ and $\mathbf{r}' = (x', y', z')$ we define cylindrical coordinates through $(R\cos\phi, R\sin\phi, Z) = (x - x', y - y', z + z')$. With k_z we denote $\sqrt{k^2 - ||k_{||}||^2}$, while $j_n(x)$ is the Bessel function of order n. The 6×6 matrices $\mathbf{M}_i$ contain the $k_{||}$ dependent Fresnel reflection coefficients r_s and r_p for s and p polarization. In detail:

$$\mathbf{M}_0 = \begin{pmatrix} r_s/k_z - r_p k_z & 0 & 0 \\ 0 & r_s/k_z - r_p k_z & 0 \\ 0 & 0 & 2r_p k_{||}^2/k_z \\ 0 & r_p - r_s & 0 \\ r_s - r_p & 0 & 0 \\ 0 & 0 & 0 \end{pmatrix}$$

$$\begin{pmatrix} 0 & r_p - r_s & 0 \\ r_s - r_p & 0 & 0 \\ 0 & 0 & 0 \\ r_p/k_z - r_s k_z & 0 & 0 \\ 0 & r_p/k_z - r_s k_z & 0 \\ 0 & 0 & 2r_s k_{||}^2/k_z \end{pmatrix} \tag{3.4}$$

and

$$\mathbf{M}_1 = 2ik_{||} \begin{pmatrix} 0 & 0 & -r_p \cos\phi \\ 0 & 0 & -r_p \sin\phi \\ r_p \cos\phi & r_p \sin\phi & 0 \\ 0 & 0 & r_p/k_z \sin\phi \\ 0 & 0 & -r_p/k_z \cos\phi \\ -r_s/k_z \sin\phi & r_s/k_z \cos\phi & 0 \end{pmatrix}$$

$$\begin{pmatrix} 0 & 0 & -r_s/k_z \sin\phi \\ 0 & 0 & r_s/k_z \cos\phi \\ r_p/k_z \sin\phi & -r_p/k_z \cos\phi & 0 \\ 0 & 0 & -r_s \cos\phi \\ 0 & 0 & -r_s \sin\phi \\ r_s \cos\phi & r_s \sin\phi & 0 \end{pmatrix} \tag{3.5}$$

and finally also

$$\mathbf{M}_2 = \begin{pmatrix} (r_s/k_z + r_p k_z)\cos 2\phi & (r_s/k_z + r_p k_z)\sin 2\phi & 0 \\ (rs/k_z + r_p k_z)\sin 2\phi & -(r_s/k_z + r_p k_z)\cos 2\phi & 0 \\ 0 & 0 & 0 \\ -(r_s + r_p)\sin 2\phi & (r_s + r_p)\cos 2\phi & 0 \\ (r_s + r_p)\cos 2\phi & (r_s + r_p)\sin 2\phi & 0 \\ 0 & 0 & 0 \end{pmatrix}$$

$$\begin{pmatrix} (r_s + r_p)\sin 2\phi & -(r_s + r_p)\cos 2\phi & 0 \\ -(r_s + r_p)\cos 2\phi & -(r_s + r_p)\sin 2\phi & 0 \\ 0 & 0 & 0 \\ (r_s k_z + r_p/k_z)\cos 2\phi & (r_s k_z + r_p/k_z)\sin 2\phi & 0 \\ (r_s k_z + r_p/k_z)\sin 2\phi & -(r_s k_z + r_p/k_z)\cos 2\phi & 0 \\ 0 & 0 & 0 \end{pmatrix}. \tag{3.6}$$

Throughout we have used the units of Ref. [17].

To specify the calculation method for the LDOS at a position $\mathbf{r}$ above the interface, we calculated the imaginary part of the Green function $\boldsymbol{G}(\mathbf{r}, \mathbf{r})$, as described in the textbook by Novotny and Hecht [22], using the complex wave vector integration contour of Paulus et al. [38]. From hereon we

suppress the argument of the Green function. We generalize the calculation to encompass the electric LDOS $\mathrm{Im}\boldsymbol{G}_{EE}$, the magnetic LDOS $\mathrm{Im}\boldsymbol{G}_{HH}$ and the crossed Green dyadic $\mathrm{Im}\boldsymbol{G}_{EH}$. Notably, the calculation of magnetic and electric LDOS is comparable in methodology to the report by Joulain et al. [27], with the distinction that we do not average over dipole orientation, specify how to implement the full Green function $\boldsymbol{G}(\mathbf{r}', \mathbf{r})$ at arbitrary distinct source and detector coordinate, and include the magnetoelectric cross term.

In Fig. 3.2, we plot the electric and magnetic LDOS for vacuum/Si and vacuum/Ag interfaces for both parallel and perpendicular dipole orientations with the aim of obtaining a large difference between the LDOS for x-oriented electric dipoles and z-oriented magnetic dipoles. We take $\varepsilon = 12.11$ for silicon and $\varepsilon = -121.53 + 3.10i$ for silver, as tabulated for the resonant wavelength of 1.5 µm [39, 40], typical for 200 nm × 200 nm split rings, and plot LDOS normalized to the LDOS in vacuum (Fig. 3.2). For the vacuum/Ag interface we observe that the magnetic z-oriented and electric x-oriented LDOS are quite similar in magnitude, except within 50 nm of the interface. As anticipated from the perfect mirror intuition, a dielectric interface is advantageous in providing a higher contrast of magnetic electric LDOS contrast compared to a metal. Continuity conditions on $E_{\parallel}$ and $H_{\parallel}$ ensure that the electric and magnetic LDOS are highly distinct. The range over which a large distinction remains away from the interface extends well into the regime beyond the first oscillations in LDOS at 200 nm, as shown in Fig. 3.2. Therefore, scanning the separation distance between split ring and interface allows to independently vary the electric and magnetic LDOS over a substantial range.

3.4 Radiative linewidth near an interface

Now we proceed to examine the radiative linewidth of a point scatterer described by a magnetoelectric polarizability, as proposed by Sersic et al. [17], which is based on the static polarizability introduced by Garcia-Garcia et al. [7] generalized to include radiation damping. The induced dipole moments of a scatterer in vacuum are entirely set by its full 6×6 dynamic polarizability tensor $\alpha_{\mathrm{free}}^{\mathrm{dyn}}$ that is of the form Eq. (3.1). In a quasistatic description of the scatterer, one starts from an LC circuit to obtain a static polarizability $\alpha_{\mathrm{free}}^{\mathrm{stat}}$ that consists of a Lorentzian frequency dependence $\mathcal{L}(\omega) = \frac{\omega_0^2 V}{\omega_0^2 - \omega^2 - i\omega\gamma}$. (resonant at the LC frequency ω_0 , damping rate γ set by the Ohmic resistance R) multiplying a frequency independent 2×2

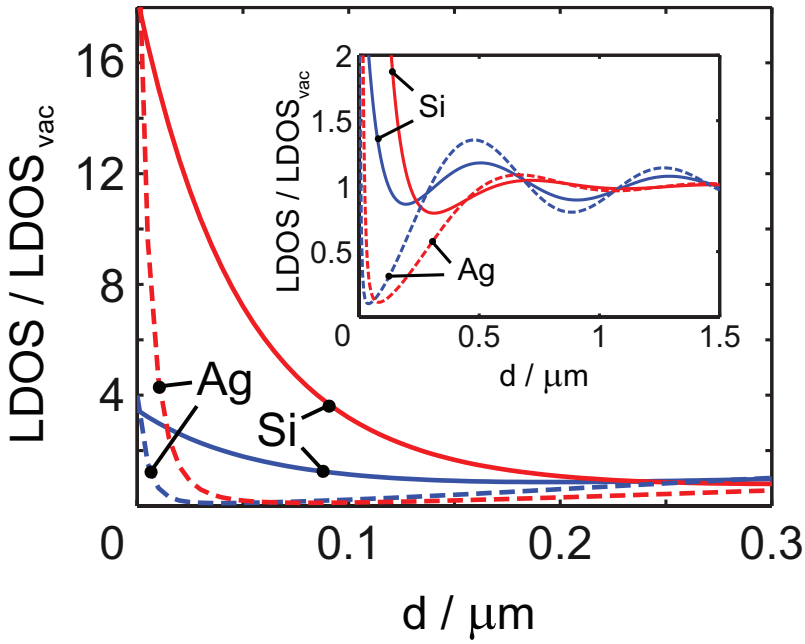

Figure 3.2: Relative electric (x-oriented dipole $\boldsymbol{p}$, dark gray) and magnetic (z-oriented dipole $\boldsymbol{m}$, light gray) LDOS for distance d from a vacuum/Ag (dashed lines) and vacuum/Si (solid lines) interface at a vacuum wavelength of 1.5 µm. Especially at close distances $d < 0.2$ µm, a vacuum/Si interface provides a higher LDOS contrast of x-oriented electric dipoles and z-oriented magnetic dipoles than a vacuum/Ag interface.

matrix

$$\boldsymbol{\alpha}_{\text{free}}^{\text{stat}} = \mathcal{L}(\omega) \begin{pmatrix} \eta_{E,xx} & i\eta_{C,xz} \\ -i\eta_{C,zx} & \eta_{H,zz} \end{pmatrix} \tag{3.7}$$

where η_E, η_H, η_C are real parameters simply set by geometry. For an ideal, infinitely thin SRR all other elements of the 6×6 polarizability are zero. To end up with an energy conserving scatterer, a radiation damping term must be added:

$$\boldsymbol{\alpha}_{\text{free}}^{\text{dyn}\,-1} = \boldsymbol{\alpha}_{\text{free}}^{\text{stat}\,-1} - i\text{Im}\boldsymbol{G}. \tag{3.8}$$

where $\boldsymbol{G}$ is shorthand for the 6×6 Green function $\boldsymbol{G}(\boldsymbol{r}, \boldsymbol{r'})$ evaluated with both $\boldsymbol{r}$ and $\boldsymbol{r'}$ equal to the position of the scatterer. In vacuum the correction amounts to the usual radiation damping term $i\text{Im}\boldsymbol{G} = 2/3ik^3\mathbb{I}$, where $k = \omega/c$, and $\mathbb{I}$ the identity matrix, that is standard in the field of plasmonics. In front of the interface, however, the Green function is

modified according to Fig. 3.2. For the effectively 2×2 polarizability of the split ring, the relevant Im$\mathbf{G}$ tensor is also only 2×2, containing on the diagonal only the electric LDOS for x-oriented dipoles Im$\boldsymbol{G}_{EE,xx}$, and the magnetic LDOS for z-oriented dipoles Im$\boldsymbol{G}_{HH,zz}$, while the off-diagonal contains Im$\boldsymbol{G}_{EH,xz}$. The off-diagonal term, but at distinct spatial coordinates, i.e., Im$\boldsymbol{G}_{EH}(\boldsymbol{r}, \boldsymbol{r'})$, was already recognized to be relevant by Agarwal [26] in the context of fluctuating electromagnetic fields. In that context, the term quantifies coherence in blackbody fluctuations, i.e., as cross-spectral correlation function between electric field at position $\boldsymbol{r}$ and magnetic field measured at position $\boldsymbol{r'}$. In the thermal energy density near simple interfaces as treated by Joulain et al. [27], this cross term does not appear, owing to the fact that it does not contribute to thermal energy density if the fluctuating electric and magnetic currents from which the thermal energy density arises are independent. In this case only the trace of the Green function enters, i.e., the sum of the dipole-orientation averaged electric and magnetic LDOS. However, as soon as bi-(an)isotropy (evident as optical activity) is at play this assumption breaks down and the Im$\boldsymbol{G}_{EH}$ term will enter in transition rates of emitters, radiative linewidths of scatterers and thermal energy density. Indeed, bianisotropy is the hallmark of the LC model for a split ring, in which electric and magnetic dipole derive from the same charge motion, at fixed quarter wave phase difference. We refer to Ref. [41] for a recent treatment of fluctuational electrodynamics in chiral bi-isotropic media.

We obtain the radiative linewidth as one would measure it in an extinction experiment, by calculating the extinction cross section in the following manner. The scatterer is driven by a plane wave impinging from above, plus its Fresnel reflection due to the interface. We take the incident beam as normal to the interface with the electric field polarized along the gap. We calculate the work done per unit cycle on the scatterer via

$$W = \left\langle \mathrm{Re}\boldsymbol{E} \cdot \mathrm{Re}\frac{d\boldsymbol{p}}{dt} + \mathrm{Re}\boldsymbol{H} \cdot \mathrm{Re}\frac{d\boldsymbol{m}}{dt} \right\rangle. \tag{3.9}$$

Plots of the work show an oscillatory dependence with distance of the split ring to the interface, due to two effects. Firstly, the driving field forms a standing wave. Secondly, the polarizability varies with the oscillating LDOS. To obtain a true extinction cross section we divide out the local field strength of the driving

$$\sigma_{\mathrm{ext}} = \frac{2Z}{|\boldsymbol{E}|^2} W, \tag{3.10}$$

with Z the impedance of the host medium, in this case vacuum. As Fig. 3.3(a, inset) shows, the retrieved extinction cross section is of Lorentzian spectral

shape, and varies in width and central frequency as the scatterer is approached to the interface. We extract the resonance width, which is the sum of the radiative and absorptive damping rate of the scatterer.

As a benchmark, Fig. 3.3 shows the linewidth of the extinction cross section of a purely electric scattering sphere, i.e., taking $\eta_E = 1$, $\eta_H = 0$ and $\eta_C = 0$, resonant at 1.5 µm wavelength, with Ohmic damping rate $\gamma = 8.3 \times 10^{13}\ \mathrm{s}^{-1}$ and a particle volume of $V = 100\ \mathrm{nm}^3$. As the scatterer approaches the interface, its extinction linewidth oscillates, and almost doubles when the scatterer is close to the interface. We find that the linewidth Γ follows the dependence $\Gamma = \Gamma_{\mathrm{abs}} + \Gamma_{\mathrm{rad}} \times \mathrm{LDOS}_{EE,xx}$. Analogous to the calibration of quantum efficiencies of fluorophores [35, 36, 37], this dependence allows to extract the radiative and Ohmic damping rate of the particle, and thereby also the LDOS dependent albedo of the scatterer. For the sphere studied here, the albedo in absence of the interface is $a = 0.41$. This benchmark calculation shows that our model reproduces the experimental observation by Buchler et al.[25]. Similarly, a calculation for a purely magnetic scatterer verifies that the damping rate of a magnetic scatterer traces the magnetic LDOS [calculation not shown].

In Fig. 3.3, as a measure for Γ, we examine the extinction linewidth for objects that have both an electric and a magnetic character. For demonstration purposes, we take the electric and magnetic polarizability equally large at $\eta_E = \eta_H = 1$. If no cross-coupling, i.e., no bianisotropy is present in the object ($\eta_C = 0$), the extinction linewidth simply traces the electric LDOS, provided excitation is normal to the sample so that the magnetic dipole is not directly driven at all [curve not shown]. As cross-coupling is introduced, and increased to its maximum value, the extinction linewidth shifts away from the purely electric LDOS, and towards the magnetic LDOS curves. At maximum cross-coupling ($\eta_C = 1$), the extinction linewidth exactly traces the mean of electric and magnetic LDOS consistent with the fact that the induced electric and magnetic dipole are equal in size. Generally, for this geometry and excitation, the averaging is weighted by the magnitudes of the dipole moments, i.e., $|\boldsymbol{p}|^2$ and $|\boldsymbol{m}|^2$. We conclude that an experiment such as performed by Buchler et al.[25], but applied to a split ring can indeed provide a quantitative test of the magnetic and bianisotropic dipole response of a single object, and a calibration of the magnitude of polarizability tensor elements.

3.5 Magnetoelectric LDOS

That a weighted average of electric and magnetic LDOS is obtained for a scatterer with both electric and magnetic dipole moment, may seem a likely

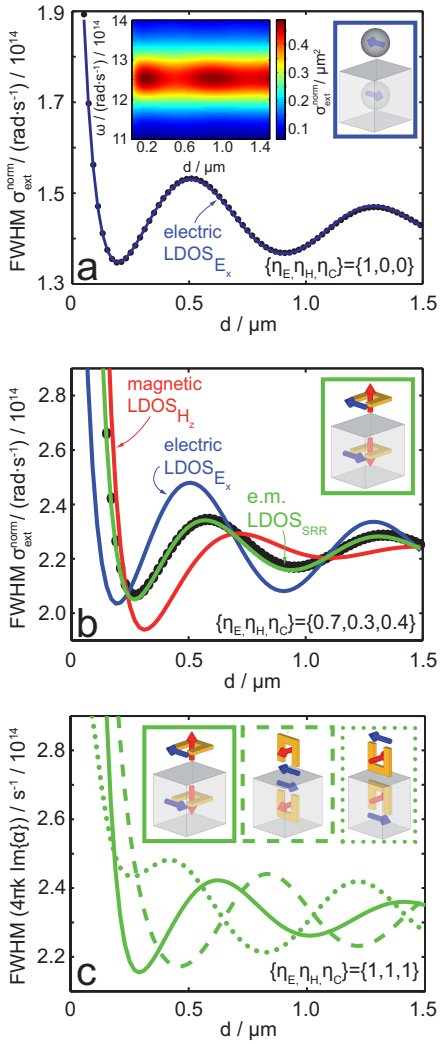

Figure 3.3: (a) Analytical calculation of the FWHM-linewidth of the extinction cross section normalized to driving field intensity as a function of distance d to a vacuum/Si interface for a purely electric ($\eta_E = 1, \eta_H = \eta_C = 0$) sphere resonant at 1.5 µm wavelength, with Ohmic damping rate $\gamma = 8.3 \cdot 10^{13}$ s^{-1} and a particle volume of $V = 100$ nm^3 (dots) in comparison to the purely electric LDOS lineshape for this interface. (b) The dots represent the same quantitity as before, but for a realistic split ring resonator ($\eta_H = 0.7, \eta_E = 0.3, \eta_C = 0.4$)[14] that is oriented with the SRR plane parallel to the surface. Electric, magnetic and magnetoelectric LDOS are shown as lines. (c) Maximally cross-coupled split ring resonator ($\eta_E = \eta_H = \eta_C = 1$) parallel to and with the gap pointing towards and pointing away from the interface, respectively.

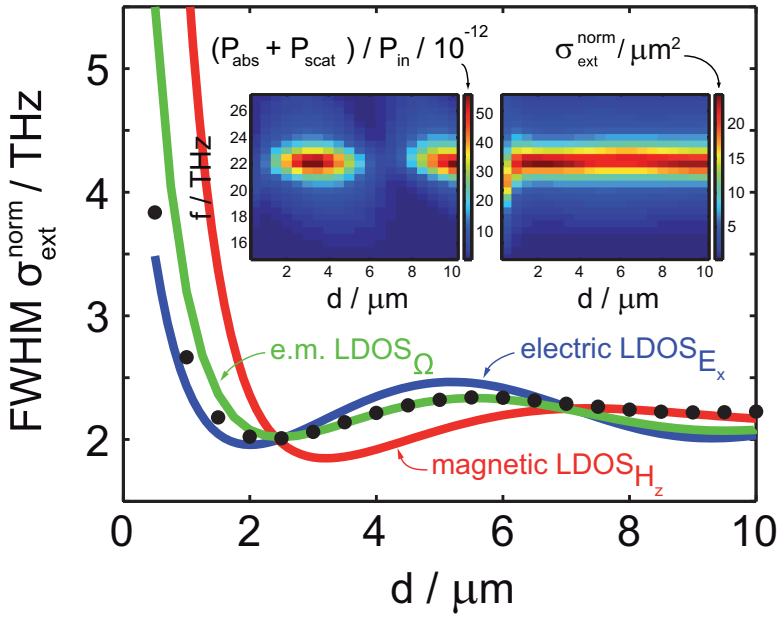

Figure 3.4: FWHM-linewidth of the extinction cross section normalized to the local driving field intensity for a zero arm-length omega particle oriented parallel to a Si interface as a function of distance d. Retrieved FWHM-linewidths from FEM-simulation (dots) vs. point dipole calculation (lines). Insets show extinct power (left) as well as normalized extinction cross section (right) as a function of frequency f and distance d as acquired from FEM-simulation.

general description of the physics describing radiative linewidths. However, we note that in a split ring the electric and magnetic dipole are *coherently* coupled through the magnetoelectric coupling, and hence may also probe the off-diagonal term in Im$\mathbf{G}$. Moreover, in a split ring the electric and magnetic response have a fixed phase relation, necessarily being a quarter cycle out of phase since the current inducing $\boldsymbol{m}$ and the charge separation inducing $\boldsymbol{p}$ are related by charge conservation. This coherence for instance results in a strongly handed response of split rings under certain viewing angles [17, 31]. We predict that the coherence also affects the strength of interaction between the split ring and its mirror image in the substrate, i.e., the radiative linewidth. In the example we examined in Fig. 3.3, this effect was fortuitously obscured due to the fact that the cross term $\boldsymbol{G}_{EH,xz}$

by symmetry happens to be exactly zero. Microscopically, the radiation emitted by an x-oriented electric dipole in front of a planar surface does not cause any magnetic field along z to be reflected to the split ring to provide back action. If we rotate the split ring to stand with arms up, or point with arms down, cross-coupling becomes important as $\boldsymbol{G}_{EH,xy} \neq 0$. Microscopically, this indicates that an x-oriented electric dipole will receive a y-oriented magnetic field as parts of its reflection in the interface, which in turn will drive the object if it has a y-oriented magnetic polarizability. In Fig. 3.3 we report the radiative linewidth for a point scatterer oriented to exactly represent this case, i.e., that of a split ring that stands up with its legs normal to the plane. The radiative linewidth in this case does not trace a weighted combination of magnetic and electric LDOS. It will depend on $\boldsymbol{G}_{EH,xy}$ instead. Remarkably, this dependence is different for the split ring pointing upwards to the split ring pointing downwards although the object has the *same* electric and magnetic polarizability. A recent paper by Andersen et al. [42] reports a similar effect, but for the radiative rate of self-assembled III-V quantum dots. Depending on the orientation of the trapezoidally shaped dots relative to a plasmonic interface their decay rate is different, although the transition electric dipole moment strength and orientation is invariant. In the quantum dot case, this difference is due to the fact that the highly extended wave functions also introduce an electric quadrupole character to the transition. While quadrupole effects are limited to strong field gradients and hence short distances (< 100 nm) from the interface, for the split rings we expect the orientation asymmetry to persist over longer distances as it is set by dipolar contributions only. As in the experiment reported by Andersen, the key to the asymmetry is that while the electric and magnetic polarizability are invariant upon reversal of the split ring, coherence between the electric and magnetic contributions is important. Indeed, when reversing the split ring orientation, the only difference is the sign of the cross-coupling polarizability, i.e., whether the quarter cycle phase difference between magnetic and electric response is a lag or an advance. Thus the fact that radiation reaction is a coherent effect means that the linewidth provides a direct way to measure phase relations between polarizabilities, and not only absolute values. For instance, one could measure if the quarter wave phase difference between $\boldsymbol{\alpha}_E, \boldsymbol{\alpha}_H$ on the one hand and $\boldsymbol{\alpha}_C$ on the other hand, that is generally surmised from quasistatic ciruit theory for split rings, in fact carries over to real scatterers that are not negligibly small compared to the wavelength and that are not composed of ideal conductors. To our knowledge, this is the first proposition that a new property of the structure that can potentially be engineered independently of the well-known electric LDOS and the recently evidenced magnetic LDOS, may enter radiative linewidth modifications for dipole objects. We

term this a magnetoelectric LDOS effect. Generally, as soon as multiple multipole moments are relevant, not only the separate multipole LDOS's, but also coherences between the different terms will be key to control the overall radiative rates and linewidths for emitters and scatterers.

3.6 Finite element modelling example

Our predictions for the effect of the magnetic and magnetoelectric LDOS on the linewidth of metamaterial scatterers are all subject to the assumption that the scatterers can actually be described in a point dipole picture. An important question that is yet to be tested in experiment and simulations is if this assumption holds at all for metamaterial scatterers, and if so for what classes of optical experiments. Therefore, we perform a numerical experiment and compare the radiative linewidth found from a finite element method calculation with the point dipole predictions. To optimally discriminate for magnetic LDOS effects, we choose an omega-shaped particle that earlier surface integral equation simulations [31, 43] predict to have a very large magnetic and magnetoelectric response. In Ref. [31], the polarizability was quantitatively retrieved by projecting calculated scattered fields for the scatterer held in free space on vector spherical harmonics. We have performed full-field finite element calculations of the omega-shaped scatterer, which is resonant in the microwave regime, again above a high-index substrate ($n = 3.5$). The scatterer geometry is that of a 60 nm thin flat loop of inner radius 0.74 μm and outer radius 1.19 μm radius. Before the loop closes, the arms smoothly curve to be parallel over a length of 390 nm, leaving a gap of 520 nm across. As material we use a Drude model for gold ($\varepsilon(\omega) = \varepsilon_b - \omega_p^2/(\omega(\omega + i\gamma))$ with $\varepsilon_b = 9.54, \omega_p = 2.148 \cdot 10^{15}$ s^{-1} and $\gamma = 0.0092\omega_p$). We employ the commercial COMSOL 3D FEM solver with elements of quadratic order and a grid finesse down to 5 nm. Perfectly matched layers enclose a cylindrical simulation domain (cylinder axis normal to the substrate) that extends 10 μm around the scatterer. We perform a total field-scattered field simulation where, as in the point dipole model, the scatterer is excited by the superposition of a plane wave and its Fresnel reflection. We extract extinct power as the sum of scattered power (obtained from a near-field flux integral over a surface enclosing the particle) and absorbed power, and normalize extinct power to the local driving strength. This procedure was tested on Mie scatterers to give cross sections to better than 1%.

Extinction spectra show a Lorentzian linewidth at all separations, with a varying width and a slightly varying center frequency around a wavelength of 13.5 μm. The center frequency varies because Eq. 3.8 in its most gen-

eral form also contains Re$\boldsymbol{G}$, corresponding to a real frequency shift due to the hybridization of the scatterer with its mirror image. We focus on the linewidth, plotted in Fig. 3.4. Evidently, the linewidth shows oscillations increasing in amplitude when approaching the interface, and is twofold larger close to the interface than away from it. To move beyond this qualitative resemblance with the point dipole prediction, we also plot the linewidth found from point dipole calculations. No adjustable parameters are used for the comparison, as we insert the polarizability values extracted from SIE calculations in Ref. [31], which are characterized through $|\alpha_H/\alpha_E| = 0.3511$ and $|\alpha_C/\alpha_E| = 0.596$. We note that the object has an on-resonance electric polarizability $|\alpha_E| = 3.9\ \mu\text{m}^3$, approximately 30 times the particle volume. The point dipole model is seen to satisfactorily agree with the linewidth in simulations. Thereby, we establish that the point dipole approach not only describes far-field measurements on arrays of split rings, but is also directly applicable for split rings in the near-field of structures that modify LDOS. We propose that the residual deviations contain interesting physics to pursue. Firstly, whether a metamaterial scatterer actually traces the magnetic and magnetoelectric LDOS can be seen as a fundamental test in the discussion in how far a spoof magnetic scatterer is actually a true magnetic scatterer. Secondly, if one accepts that a scatterer that largely radiates according to the magnetic and magnetoelectric LDOS is a bona fide magnetic dipole, one can assess on basis of the residual deviations between simulation and analytical model in how far multipolar corrections are important.

3.7 Conclusion

To conclude we have examined the dependence of the radiative linewith of split ring scatterers on their distance to an interface that modifies the electric LDOS, the magnetic LDOS and a new quantity that we term magnetoelectric LDOS. We propose that this linewidth, i.e., the backaction of the field radiated by the scatterer on itself, can serve as a calibration probe of the complex polarizability tensor and as a fundamental test of the proposed dipolar nature of metamaterial scatterers. Of particular note is the concept of magnetoelectric LDOS, whereby the electric dipole of an object radiates magnetic field that back-acts on the magnetic dipole. It is an interesting question to explore whether such a magnetoelectric LDOS will also affect quantum mechanical transitions. While in the recent breakthroughs by Taminiau et al. and Karaveli et al. magnetic-only transitions in rare earth ions are enhanced [18, 19, 21], it is an open question if transitions with a clear simultaneous electric and magnetic character can be found. Conversely, we propose that coupling single emitters with a purely electric

response to magnetoelectric scatterers may allow to spoof quantum mechanical transitions with a magnetoelectric character, as antennas tend to imbue their polarization characteristics on emitters. Such emitters would likely have interesting chiral properties, since magnetoelectric cross-coupling implies optical activity [44, 45].

3.8 References

[1] L. Landau, E. Lifshitz, and L. Pitaevskii, *Electrodynamics of Continuous Media, 2nd edition*, Elsevier, Amsterdam, 1984.

[2] J. B. Pendry, *Negative refraction makes a perfect lens*, Phys. Rev. Lett. **85**, 3966 (2000).

[3] V. M. Shalaev, *Optical negative-index metamaterials*, Nat. Photon. **1**, 41 (2007).

[4] C. M. Soukoulis and M. Wegener, *Past achievements and future challenges in the development of three-dimensional photonic metamaterials*, Nat. Photon. **5**, 523 (2011).

[5] J. B. Pendry, A. Aubry, D. R. Smith, and S. A. Maier, *Transformation optics and subwavelength control of light*, Science **337**, 549 (2012).

[6] N. Katsarakis, T. Koschny, M. Kafesaki, E. N. Economou, and C. M. Soukoulis, *Electric coupling to the magnetic resonance of split ring resonators*, Appl. Phys. Lett. **84**, 2943 (2004).

[7] J. Garcia-Garcia, F. Martin, J. D. Baena, R. Marques, and L. Jelinek, *On the resonances and polarizabilities of split ring resonators*, J. App. Phys. **98**, 033103 (2005).

[8] C. Rockstuhl, T. Zentgraf, H. Guo, N. Liu, C. Etrich, I. Loa, K. Syassen, J. Kuhl, F. Lederer, and H. Giessen, *Resonances of split-ring resonator metamaterials in the near infrared*, Appl. Phys. B **84**, 219 (2006).

[9] C. Rockstuhl, T. Zentgraf, H. Guo, N. Liu, C. Etrich, I. Loa, K. Syassen, J. Kuhl, F. Lederer, and H. Giessen, *Resonances of split-ring resonator metamaterials in the near infrared*, Appl. Phys. B **84**, 219 (2006).

[10] C. Enkrich, M. Wegener, S. Linden, S. Burger, L. Zschiedrich, F. Schmidt, J. F. Zhou, T. Koschny, and C. M. Soukoulis, *Magnetic metamaterials at telecommunication and visible frequencies*, Phys. Rev. Lett. **95**, 203901 (2005).

[11] M. W. Klein, C. Enkrich, M. Wegener, C. M. Soukoulis, and S. Linden, *Single-slit split-ring resonators at optical frequencies: limits of size scaling*, Opt. Lett. **31**, 1259 (2006).

[12] C. Rockstuhl, T. Zentgraf, E. Pshenay-Severin, J. Petschulat, A. Chipouline, J. Kuhl, T. Pertsch, H. Giessen, and F. Lederer, *The origin of magnetic polarizability in metamaterials at optical frequencies - an electrodynamic approach*, Opt. Express **15**, 8871 (2007).

[13] M. Husnik, M. W. Klein, N. Feth, M. Koenig, J. Niegemann, K. Busch, S. Linden, and M. Wegener, *Absolute extinction cross-section of individual magnetic split-ring resonators*, Nat. Photon. **2**, 614 (2008).

[14] I. Sersic, M. Frimmer, E. Verhagen, and A. F. Koenderink, *Electric and magnetic dipole coupling in near-infrared split-ring metamaterial arrays*, Phys. Rev. Lett. **103**, 213902 (2009).

[15] N. Liu, H. Liu, S. Zhu, and H. Giessen, *Stereometamaterials*, Nat. Photon. **3**, 157 (2009).

[16] C. M. Soukoulis, S. Linden, and M. Wegener, *Negative refractive index at optical wavelengths*, Science **315**, 47 (2007).

[17] I. Sersic, C. Tuambilangana, T. Kampfrath, and A. F. Koenderink, *Magnetoelectric point scattering theory for metamaterial scatterers*, Phys. Rev. B **83**, 245102 (2011).

[18] S. Karaveli and R. Zia, *Strong enhancement of magnetic dipole emission in a multilevel electronic system*, Opt. Lett. **35**, 3318 (2010).

[19] S. Karaveli and R. Zia, *Spectral tuning by selective enhancement of electric and magnetic dipole emission*, Phys. Rev. Lett. **106**, 193004 (2011).

[20] C. M. Dodson and R. Zia, *Magnetic dipole and electric quadrupole transitions in the trivalent lanthanide series: Calculated emission rates and oscillator strengths*, Phys. Rev. B **86**, 125102 (2012).

[21] T. H. Taminiau, S. Karaveli, N. F. van Hulst, and R. Zia, *Quantifying the magnetic nature of light emission*, Nature Comm. **3**, 979 (2012).

[22] L. Novotny and B. Hecht, *Principles of Nano-Optics*, Cambridge University Press, Cambridge, 2006.

[23] F. J. García de Abajo, *Optical excitations in electron microscopy*, Rev. Mod. Phys. **82**, 209 (2010).

[24] R. Sapienza, T. Coenen, J. Renger, M. Kuttge, N. F. van Hulst, and A. Polman, *Deep-subwavelength imaging of the modal dispersion of light*, Nat. Materials **11**, 781 (2012).

[25] B. C. Buchler, T. Kalkbrenner, C. Hettich, and V. Sandoghdar, *Measuring the quantum efficiency of the optical emission of single radiating dipoles using a scanning mirror*, Phys. Rev. Lett. **95**, 063003 (2005).

[26] G. S. Agarwal, *Quantum electrodynamics in the presence of dielectirc and conductors. i. electromagnetic-field response functions and blackbody fluctuations in finite geometries*, Phys. Rev. A **11**, 230 (1975).

[27] K. Joulain, R. Carminati, J.-P. Mulet, and J.-J. Greffet, *Definition and measurement of the local density of electromagnetic states close to an interface*, Phys. Rev. B **68**, 245405 (2003).

[28] K. Joulain, J.-P. Mulet, F. Marquier, R. Carminati, and J.-J. Greffet, *Surface electromagnetic waves thermally excited: Radiative heat transfer, coherence properties and casimir forces revisited in the near field*, Surf. Sci. Rep. **57**, 59 (2005).

[29] I. V. Lindell, A. H. Sihvola, S. A. Tretyakov, and A. J. Viitanen, *Electromagnetic Waves in Chiral and Bi-Isotropic Media*, Artech House, Norwood, MA, 1994.

[30] E. Plum, X. . X. Liu, V. A. Fedotov, Y. Chen, D. P. Tsai, and N. I. Zheludev, *Metamaterials: Optical activity without chirality*, Phys. Rev. Lett. **102**, 113902 (2009).

[31] I. Sersic, M. A. van de Haar, F. Bernal Arango, and A. F. Koenderink, *Ubiquity of optical activity in planar metamaterial scatterers*, Phys. Rev. Lett. **108**, 223903 (2012).

[32] I. Sersic, *Magnetoelectric Resonant Metamaterial Scatterers*, PhD thesis, Universiteit van Amsterdam, 2012.

[33] K. Drexhage, *Influence of a dielectric interface on fluorescence decay time*, J. Lumin. **1 & 2**, 693 (1970).

[34] R. M. Amos and W. L. Barnes, *Modification of the spontaneous emission rate of* Eu^{3+} *ions close to a thin metal mirror*, Phys. Rev. B **55**, 7249 (1997).

[35] E. Snoeks, A. Lagendijk, and A. Polman, *Measuring and modifying the spontaneous emission rate of erbium near an interface*, Phys. Rev. Lett. **74**, 2459 (1995).

[36] M. D. Leistikow, J. Johansen, A. J. Kettelarij, P. Lodahl, and W. L. Vos, *Size-dependent oscillator strength and quantum efficiency of CdSe quantum dots controlled via the local density of states*, Phys. Rev. B **79**, 045301 (2009).

[37] A. Kwadrin and A. F. Koenderink, *Gray-tone lithography implementation of drexhage's method for calibrating radiative and nonradiative decay constants of fluorophores*, J. Phys. Chem. C **116**, 16666 (2012).

[38] M. Paulus, P. Gay-Balmaz, and O. J. F. Martin, *Accurate and efficient computation of the Green's tensor for stratified media*, Phys. Rev. E **62**, 5797 (2000).

[39] P. B. Johnson and R. W. Christy, *Optical constants of the noble metals*, Phys. Rev. B **6**, 4370 (1972).

[40] D. E. Aspnes and A. A. Studna, *Dielectric functions and optical parameters of Si, Ge, GaP, GaAs, GaSb, InP, InAs, and InSb from 1.5 to 6.0 eV*, Phys. Rev. B **27**, 985 (1983).

[41] J. Cui, Y. Huang, and J. Wang, *Near-field radiative heat transfer between chiral metamaterials*, J. Appl. Phys. **112**, 084309 (2012).

[42] M. L. Andersen, S. Stobbe, A. S. Sørensen, and P. Lodahl, *Strongly modified plasmonmatter interaction with mesoscopic quantum emitters*, Nature Phys. **7**, 215 (2011).

[43] A. M. Kern and O. J. F. Martin, *Surface integral formulation for 3d simulations of plasmonic and high permittivity nanostructures*, J. Opt. Soc. Am. A **26**, 732 (2009).

[44] L. D. Barron, *Molecular light scattering and optical activity (2nd edition)*, Cambridge University Press, UK, 2004.

[45] Y. Q. Tang and A. E. Cohen, *Optical chirality and its interaction with matter*, Phys. Rev. Lett. **104**, 163901 (2010).

Chapter 4

Diffractive stacks of metamaterial lattices

Metasurfaces and metamaterials promise arbitrary rerouting of light using 2D planar arrangements of electric and magnetic scatterers, respectively 3D stacks built out of such 2D planes. An important problem is how to self-consistently model the response of these systems in a manner that retains dipole intuition, yet does full justice to the self-consistent multiple scattering via near-field and far-field retarded interactions. We set up such a general model for metamaterial lattices of complex 2D unit cell of poly-atomic basis as well as allowing for stacking in a third dimension. In particular, each scatterer is quantified by a magneto-electric polarizability tensor and Ewald lattice summation deals with all near-field and long-range retarded electric, magnetic and magneto-electric couplings selfconsistently. We show in theory and experiment that grating diffraction orders of dilute split ring lattices with complex unit cell show a background-free signature of magnetic dipole response. For denser lattices experiment and theory show that complex unit cells can reduce the apparent effect of bi-anisotropy, i.e., the strong oblique-incidence handed response that was reported for simple split ring lattices. Finally, the method is applied to calculate transmission of finite stacks of lattices. Thereby our simple methodology allows to trace the emergence of effective material constants when building a 3D metamaterial layer-by-layer, as well as facilitating the design of metasurfaces.

4.1 Introduction

In the field of metamaterials, there is a growing interest in metasurfaces [1, 2]: two-dimensional (2D) arrangements of subwavelength scatterers which combine a strong electric and magnetic response to electromagnetic fields, both of which may contribute equally to scattering [1, 3, 4]. These lattice arrangements offer unprecedented level of control over the reflection, transmission, and refraction of light as seen in state-of-the-art phase mask [5] and phased array antenna designs [6, 7]. While metasurfaces are typically 2D sheets of nonidentical scatterers forming a complex repeated unit cell, metamaterials, in turn, can be conceptually viewed as a 3D stack of 2D lattices of identical meta-atoms [8, 9]. Exactly how the collective response of a metasurface or metamaterial comes about is a function firstly of the scattering properties of individual building blocks, and secondly how a multitude of possibly non-identical building blocks are arranged to cover a surface [10, 11]. Exactly how the magnetic and electric scattering of single building blocks comes about has been a topic of intense discussion, centering mainly on electric dipole models for plasmonics, and LC-circuit models [9, 12, 13, 14, 15] for metamaterial atoms such as split rings. LC-circuit intuition directly implies electric and magnetic dipole-dipole interactions, as well as 'bi-anisotropic' magnetoelectric cross-coupling terms [16, 15, 14]. Given this single building block understanding, an important question currently faced by designers of metasurfaces and metamaterials is how to deal with complex 2D lattices and lattice stacks, while accounting for both electric and magnetic interactions between such building blocks.

In this chapter, we set up an analytical theory based on Ewald lattice summation [17] that can predict the response of diffractive as well as non-diffractive 2D periodic lattices with complex unit cells, as well as stacks of such gratings that form a 3D structure, taking as input the magneto-electric polarization tensors of the magneto-electric scatterers that form the unit cell. In order to test this model, we experimentally verify the optical response of 2D lattices of split rings, since for split rings the single-object polarizability is well known [18, 14, 19, 20]. In particular we examine both dilute and dense lattices of two symmetries, i.e., square lattices in which all SRRs are arranged with their slits pointing in the same direction (A-lattice, Fig. 4.1, left), respecively, in which slit orientations (B-lattice) alternate. This choice is motivated by experimental studies on low-symmetry planar arrays initiated by Decker et al. [21]. The dilute lattices are designed to show grating diffraction orders which we examine for magnetic signatures. In particular we predict and observe additional diffraction orders for the B-lattice as compared to the A-lattice that directly reflect purely magnetic dipole contributions. As a second test we examine the transmission

of dense, i.e., non-diffractive, lattices, in particular focusing on oblique-incidence circularly polarized input and detection. This geometry provides a measure of bi-anisotropy or 'pseudochirality'. We observe cancellation of the bi-anisotropy present in each building for the collective response of the B-lattice. Finally we demonstrate that our calculation methodology has large potential for resolving the fundamental question how effective medium parameters emerge from the stacking of building blocks into 3D slabs, by demonstrating that one can self-consistently calculate reflection and transmission amplitudes that can be used as input for retrieval algorithms. The unique property of our approach is that it is very simple, allows arbitrary magneto-electric response per building block, yet accounts for all the complex self-consistent retarded interactions both in the plane of periodicity, and transverse to the stacked planes, that define the debate on how to deal with spatial dispersion and bi-anisotropy in the resulting effective medium.

This chapter is structured as follows. Sections 4.2 and 4.3 describe the theory. Section 4.4 reports grating diffraction calculations for the two lattice symmetries. Section 4.5 covers the Fourier microscopy setup that was utilized to gather diffraction patterns discussed in section 4.6. Angle-resolved transmission experiments conducted on non-diffractive lattices are described and compared to analytical point dipole (lattice-sum) calculations in section 4.7. In section 4.8, we apply our point dipole model to calculate transmission and reflection for finite stacks of 2D metamaterial layers.

4.2 Starting point: 2D lattice-sum theory

The main point of this chapter is to take the point dipole model reported in Ref. [14], and show how to extend it to arbitrary stacks and supercells of 2D lattices. In a point scattering model [22], the induced electric and magnetic point dipole moments $\boldsymbol{p}$ and $\boldsymbol{m}$ in response to an incident electric and magnetic field $\boldsymbol{E}_{\text{in}}$ and $\boldsymbol{H}_{\text{in}}$ are set by the point scatterer's polarizability $\boldsymbol{\alpha}$ according to

$$\begin{pmatrix} \boldsymbol{p} \\ \boldsymbol{m} \end{pmatrix} = \boldsymbol{\alpha} \begin{pmatrix} \boldsymbol{E}_{\text{in}} \\ \boldsymbol{H}_{\text{in}} \end{pmatrix}. \tag{4.1}$$

For completeness, we briefly recapitulate how one can deal with an arrangement of such scatterers in a simple 2D lattice, defined by lattice vectors $\mathbf{R}_{mn} = m\mathbf{a}_1 + n\mathbf{a}_2$ with integer m and n and real space basis vectors $\mathbf{a}_{1,2}$. The response of a point scatterer at position $\mathbf{R}_{mn}$ is self-consistently set by the incident field, plus the field of all other dipoles in the lattice according

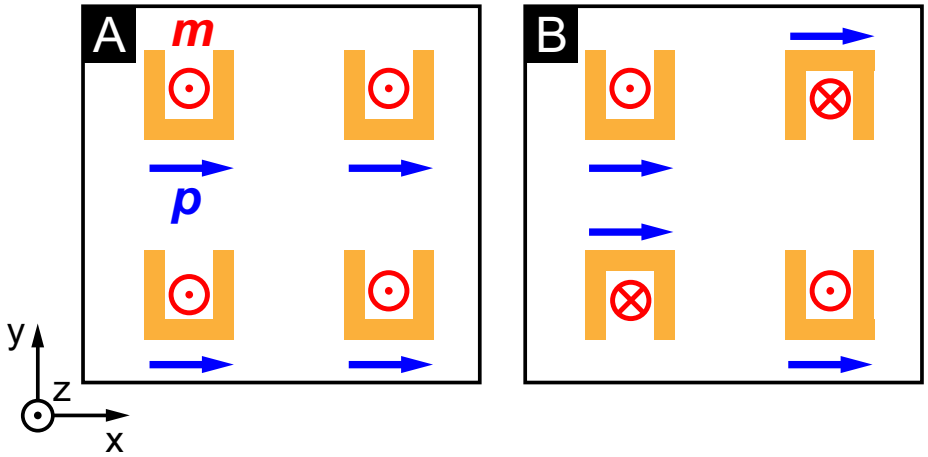

Figure 4.1: Non-primitive unit cell with equal (A) and alternating (B) split ring orientation. An x-polarized electric driving field sets an electric dipole moment $\boldsymbol{p}$ for each individual split ring. Depending on the orientation of the respective split ring, a magnetic dipole moment $\boldsymbol{m}$ will be acquired. The electric dipole orientation will be the same for unit cells A and B, namely in $+x$-direction. However, the magnetic dipoles, while being uniformly $+z$-oriented for unit cell A, will be alternating in $+z$ and $-z$ orientation for unit cell B.

to

$$\begin{pmatrix} \boldsymbol{p}_{mn} \\ \boldsymbol{m}_{mn} \end{pmatrix} = \boldsymbol{\alpha} \left[\begin{pmatrix} \boldsymbol{E}_{\mathrm{in}}(\mathbf{R}_{mn}) \\ \boldsymbol{H}_{\mathrm{in}}(\mathbf{R}_{mn}) \end{pmatrix} + \sum_{m' \neq m, n' \neq n} \mathbf{G}^0(\mathbf{R}_{mn} - \mathbf{R}_{m'n'}) \begin{pmatrix} \boldsymbol{p}_{m'n'} \\ \boldsymbol{m}_{m'n'} \end{pmatrix} \right]. \tag{4.2}$$

If we take a plane wave incident with parallel wave vector $\mathbf{k}_{||}$ and using translation invariance of the lattice, we can substitute a Bloch wave form $(\boldsymbol{p}_{mn}, \boldsymbol{m}_{mn})^T = e^{i\mathbf{k}_{||}\cdot\mathbf{R}_{mn}}(\boldsymbol{p}_{00}, \boldsymbol{m}_{00})^T$ to obtain

$$\begin{pmatrix} \boldsymbol{p}_{00} \\ \boldsymbol{m}_{00} \end{pmatrix} = [\boldsymbol{\alpha}^{-1} - \mathcal{G}^{\neq}(\mathbf{k}_{||}, 0)]^{-1} \begin{pmatrix} \boldsymbol{E}_{\mathrm{in}}(\mathbf{R}_{00}) \\ \boldsymbol{H}_{\mathrm{in}}(\mathbf{R}_{00}) \end{pmatrix} \tag{4.3}$$

Here, $\mathcal{G}^{\neq}(\mathbf{k}_{||}, 0)$ is a summation of the free space 6×6 dyadic Green function $\mathbf{G}^0$ over all positions on the 2D periodic real space lattice barring the origin:

$$\mathcal{G}^{\neq}(\mathbf{k}_{||}, \mathbf{r}) = \sum_{m,n \neq 0} \mathbf{G}^0(\mathbf{R}_{mn} - \mathbf{r}) e^{i\mathbf{k}_{||}\cdot\mathbf{R}_{mn}}. \tag{4.4}$$

We will refer to the summation without exclusion of $m = n = 0$ as $\mathcal{G}(\mathbf{k}_{||}, \mathbf{r})$. The necessary steps for 6×6 dyadic Green functions are easily derived from the known scalar Green function lattice sum. We refer to the Appendix 4.A of this chapter and our recent report on the optical properies of two-dimensional magnetoelectric point scattering lattices [23] for implementation details. As a subtle point we note that throughout this work $\mathbf{R}_{mn}$ represent reciprocal lattice vectors strictly in the $z = 0$ plane, while the 'observation point' $\mathbf{r} = (x, y, z) = (\mathbf{r}_{||}, z)$ at which the lattice sum is evaluated is anywhere in 3D, i.e., at any z. Since each $\mathbf{G}^0(\mathbf{R}_{mn} - \mathbf{r})$ is essentially a spherical wave, the lattice sum contains retardation both in the plane and perpendicular to the plane, even though only a phase factor depending on $\mathbf{k}_{||}$ is explicitly visible in Eq. (4.4).

Once one has obtained the induced dipole moments given the incident field, it is straightforward to calculate the near-field distribution at any point inside, or outside the lattice, i.e., at any $\mathbf{r}$.

$$\begin{pmatrix} \boldsymbol{E}(\mathbf{r}) \\ \boldsymbol{H}(\mathbf{r}) \end{pmatrix} = \begin{pmatrix} \boldsymbol{E}_{\text{in}} \\ \boldsymbol{H}_{\text{in}} \end{pmatrix} e^{i\mathbf{k}\cdot\mathbf{r}} + \mathcal{G}(\mathbf{k}_{||}, \mathbf{r}) \begin{pmatrix} \boldsymbol{p}_{00} \\ \boldsymbol{m}_{00} \end{pmatrix} \tag{4.5}$$

Similarly, one can calculate the intensity and polarization of the diffracted, reflected and transmitted waves. Using the completeness relation of the lattice, one retrieves diffracted orders in the far-field of the form [17]

$$\begin{pmatrix} \boldsymbol{E}(\mathbf{r}) \\ \boldsymbol{H}(\mathbf{r}) \end{pmatrix} = \sum_{\mathbf{g}, |\mathbf{k}^{\mathbf{g}}| \leq k} \begin{pmatrix} \boldsymbol{E}^{\mathbf{g}} \\ \boldsymbol{H}^{\mathbf{g}} \end{pmatrix} e^{i\mathbf{k}^{\mathbf{g}}\cdot\mathbf{r}}, \tag{4.6}$$

where the diffracted wave vectors are

$$\mathbf{k}^{\mathbf{g}} = (\mathbf{k}_{||} + \mathbf{g}, \pm\sqrt{k^2 - |\mathbf{k}_{||} + \mathbf{g}|^2}), \tag{4.7}$$

which can be identified with polar diffraction angles θ, ϕ through $\mathbf{k}^{\mathbf{g}} = k(\cos\phi\sin\theta, \sin\phi\sin\theta, \cos\theta)$. Note that the diffracted orders are simply set by parallel wave vector conservation modulo addition of any vector $\mathbf{g}$ from the reciprocal lattice. The fields associated with each order are

$$\begin{pmatrix} \boldsymbol{E}^{\mathbf{g}} \\ \boldsymbol{H}^{\mathbf{g}} \end{pmatrix} = \frac{2\pi k i}{A\cos\theta} \boldsymbol{M}(\theta, \phi) \begin{pmatrix} \boldsymbol{p}_0 \\ \boldsymbol{m}_0 \end{pmatrix}. \tag{4.8}$$

Here, A is the unit cell area. The orientation matrix $\boldsymbol{M}(\theta, \phi)$ simply contains the radiation pattern of a single dipole. In other words, the radiation pattern from a grating is simply that of the individual dipole, multiplied by a comb of δ-functions at exactly the diffracted grating orders. Mathematically, the orientation matrix $\boldsymbol{M}(\theta, \phi)$ reads

$$\boldsymbol{M} = \begin{pmatrix} D & O \\ -O & D \end{pmatrix} \tag{4.9}$$

where

$$D = \begin{pmatrix} 1-x^2 & -xy & -xz \\ -xy & 1-y^2 & -yz \\ -xz & -yz & 1-z^2 \end{pmatrix} \tag{4.10}$$

and

$$O = \begin{pmatrix} 0 & -z & y \\ z & 0 & -x \\ -y & x & 0 \end{pmatrix} \tag{4.11}$$

using as short hand $x = \cos\phi \sin\theta$, $y = \sin\phi \sin\theta$ and $z = \cos\theta$. Since these are only scattered fields, one still needs to add the incident field to obtain the zero-order transmitted beam.

4.3 Complex base and stacks of 2D layers

Having defined our starting point, we now turn to setting up a theory that can deal with almost arbitrary stacks of 2D lattices. To define the class of problems for which our approach is applicable more clearly, we outline how to deal with an arbitrarily large but finite set of N lattices where each lattice has the same reciprocal lattice vectors, but can have its real space base point arbitrarily shifted both in the plane of periodicity, and transverse to it. Furthermore each lattice can contain a different type of scatterer. Thereby, our theory as outlined in this section can directly deal with a rich variety of problems. These include the physics of planar structures with complicated supercells of many different scatterers, such as metasurfaces, or stacks of metamaterial planes that form a 3D structure.

Suppose we have $m = 1 \ldots N$ lattices of the same symmetry, each shifted by an arbitrary spatial offset $\mathbf{r}^m_{0,0}$ sideways, and z^m perpendicular to the plane, and potentially each containing a different type of scatterer of polarizability $\boldsymbol{\alpha}_m$. As an example, lattice type B (Fig. 4.1, right) can be represented by two lattices (one for each split ring orientation) with relative offset of $\sqrt{2}/2$ in the (x, y)-plane. Since under our assumption Bloch's theorem still holds, the problem of N infinite periodic lattices reduces to finding just the N dipole moments on the central lattice sites in each lattice, i.e., the sites $(\mathbf{r}^m_0, z^m)$. Indeed, Bloch's theorem asserts that at any other lattice site in the same layer m, the moment is simply $\boldsymbol{p}^m(\mathbf{r}^m_0 + \mathbf{R}, z^m) = e^{i\mathbf{k}_{||}\cdot\mathbf{R}}\boldsymbol{p}^m(\mathbf{r}^m_0, z^m)$. The N independent dipole moments are once again set by a self-consistent equation. For the dipole moment at $(\mathbf{r}^m_0, z^m)$ in layer m, the self-consistent

equation reads

$$\begin{pmatrix} \boldsymbol{p}^m \\ \boldsymbol{m}^m \end{pmatrix} = \boldsymbol{\alpha}_m \left[\begin{pmatrix} \boldsymbol{E}_{\text{in}} \\ \boldsymbol{H}_{\text{in}} \end{pmatrix} e^{i\mathbf{k}\cdot(\mathbf{r}_0^m, z^m)} + \mathcal{G}^{\neq}(\mathbf{k}_{||}, 0) \begin{pmatrix} \boldsymbol{p}^m \\ \boldsymbol{m}^m \end{pmatrix} + \sum_{m'=1, m' \neq m}^{N} \mathcal{G}(\mathbf{k}_{||}, (\mathbf{r}_0^{m'} - \mathbf{r}_0^m, z_{m'} - z_m)) \begin{pmatrix} \boldsymbol{p}^{m'} \\ \boldsymbol{m}^{m'} \end{pmatrix} \right]. \tag{4.12}$$

Here, the interpretation is that any dipole is driven by the external incident field (first term on the right hand side), by all the dipoles except itself in the *same* layer (second term on the right hand side that also occurs in Eq. (4.2)), and moreover by all the dipoles in all the *other* layers. In this third term a full lattice summation, *including* the $(0, 0)$ term, occurs. It should be noted that in the first term, i.e., the direct driving, the retardation of the driving across the structure is directly explicit both transverse to the plane, and in the plane, as the term $\mathbf{k} \cdot (\mathbf{r}_0^m, z)$ explicitly contains the full 3D wave vector and 3D lattice base point coordinate. What is less obvious upon inspection is that the third term, i.e., $\mathcal{G}(\mathbf{k}_{||}, (\mathbf{r}_0^{m'} - \mathbf{r}_0^m, z_{m'} - z_m))$ also accounts both for retardation in plane (evident through the explicit argument $\mathbf{k}_{||}$) and out of the plane, i.e., for phase increments across the distances $z_{m'} - z_m$ between planes. Note from the definition Eq. (4.4) that this retardation is in fact accounted for in the lattice sum not through the explicit Bloch phase term $e^{i\mathbf{k}_{||}\cdot\mathbf{R}_{mn}}$ but through the fact that one coherently sums *spherical* waves $\mathbf{G}^0$ at given overall k. In the actual implementation of the lattice sum (see Appendix), the retardation transverse to each plane appears explicitly (cf. Eq. (4.18) in particular) as the different real and evanescent diffracted orders $\mathbf{k}^g$ that couple lattices each involve different phase slips $k_z^{\mathbf{g}}|z_{m'} - z_m|$ with transverse wave vector $k_z^{\mathbf{g}} = \sqrt{k^2 - |\mathbf{k}_{||} + \mathbf{g}|^2}$.

Returning to the overall solution strategy, we note that the summation in the new, third term of Eq. (4.12) is no more difficult to deal with than the original lattice sum in Eq. (4.3) and Eq. (4.4). In terms of its overall structure, Eq.(4.12) is almost identical to a usual multiple scattering problem for just N scatterers, and is a simple set of $6N$ linear equations for $6N$ unknowns once one has calculated the required lattice summations that couple the lattices. However, while usually the coupling matrix would simply have $\boldsymbol{\alpha}_m^{-1}$ on the diagonal, now the block diagonal reads $\boldsymbol{\alpha}_m^{-1} - \mathcal{G}^{\neq}(\mathbf{k}_{||}, 0)$. In other words, the polarizability of each scatterer is renormalized by the lattice sum of the layer in which it is embedded. The off-diagonal terms for a standard multiple scattering problem would simply be the Green function $\mathbf{G}(\mathbf{r}_m, \mathbf{r}_{m'})$ that quantifies the dipole field at $\mathbf{r}_m$ due to a dipole at $\mathbf{r}_{m'}$. Here, the off diagonal terms are given by the lattice-summed Green func-

tion $\mathcal{G}(\mathbf{k}_{||}, \mathbf{r}_0^{m'} - \mathbf{r}_0^m, z_{m'} - z_m)$ that quantifies the field strength exerted by lattice m' on lattice m.

Once the dipole moments in each layer are retrieved, one can once again find the far-field intensity in each diffracted order, taking into account the fact that different layers are shifted to have the base point away from the origin, giving rise to a phase shift. The fields associated with each order are

$$\begin{pmatrix} \boldsymbol{E}^{\mathbf{g}} \\ \boldsymbol{H}^{\mathbf{g}} \end{pmatrix} = \frac{2\pi k i}{A\cos\theta} \boldsymbol{M}(\theta,\phi) \sum_{m=1}^{N} \begin{pmatrix} \boldsymbol{p}^m \\ \boldsymbol{m}^m \end{pmatrix} e^{-i\mathbf{k}^{\mathbf{g}}\cdot(\mathbf{r}_0^m, z^m)}. \tag{4.13}$$

While exactly the same diffracted orders appear as for a single lattice, their amplitude is now a coherent summation of the diffracted fields from each layer separately. The coherence involves both the phase in $(\boldsymbol{p}_m, \boldsymbol{m}_m)$ that arises from the selfconsistent interactions, and an additional phase slip owing to the displacement $(\mathbf{r}_0^m, z^m)$.

4.4 Diffractive calculation

Our calculation method can be applied to 2D lattices that have more than one scatterer per unit cell (complex basis for the lattice) [11, 10, 1], as well as stacks of such 2D lattices that form a 3D structure. In this section we show calculations for 2D lattices with more than one scatterer per unit cell. As a first demonstration, we have calculated grating diffraction efficiencies of comparatively dilute split ring lattices for two types of lattices. Lattice A is a simple square lattice (periodicity 1500 nm) while lattice B has every second split ring rotated by 180 degrees in checkerboard geometry [10]. These two lattices have identical number of scatterers per unit area, but have differently sized unit cells. In particular, the B lattice has a larger unit cell, thereby giving rise to extra allowed diffraction orders. These orders have nonzero amplitude only when the scatterers have an induced magnetic dipole, and can hence be viewed as direct and background-free quantification of the magnetic SRR response. As split ring polarizability we include radiation damping according to

$$\boldsymbol{\alpha}^{-1} = \boldsymbol{\alpha}_{LC}^{-1} - i\frac{2}{3}k^3\mathbb{I}, \tag{4.14}$$

in the static LC-circuit polarizability

$$\boldsymbol{\alpha}_{LC} = \frac{\omega_0^2 V}{\omega_0^2 - \omega^2 - i\omega\gamma} \begin{pmatrix} \eta_E & 0 & \dots & 0 & i\eta_C \\ 0 & & & & 0 \\ \vdots & & \ddots & & \vdots \\ 0 & & & & 0 \\ -i\eta_C & 0 & \dots & 0 & \eta_H \end{pmatrix} \tag{4.15}$$

exactly as argued in Ref. [14]. This formulation ensures a scattering theory that satisfies reciprocity and the optical theorem in limit of no Ohmic damping, while γ introduces absorption loss. We assume the LC resonance to be described by a resonance frequency $\omega_0 = 1.26 \times 10^{15}$ s^{-1} (corresponding free space wavelength $\lambda = 1500$ nm), damping rate γ equal to the Ohmic damping rate of gold ($\gamma = 1.25 \times 10^{14}$ s^{-1}) and parameters $\{\eta_E, \eta_H, \eta_C\} = \{0.7, 0.3, 0.4\}$, where V is the split ring volume ($150 \times 150 \times 30$ nm^3). As environment we assume a homogeneous medium of index $n = 1.0$. Figure 4.2 reports the calculated zero order transmission coefficient, and the efficiencies for transmitted grating orders, assuming normal incidence, and plotting only the intensity co-polarized with the incident beam. A polarization analysis will be presented below in the framework of our experiments. The zero-order transmission shows a broad minimum punctuated by a narrow grating anomaly around 6700 cm^{-1} (wavelength equal to the grating pitch). The transmission depth is around 20%, commensurate with the very dilute nature of the grating and the per split-ring cross section [18] of around 0.3 μm^2. The grating anomaly is coincident with the emergence of the first order grating diffraction at grazing exit angle. The first order grating diffractions reach efficiency values of around 0.5 to 1% at $\lambda^{-1} = 7100$ cm^{-1}. For a simple lattice of electric dipoles polarized along the x-axis, one would expect the highest grating efficiency to occur for the $(0, \pm 1)$ order, owing to the fact that the single dipole emission pattern is peaked away from the dipole orientation. For instance, for a frequency of $\lambda^{-1} = 7100$ cm^{-1}, the grating orders appear at circa 80° from the plane normal. For this angle, the expected intensity ratio assuming purely electric dipole scatterer is $\sin^2\theta : \cos^2\theta = 8 : 1$ for the $(0, \pm 1)$ orders compared to the $(\pm 1, 0)$ orders. Reference [24] verifies that this reasoning to estimate grating diffraction efficiency from single-dipole radiation patterns indeed quantitatively holds for dilute lattices of plasmonic rod dipole antennas. The fact that in experiments the actual ratio for the split ring lattice is closer to 2 : 1 than the estimated 8 : 1 is a direct consequence of the magnetic dipole radiation.

Next we turn to the superlattice. If the base lattice A has reciprocal lattice vectors $b_1 = 2\pi/d(1, 0)$ and $b_2 = 2\pi/d(0, 1)$, the superlattice can be classified as having a two-atomic basis with reciprocal lattice vectors $b_1 = 2\pi/d(1/2, 1/2)$ and $b_2 = 2\pi/d(1/2, -1/2)$. Consequently, a set of extra diffraction orders appears. We label the extra orders with half integer number pairs obtained by normalizing the $\mathbf{G}$-vector added to $\mathbf{k}_{||}$ in the diffraction process to $2\pi/d$. It should be noted that the extra orders will not correspond to *all* combinations of half integers. Indeed, the first set is at $(\pm 1/2, \pm 1/2)$ (and not at $(\pm 1/2, 0)$ resp. $(0, \pm 1/2)$). The calculated diffraction efficiencies contain two independent measures of the magnetic dipole component of SRR scattering. Firstly, the amplitude in the half-

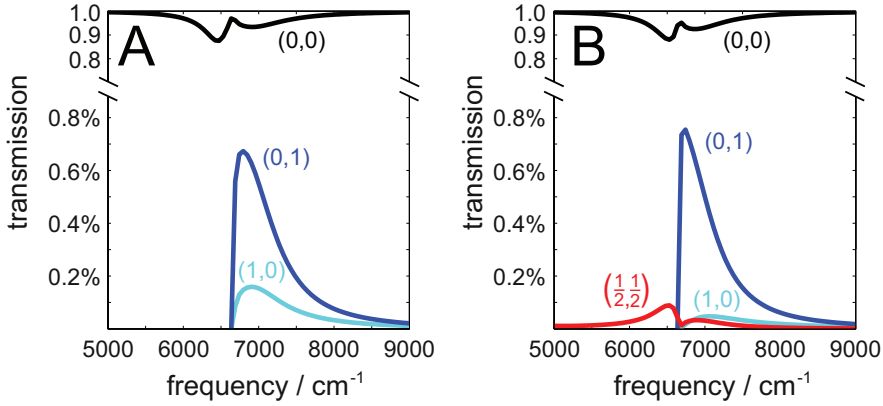

Figure 4.2: Calculated transmission for diffracted orders for SRR lattices of type A (left) and B (right) assuming a lattice of 1500 nm pitch, in an environment of $n = 1$. As SRR parameters we use $\omega_0 = 1.26 \times 10^{15}$ s^{-1}, $\gamma = 1.25 \times 10^{14}$ s^{-1}, $\{\eta_E, \eta_H, \eta_C\} = \{0.7, 0.3, 0.4\}$. Note the emergence of half-integer diffraction orders for lattice type B with their cut-off being outside of the presented frequency range.

integer orders can be viewed as direct and background-free quantification of the magnetic SRR response, since they would not appear for $\eta_H = \eta_C = 0$. As Figure 4.2 shows, the half integer orders appear from frequencies $1/\sqrt{2} \times 6700$ cm^{-1} onwards, and indeed contain significant amplitude (up to 2.5% total diffraction efficiency spread over four beams). A second measure of the magnetic dipole strength is evident in the $(\pm 1, 0)$ and $(0, \pm 1)$ orders. As soon as the condition for emergence of the $(\pm 1, 0)$ and $(0, \pm 1)$ is crossed, the $(\pm 1/2, \pm 1/2)$ orders diminish in amplitude. Remarkably, the contrast between the $(0, \pm 1)$ and $(\pm 1, 0)$ orders is much stronger than in the A lattice, reaching up to 10:1 rather than 2:1. This larger ratio is a direct consequence of the fact that, in the superlattice, the magnetic dipoles are aligned in antiphase in the two sublattices, while the electric dipoles are aligned. Since the $(\pm 1, 0)$ intensity for the A lattice is mainly from the z-oriented magnetic dipoles, the diminished $(1, 0)$-diffraction strength is due to cancellation of the magnetic dipole contributions in the antiparallel arrangement [10].

4.5 Fourier microscopy setup

In order to verify the predictions for diffraction by the A and B lattices, we perform a diffraction experiment in the near infrared on Au split ring

resonator arrays fabricated using e-beam lithography and lift-off [25]. The dimensions are 150 nm×150 nm×30 nm with gaps of 50 nm×80 nm. The setup (sketch shown in Fig. 4.3) is essentially built as an infrared-range copy of the setup reported in Ref.[24] with achromatic lenses specified for 1050 nm−1620 nm. Light from a supercontinuum source (Fianium) is frequency selected by passing through an acousto-optical tunable filter (Crystal Technology PCAOM NIR 2) that allows to select any wavelength from 1100 nm to 2000 nm, with a spectral selection FWHM-bandwidth of around 12 nm at 1550 nm. After passing a linear polarizer (Thorlabs LPNIR100) the beam is weakly focused to a spot of ≈ 20 µm diameter, smaller than an individual lattice which covers an area of 50 µm×50 µm. This illumination approximates a plane wave as it has an angular spread $\Delta k_{||}/k = 0.02$. Light passing through the sample is collected by a 100× oil objective (Olympus UPLSAPO, NA = 1.4). To retrieve k-space information, we image the back aperture of the objective onto an InGaAs CCD (Vosskühler NIR 300-PGE) via a $4f$-imaging system ($f_{\text{telescope}} = 50\,\text{mm}$, $f_{\text{Fourier}} = f_{\text{tube}} = 200\,\text{mm}$). An iris placed in the real space image plane in between the 1 : 1 telescope lens pair blocks light stemming from the edges of an illuminated lattice which would cause additional features in the k-space image. Our aim is to study the intensity and polarization for non-zero diffracted orders. However, the sparse arrangement of scatterers will result in back focal plane images that are dominated by the 0-order transmitted beam. Indeed, the calculations in Fig. 4.2 indicate an intensity ratio on the order of 10^3:1, making acquisition of diffraction orders well above the noise, without oversaturation of the zeroth order problematic on a CCD limited dynamic range of 12 bit. We overcome this limitation by placing a 0-order beam block at the back aperture of the objective. The beam block is a metal sheet disc of 2.5 mm diameter supported by a cross of thin wires (200 µm width), made by electrical discharge machining in a 200 µm thick metal foil. The size of the disk should be compared to the backaperture size of our Olympus UPLSAPO 100× objective which is 7.1 mm in diameter. For cross-polarized excitation/analysis configurations the beam block may be omitted.

4.6 Diffraction measurement

First, we compare the diffraction patterns of the lattice of type A to the B-lattice (sketch in Fig.4.4) under plane-wave illumination at 1550 nm. We use lattices immersed in index matching oil to obtain a completely symmetric optical environment, and use a pitch of 1250 nm. The measurements are hence done well to the blue of the diffraction condition. Data in the co-polarized channel, i.e., with input polarization and detection polarization

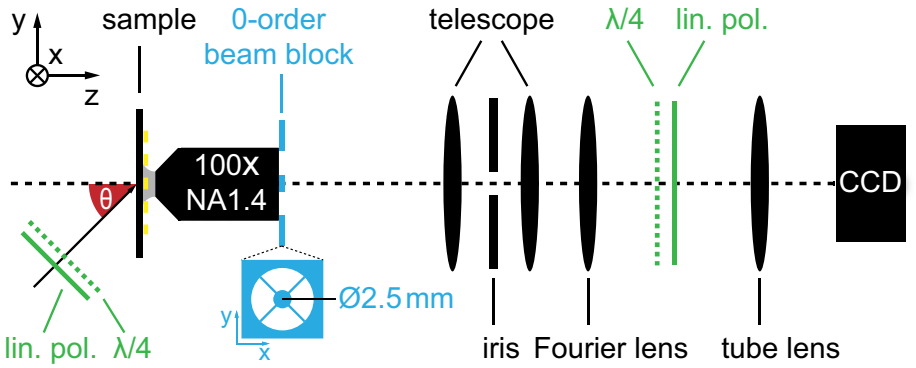

Figure 4.3: In our Fourier microscopy setup, light from a filtered supercontinuum light source is incident from the left at an angle θ from the lattice plane normal. A 100× immersion objective collects transmitted light. The iris provides real space filtering prior to Fourier imaging.

along the split ring base x, clearly evidence the $(\pm 1, 0)$ and $(0, \pm 1)$ diffraction orders. The efficiency in these four orders stand in almost 1:1 ratio, in apparent contradiction to Fig. 4.4. However, it should be noted that at the wavelength used, the grating diffraction angle of about 55° is much closer to the sample normal than in the calculation example. Consequently, the expected intensity ratio on basis of electric dipoles alone is around 2:1 further reduced by magnetic contributions. The magnetic contribution to diffraction should appear much more clearly in cross-polarized detection, since the electric dipole should be x-polarized for all orders, while the magnetic dipole should give rise to y-polarized light for the orders on the k_x axis (and vice versa). Indeed, in cross-polarized detection the $(0, \pm 1)$ orders almost vanish compared to the orders on the x-axis $(\pm 1, 0)$ diffraction orders, yielding a 7:1 ratio.

For the B-lattice, the diffraction-pattern in co-polarized excitation and detection is dominated by the $(\pm 1, 0)$ and $(0, \pm 1)$ orders, as in the A-lattice. This similarity, which is much stronger than expected from Fig. 4.2 is indicative of the fact that actual split rings do not have equally electric, magnetic, and magneto-electric polarizability, but in fact are expected [19] to have $\alpha_E : \alpha_H : \alpha_C = 4 : 1 : 2$. Nonetheless, the extra half-integer orders are faintly visible in the co-polarized Fourier image. The magnetic nature of the SRR scatterers is much more clearly evident in the cross-polarized Fourier image. In cross-polarization, all the integer orders almost vanish. For the $(0, \pm 1)$ orders such vanishing is expected since both the electric and magnetic dipole contributions are $x-$polarized for wavevectors in the

yz-plane. For the $(\pm 1, 0)$ orders, all y-polarized light must result from the magnetic dipole radiation. However, in strong contrast to the A-lattice, where the magnetic dipoles are all aligned and give a clear $(1, 0)$-diffraction, in the B-lattice cancellation occurs owing to the fact that the two distinct sublattices have magnetic moments in antiphase. Remarkably, in the cross-polarized data the half-integer diffraction orders clearly stand out at the $(\pm 1/2, \pm 1/2)$ nodes, providing a background free measure for the presence of magnetic polarizability in the single SRR polarizability. Strictly no intensity is expected at the $(\pm 1/2, 0)$ and $(0, \pm 1/2)$ nodes if the split rings could be considered points located exactly on a square lattice. Careful inspection points at a very faint diffraction intensity at these angles, which we attribute to a minute deviation in split ring positioning introduced by the RAITH-lithography pattern generator.

Next we turn to a more comprehensive polarization analysis of the half-integer orders. We study a lattice of higher split ring density (pitch 900 nm), so that the diffraction orders move outwards in the Fourier image. In fact, at this pitch, the condition for integer order diffraction $(\pm 1, 0)$ are not yet met, while the half-integer orders occur at large NA, conveniently far from the zero-order transmitted beam. According to point scattering theory, if the split rings would have no magnetic polarizability, and no bi-anisotropy, they would all carry identical electric dipole moment, no magnetic moment, and the half-integer orders would have strictly zero intensity. From symmetry it is apparent that even in presence of bi-anisotropy and split ring coupling, at normal incidence the induced electric dipole moments in each sublattice will still be equal. Consequently, the half-integer diffraction orders are solely due to the induced magnetic dipoles. Since in high-NA Fourier imaging of an out-of-plane magnetic dipole, the back focal plane image must contain a radially polarized magnetic field, polarization analysis of the Fourier image must reveal azimuthal polarization. Figure 4.5 shows Fourier images with excitation polarization along the split ring base x, and the detection polarizer set at 0°, 90° and ±45° relative to the x-axis. The four orders indeed are dominantly azimuthally polarized, commensurate with radiation of out-of-plane magnetic dipole moments.

4.7 Angle-resolved transmission and pseudochirality

Recent reports indicate that dense split ring lattices that have square symmetry and all split rings aligned show a strongly handed response when illuminated under an angle. This handed response was first noted for split ring lattices by Plum et al. [26, 27, 28], who proved that an asymmetric

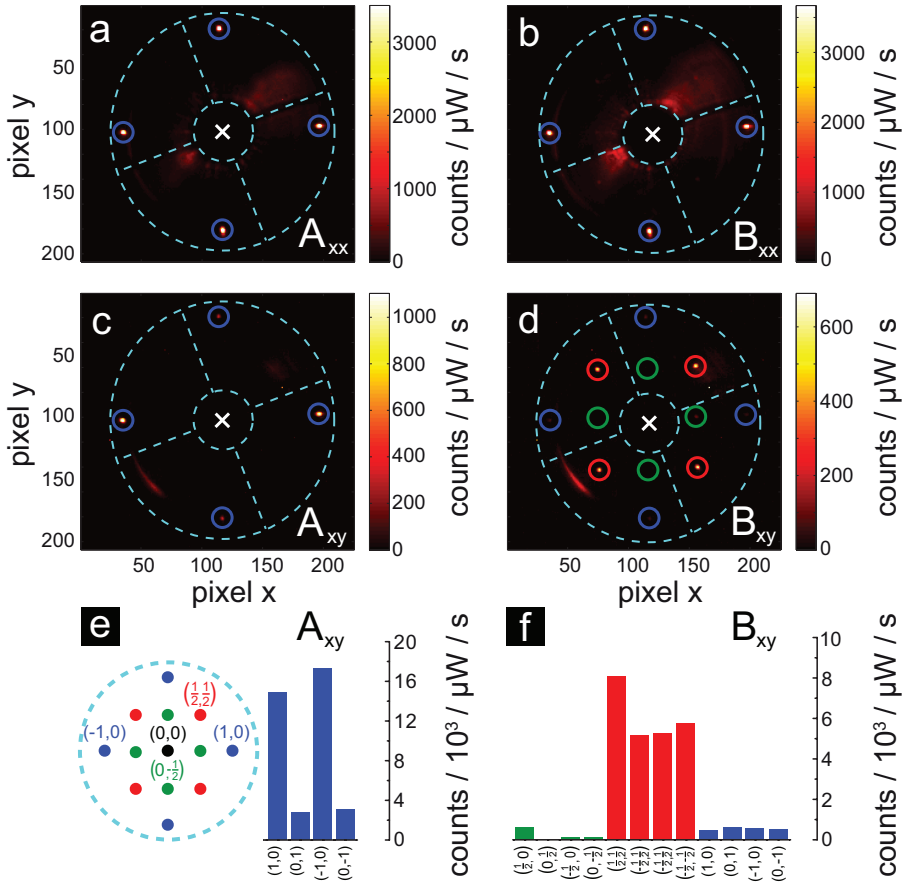

Figure 4.4: Diffraction pattern analysis for lattice type A (a,c) and lattice type B (b,d) for plane wave illumination with x-polarized light at 1550 nm. For cross-polarized analyzer orientation (y-direction) the diffraction patterns for A and B (c,d) are clearly distinct. For A, diffracted light is found in orders (blue) close to the maximum collection angle of the system (dashed circle). In contrast, lattice B also shows half integer orders (red). Cross-polarized detection brings out these orders more clearly. Histograms (e,f) quantify the cross-polarized intensity. Low diffraction order intensities at positions indicated in green are attributed to minute deviations of SRR center positions from a perfect square lattice introduced during the manufacturing process.

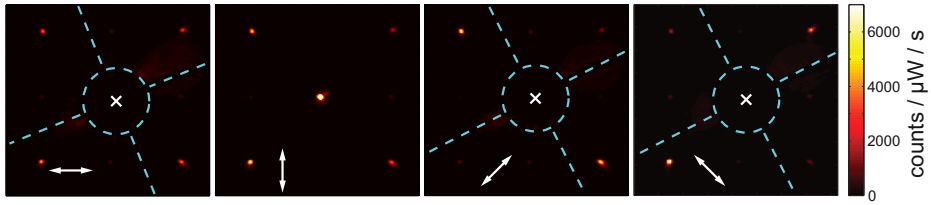

Figure 4.5: Experimental polarization analysis for lattice type B. For a lattice pitch of 900 nm pitch, only the orders are propagating. Fourier images for different analyzing polarizer settings (white arrow) reveal that the orders are azimuthally polarized.

response is allowed under oblique incidence even for geometrically nonchiral structure. The key to their argument is that the illumination geometry should be included in the symmetry considerations. A different interpretation is that the handed response is intrinsic to the single split ring polarizability tensor and directly results from the off-diagonal bi-anisotropy. This form of 'pseudochirality' was already discussed in 1997 by Tretyakov [29] in the framework of current carrying cut wires, omega particles and helices. Recently, this pseudochirality was measured to be exceptionally strong in split rings by Sersic et al. [19]. A shortcoming of that work was that, while the asymmetric response was attributed to the single building block, in fact the observation was made on lattices without mapping the influence of the lattice symmetry. Here, we present calculations as well as experiments on superlattices of different symmetry, i.e., the A-lattice with all split rings aligned, and the B-lattice in which bi-anisotropy should cancel in the zero-order transmission.

Figure 4.6 (left) shows calculations for the A lattice, assuming split rings in a square lattice of pitch 300 nm, in surroundings index-matched to glass ($n = 1.5$). As parameters we take $\{\eta_E, \eta_H, \eta_C\} = \{0.7, 0.3, 0.4\}$, $\gamma = 1.25 \times 10^{14}\,\mathrm{s}^{-1}$, and $\omega = 1.108 \times 10^{15}\,\mathrm{s}^{-1}$ in order to match the resonance wavelength to the wavelength with lowest normal incidence transmission dip. As also reported by Sersic et al. [19] and Lunnemann et al. [23] lattice A shows a strongly asymmetric handed response when rotating the sample in the incident beam around the split ring symmetry axis and collecting the total transmitted signal without analyzer. The asymmetry consists of a sharp decrease in transmission when going from normal incidence to positive angles at handed incidence light, and almost vanishing of the transmission resonance when either rotating the sample in the opposite direction, or collecting in the opposite helicity channel. For rotation around the x-axis, the asymmetry vanishes entirely. Here we have measured and calculated trans-

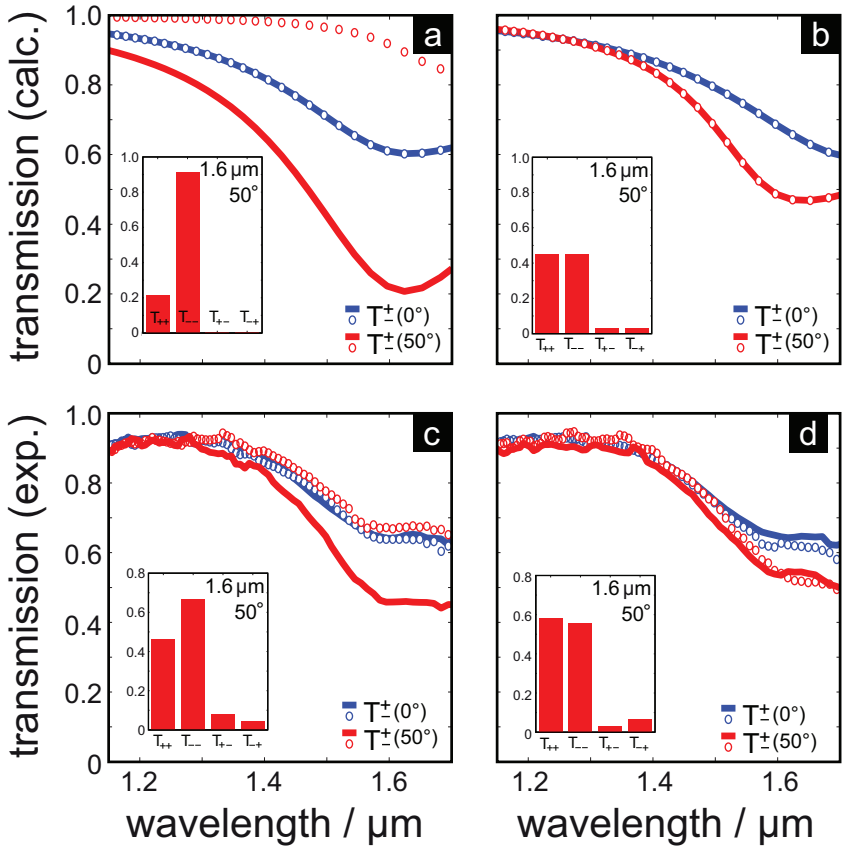

Figure 4.6: Calculated and experimentally retrieved transmission spectra for SRR lattices of type A (a, c) and B (b,d) with lattice pitch 300 nm. Right- (+) and left-handed (−) circularly polarized light is incident at 0° (blue) and 50° (red) from the lattice normal. The insets depict histograms for transmission at 1600 nm and 50° angle of incidence. The contrast in co-polarized transmission channels T_{++} and T_{--} for lattice type A (insets a,c) vanishes for lattice type B (insets b,d). Transmission for cross-polarized polarization channels T_{+-} and T_{-+} is considerably smaller for both lattice types compared to the co-polarized case.

mission for both the helicity conserving ($T_{\pm\pm}(\theta)$ channels, and the helicity nonconserving channels ($T_{\pm\mp}(\theta)$). Calculations of transmission resolved for the output polarization shows that the handed transmission contrast is not associated with polarization conversion. Indeed, our calculation predicts a large contrast between T_{++} and T_{--}, but no amplitude in the helicity non-conserving channel ($T_{+-} = 0$ and $T_{-+} = 0$).

Our transmission measurement is effectuated in the same set up also used for diffraction experiments. The detection path again uses a $N = 1.4$ oil immersion objective and InGaAs CCD detector. Oblique illumination is provided by fiber coupling the spectrally filtered supercontinuum light and mounting the output fiber coupler, collimation and focusing optics, as well as polarization optics on a manually adjustable goniometer arm. We can select the transmitted beam from just the patterned sample area using real space and Fourier space filtering in the detection path. A reference for the transmission measurement is obtained by shifting the sample to image an unpatterned region.

Measurements of transmission for two handednesses for an index matched lattice with 300 nm pitch of split rings (150 nm arm lengths, gap size of 50 nm by 80 nm, 30 nm height) indeed show strong asymmetry in oblique incidence transmission for the A lattice. Compared to the previous report by Sersic et al. [19], the measured transmission asymmetry is clearly evident, yet less pronounced, which we attribute to the fact that in that measurement the substrate was not index matched. Presence of a dielectric substrate can significantly affect the magnetic polarizability and increase bi-anisotropy as was reported for split rings on substrates [30] as well as fishnet metamaterials [31]. Polarization analysis of the transmitted light on resonance $\lambda_0 = 1600\,\text{nm}$ quantifies that the transmitted light does not show strong polarization conversion.

Figure 4.6 (top and bottom right) show transmission calculations and measured data for the B lattice. The handed-dependent difference in angle-dependent transmission vanishes entirely, showing that in this particular type of structure it is the single building block that determines the asymmetric response, as opposed to spatial dispersion that was recently proposed to mimic chirality [32]. A viable solution to reduce the apparent bi-anisotropy in metamaterials is hence to create superlattices with rotated copies of the same bi-anisotropic building block. However, the price is that the increased unit cell size causes diffractive effects already at lower frequencies.

4.8 Stacked lattices

Finally, we discuss application of our multi-stack point scattering theory to a problem of large interest in metamaterials research, i.e., the emergence of properties such as transmission, ϵ and μ, as a function of the number of lattices that one stacks to obtain a truly 3D structure. A second context in which stacking is relevant is in the formation of stereometamaterials, in which identical lattices are stacked with split rings rotated from layer to layer, and in which retardation between layers may also occur[15]. We refer to Ref. [33] for a treatment of this model in electrostatic circuit theory amended to include a retardation phase. We suppose one could stack layers of split rings resonant at 1.5 µm that are in 2D square lattices of 300 nm pitch with a spacing between layers of 300 nm, so that a finite crystal of simple cubic symmetry is formed. As parameters we use $\eta_E = \eta_H = \eta_C = 1$, $\gamma = 8.3 \times 10^{13}\,\mathrm{s}^{-1}$, $\omega = 1.256 \times 10^{15}\,\mathrm{s}^{-1}$, which emulates the case of maximally magneto-electric cross-coupled SRRs, with a damping rate comparable to silver. Stacked fabrication of split ring lattices was reported by Liu et al. [15]. Figure 4.7(left) shows the calculated transmission coefficient as a function of the number of layers. As one expects from reported data, a single layer already presents a significant suppression of transmission to below 15%, owing to the large cross section per split ring. The reflection coefficient of around 45% (right panel in Figure 4.7), shows a peak complementary to the transmission, leaving a significant residual 40% absorption. As the number of layers is increased, the transmission stop gap significantly deepens and widens, as would be expected for an increasingly thick slab with a strong absorption resonance. At the same time, the reflection resonance reduces in strength, stays comparable in width to the single layer reflection peak, and gains a significant number of fringes with increasing structure thickness. Since the multi-stack point scattering theory returns full amplitude and phase information for reflection and transmission, one could continue to pursue a number of interesting studies on the convergence of ϵ and μ as retrieved from the reflection and transmission, as a function of thickness, density, and single dipole polarizability. Moreover, one could explore how multiple scattering interactions become apparent as spatial dispersion in the retrieved material constants.

4.9 Conclusion

In this work, we successfully described experimentally retrieved grating order intensities and transmission spectra for diffractive and non-diffractive SRR lattices with a magnetoelectric point dipole model extended for stacks

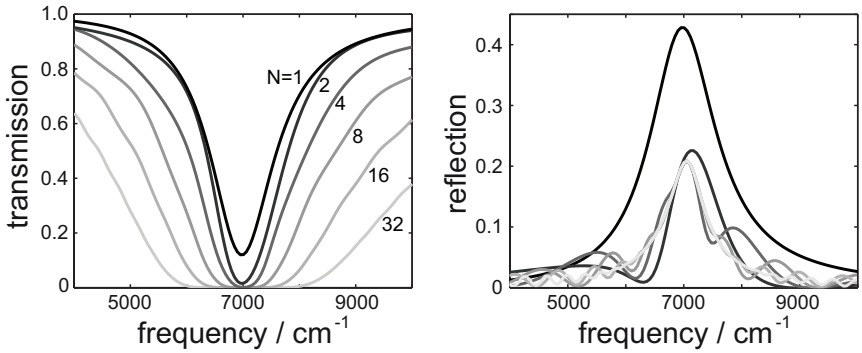

Figure 4.7: Calculated transmission and reflection for N stacked layers of lattice type A so that the SRRs ($\eta_E = \eta_H = \eta_C = 1$, $\gamma = 8.3 \times 10^{13}\,\mathrm{s}^{-1}$, $\omega = 1.256 \times 10^{15}\,\mathrm{s}^{-1}$) are in a simple cubic arrangement with a lattice constant of 300 nm.

of 2D lattices applying Ewald's summation technique. The role of magnetic dipole response for SRR lattices was revealed by comparing diffraction order intensities of a lattice formed by a trivial unit cell (single-atomic base) to a lattice formed by a complex unit cell (two-atomic base) with alternating SRR orientation. The alternating SRR orientation in the complex unit cell case lead to the absence of transmission contrast for right- and left-handed incident light for off-normal illumination as predicted by our model. Finally, we explored the influence of the finite number of 2D metamaterial layers forming a 3D stack on the stack's total transmission and reflection.

4.A Lattice sum

The 6×6 dyadic Green function of free space can be obtained by applying the operator

$$\begin{pmatrix} \mathbb{I}k^2 + \nabla \otimes \nabla & -ik\nabla\times \\ ik\nabla\times & \mathbb{I}k^2 + \nabla \otimes \nabla \end{pmatrix} \tag{4.16}$$

to the Green function of the scalar wave equation. Hence also the 6×6 dyadic lattice sum follows from the lattice sum for the scalar Green function, i.e., from

$$\sum_{m,n} \frac{e^{ik|\mathbf{R}_{mn}-\mathbf{r}|}}{|\mathbf{R}_{mn}-\mathbf{r}|} e^{i\mathbf{k}_{||}\cdot\mathbf{R}_{mn}} = \Gamma^{(1)} + \Gamma^{(2)}. \tag{4.17}$$

Note that in this defintion, $\mathbf{R}_{mn}$ are real space lattice vectors strictly in the x, y plane, while the observation point $\mathbf{r} = (x, y, z) = (\mathbf{r}_{||}, z)$ may be outside

the lattice plane, i.e., away from $z = 0$. In the right hand side we have split the scalar lattice sum in a real space and reciprocal space part that read as reported by Linton [34] as follows:

$$\begin{aligned}\Gamma^{(1)} &= \frac{\pi}{A}\sum_{\mathbf{g}}\left\{\frac{e^{i(\mathbf{k}_{||}+\mathbf{g})\cdot\mathbf{r}_{||}}}{k_z^{\mathbf{g}}}\times\left[e^{ik_z^{\mathbf{g}}|z|}\mathrm{erfc}\left(\frac{k_z^{\mathbf{g}}}{2\eta}+|z|\eta\right)\right.\right.\\ &\qquad\left.\left.+e^{-ik_z^{\mathbf{g}}|z|}\mathrm{erfc}\left(\frac{k_z^{\mathbf{g}}}{2\eta}-|z|\eta\right)\right]\right\}\\ \Gamma^{(2)} &= \sum_{\mathbf{R}}\left\{\frac{e^{i\mathbf{k}_{||}\cdot\mathbf{R}}}{2\rho_{mn}}\times\left[e^{ik\rho_{mn}}\mathrm{erfc}\left(\rho_{mn}\eta+\frac{ik}{2\eta}\right)\right.\right.\\ &\qquad\left.\left.+e^{-ik\rho_{mn}}\mathrm{erfc}\left(\rho_{mn}\eta-\frac{ik}{2\eta}\right)\right]\right\}.\end{aligned} \tag{4.18}$$

The first term sums over all reciprocal lattice vectors $\mathbf{g}$ and in terms of its dependence on the 'observation' coordinate $\mathbf{r}$ at which it is evaluated explicitly splits in in-plane and transverse coordinates $(\mathbf{r}_{||}, z)$. All retardation effects in the plane appear explicitly through $\mathbf{k}_{||}\cdot\mathbf{r}_{||}$, while retardation transverse to the plane appears explicitly through $k_z^{\mathbf{g}} = \sqrt{k^2 - |\mathbf{k}_{||}+\mathbf{g}|^2}$. The second part $\Gamma^{(2)}$ sums over real space lattice vectors $\mathbf{R}$. In terms of the 'observation' coordinate $\mathbf{r}$ at which it is evaluated, each summand is essentially in a spherical coordinate, with dependence only on the radius $\rho_{mn} = |\mathbf{R}_{mn} - \mathbf{r}|$. Notice that since $\mathbf{r} = (\mathbf{r}_{||}, z)$ not only has a component parallel to the plane but also transverse to it, the $k\rho_{mn}$ terms account for retardation both in, and transverse, to the plane. As regards numerical implementation, the formulation holds for any choice of η; however optimal convergence requires η around$\sqrt{\pi}/a$ where a is the lattice constant. Pointers as to how to apply the operator Eq. (4.16) and how many terms to sum are contained in Ref. [23].

4.10 References

[1] A. V. Kildishev, A. Boltasseva, and V. Shalaev, *Planar photonics with metasurfaces*, Science **339** (2013).

[2] X. Ni, S. Ishii, A. Kildishev, and V. Shalaev, *Ultra-thin, planar, Babinet-inverted plasmonic metalenses*, Light Sci. Appl. **2** (2013).

[3] N. Yu, F. Aieta, P. Genevet, M. A. Kats, Z. Gaburro, and F. Capasso, *A broadband, background-free quarter-wave plate based on plasmonic metasurfaces*, Nano Lett. **12**, 6328 (2012).

[4] A. Alù and N. Engheta, *Plasmonic and metamaterial cloaking: physical mechanisms and potentials*, J. Opt. A **10**, 093002 (2008).

[5] F. Aieta, P. Genevet, M. Kats, N. Yu, R. Blanchard, Z. Gaburro, and F. Capasso, *Aberration-free ultrathin flat lenses and axicons at telecom wavelengths based on plasmonic metasurfaces.*, Nano Lett. **12**, 4932 (2012).

[6] J. Sun, E. Timurdogan, A. Yaacobi, E. S. Hosseini, and M. R. Watts, *Large-scale nanophotonic phased array*, Nature **493**, 195 (2013).

[7] M. A. Kats, P. Genevet, G. Aoust, N. Yu, R. Blanchard, F. Aieta, Z. Gaburro, and F. Capasso, *Giant birefringence in optical antenna arrays with widely tailorable optical anisotropy*, Proc. Natl. Acad. Sci. U.S.A. **109**, 12364 (2012).

[8] C. M. Soukoulis, S. Linden, and M. Wegener, *Negative refractive index at optical wavelengths*, Science **315**, 47 (2007).

[9] K. Busch, G. von Freymann, S. Linden, S. Mingaleev, L. Tkeshelashvili, and M. Wegener, *Periodic nanostructures for photonics*, Phys. Rep. **444**, 101 (2007).

[10] N. Feth, M. König, M. Husnik, K. Stannigel, J. Niegemann, K. Busch, M. Wegener, and S. Linden, *Electromagnetic interaction of split-ring resonators : The role of separation and relative orientation*, Opt. Expr. **18**, 215 (2010).

[11] M. Decker, R. Zhao, C. M. Soukoulis, S. Linden, and M. Wegener, *Twisted split-ring-resonator photonic metamaterial with huge optical activity*, Opt. Lett. **35**, 1593 (2010).

[12] C. Enkrich, M. Wegener, S. Linden, S. Burger, L. Zschiedrich, F. Schmidt, J. F. Zhou, T. Koschny, and C. M. Soukoulis, *Magnetic metamaterials at telecommunication and visible frequencies*, Phys. Rev. Lett. **95**, 203901 (2005).

[13] C. Rockstuhl, T. Zentgraf, H. Guo, N. Liu, C. Etrich, I. Loa, K. Syassen, J. Kuhl, F. Lederer, and H. Giessen, *Resonances of split-ring resonator metamaterials in the near infrared*, Appl. Phys. B **84**, 219 (2006).

[14] I. Sersic, C. Tuambilangana, T. Kampfrath, and A. F. Koenderink, *Magnetoelectric point scattering theory for metamaterial scatterers*, Phys. Rev. B **83**, 245102 (2011).

[15] N. Liu, H. Liu, S. Zhu, and H. Giessen, *Stereometamaterials*, Nat. Photon. **3**, 157 (2009).

[16] A. Serdyukov, I. Semchenko, S. Tretyakov, and A. Sihvola, *Electromagnetics of Bi-anisotropic Materials: Theory and Applications*, Electrocomponent science monographs, Gordon and Breach Science, Amsterdam, The Netherlands, 1 edition, 2001.

[17] F. J. García de Abajo, *Colloquium: Light scattering by particle and hole arrays*, Rev. Mod. Phys. **79**, 1267 (2007).

[18] M. Husnik, M. W. Klein, N. Feth, M. Koenig, J. Niegemann, K. Busch, S. Linden, and M. Wegener, *Absolute extinction cross-section of individual magnetic split-ring resonators*, Nat. Photon. **2**, 614 (2008).

[19] I. Sersic, M. A. van de Haar, F. Bernal Arango, and A. F. Koenderink, *Ubiquity of optical activity in planar metamaterial scatterers*, Phys. Rev. Lett. **108**, 223903 (2012).

[20] F. Bernal Arango and A. F. Koenderink, *Polarizability tensor retrieval for magnetic and plasmonic antenna design*, New J. Phys. **15**, 1073023 (2013).

[21] M. Decker, S. Linden, and M. Wegener, *Coupling effects in low-symmetry planar split-ring resonator arrays*, Opt. Lett. **34**, 1579 (2009).

[22] P. de Vries, D. V. van Coevorden, and A. Lagendijk, *Point scatterers for classical waves*, Rev. Mod. Phys. **70**, 447 (1998).

[23] P. Lunnemann, I. Sersic, and A. F. Koenderink, *Optical properties of two-dimensional magnetoelectric point scattering lattices*, Phys. Rev. B **88**, 245109 (2013).

[24] I. Sersic, C. Tuambilangana, and A. F. Koenderink, *Fourier microscopy of single plasmonic scatterers*, New J. Phys. **13**, 083019 (2011).

[25] I. Sersic, M. Frimmer, E. Verhagen, and A. F. Koenderink, *Electric and magnetic dipole coupling in near-infrared split-ring metamaterial arrays*, Phys. Rev. Lett. **103**, 213902 (2009).

[26] E. Plum, J. Zhou, J. Dong, V. A. Fedotov, T. Koschny, C. M. Soukoulis, and N. I. Zheludev, *Metamaterial with negative index due to chirality*, Phys. Rev. B **79**, 035407 (2009).

[27] E. Plum, X. . X. Liu, V. A. Fedotov, Y. Chen, D. P. Tsai, and N. I. Zheludev, *Metamaterials: Optical activity without chirality*, Phys. Rev. Lett. **102**, 113902 (2009).

[28] E. Plum, V. A. Fedotov, and N. I. Zheludev, *Asymmetric transmission: a generic property of two-dimensional periodic patterns*, J. Opt. **13**, 024006 (2011).

[29] S. Tretyakov, C. Simovski, and A. Sochava, *Advances in Complex Electromagnetic Materials*, volume 28 of *NATO ASI Series High Technology*, Kluwer Academic Publishers, Dordrecht, The Netherlands, 1997.

[30] A. Kwadrin and A. F. Koenderink, *Probing the electrodynamic local density of states with magnetoelectric point scatterers*, Phys. Rev. B **87**, 125123 (2013).

[31] Z. Ku, K. M. Dani, P. C. Upadhya, and S. R. J. Brueck, *Bianisotropic negative-index metamaterial embedded in a symmetric medium*, J. Opt. Soc. Am. B **26**, B34 (2009).

[32] B. Gompf, J. Braun, T. Weiss, H. Giessen, M. Dressel, and U. Hübner, *Periodic nanostructures: Spatial dispersion mimics chirality*, Phys. Rev. Lett. **106**, 185501 (2011).

[33] H. Liu, J. X. Cao, S. N. Zhu, N. Liu, R. Ameling, and Giesse, *Lagrange model for the chiral optical properties of stereometamaterials*, Phys. Rev. B **81**, 241403 (2010).

[34] C. Linton and I. Thompson, *One- and two-dimensional lattice sums for the three-dimensional Helmholtz equation*, J. Comp. Phys. **228**, 1815 (2009).

Chapter 5

Backaction on a lattice of scatterers in front of a reflective interface

In this chapter, we study back scattering on scatterers, as in Chapter 3, however for periodic lattices of scatterers, as in Chapter 4. In particular, we ask how the response of a lattice of scatterers is modified when the lattice is held in front of a reflective interface. We set up an analytical point scattering model to calculate the response of scatterers at a planar interface taking all electrodynamic retarded multiple scattering interactions into account. We show that while the polarizability of scatterers is strongly affected by their environment, the reflectivity of the combined system is quite close to that predicted from the bare lattice reflectivity and the bare interface reflectivity in a Fabry-Pérot model. Furthermore, we isolate the subtle deviations in a 'reflectivity-backaction' effect. Finally, we present preliminary results from an experiment on split ring arrays at controlled distance from a mirror, as realized using the fabrication technique of Chapter 2.

5.1 Introduction

If it has a size smaller than the wavelength, a single scatterer in vacuum can be described in a point dipole model by a dynamic polarizability tensor $\boldsymbol{\alpha}$ that fulfills energy conservation by taking the radiation damping for free space into account [1, 2, 3]. Changing the environment of a single magneto-electric scatterer, for instance by simply placing it in front of a mirror affects the particle's polarizability which in turn becomes separation dependent in an intriguing way as we report in Chapter 3. In essence, this can be viewed as a backaction effect whereby a scatterer interacts with its own scattered light that returns to the scatterer via the mirror, similar to the backaction effect that normalizes the linewidth and resonance of a radiating atom or molecule [4]. In Chapter 4, we report that the polarizability also effectively gets renormalized for periodic arrangements of such scatterers. In this case, the renormalization is not due to the multiple scattering interaction of a scatterer with a mirror, but with all other scatterers in the lattice, leading to significant lattice-dependent resonance shifts and broadenings of experimentally accessible quantities such as the reflection coefficient for infinite (non-)diffractive 2D lattices, as discussed in [5] and 4. The open question we would like to address in this chapter is how these two renormalization steps will manifest themselves in a combined system of a lattice of scatterers separated from an interface. Furthermore, we investigate to which extent, if at all, the combined system of a lattice and a mirror can be treated within a Fabry-Pérot model as proposed by Ameling et al., and whether or not backaction should be included in this case [6, 7, 8].

We present our results according to the following structure. First, we present an analytical approach to selfconsistently calculate the optical response of a lattice of point scatterers embedded in a stratified system. This approach combines the lattice-sum formalism of Chapter 4 with the interface Green function approach of Chapter 3. Next we examine the effective per-particle polarizability as a function of its environment. In particular, exactly according to the reasoning in Chapter 3, the effect of a nearby interface on a particle is to renormalize the extent to which it can be polarized by a given incident field applied at its location. In a similar way the per-particle polarizability is renormalized by the presence of all other particles in a lattice arrangement. Finally, these two effects add up in a nontrivial fashion once one places a lattice of particles in front of an interface. In section 5.3 we compare predictions for these three cases. Next we turn to predicted reflectivity coefficients of lattices of resonant particles held in front of a mirror as predicted from our exact theory for point scattering lattices in front of interfaces. Resonant features of the lattice together with interference from the various multiple reflections conspire to give a complex frequency and

distance dependence reminiscent of the physics of a Fabry-Pérot resonator comprised of a mirror geometrically separated from a second interface that features a resonant response.

Finally, we examine the Fabry-Pérot analogy in more detail. Using just the reflection constant of mirror and bare lattice, we evaluate what a simple Fabry-Pérot model would predict for the composite structure, and show subtle deviations from the full point scattering model. One striking interpretation is that the reflection coefficient of just the lattice that one needs to enter in the Fabry-Pérot model varies as function of distance to the mirror, as opposed to the standard theory for etalons where solely the interface separation enters as a phasefactor. By inverting the Fabry-Pérot model we can retrieve the effective reflection constant of the lattice from the full calculation. This effective reflection constant varies with distance to the mirror in an oscillatory manner analogous to that in which the polarizability of a particle varies with mirror-particle separation. We thus predict a subtle backaction effect on the reflectivity of metasurfaces.

5.2 Theory

Our goal is finding the full *lattice-summed* Green function $\mathcal{G}$ for a system composed of a two-dimensional, infinite lattice of point scatterers separated by a distance d from, and parallel to, an interface. The two media forming the interface are assumed to be simple homogeneous media described by dielectric constants ε.

As in Chapter 4, our starting point is that the response of a periodic lattice of polarizable point particles illuminated by a plane wave (parallel wave vector $\mathbf{k}_{\parallel}$) can be summarized entirely by the response of the particle at the lattice origin which reads

$$\begin{pmatrix} \boldsymbol{p} \\ \boldsymbol{m} \end{pmatrix} = \boldsymbol{\alpha} \left[\begin{pmatrix} \boldsymbol{E} \\ \boldsymbol{H} \end{pmatrix} + \sum_{n \neq 0} \mathbf{G}((\mathbf{R}_n, d), (0, d)) e^{i\mathbf{k}_{||} \cdot \mathbf{R}_n} \begin{pmatrix} \boldsymbol{p} \\ \boldsymbol{m} \end{pmatrix} \right]. \tag{5.1}$$

Here, $\mathbf{R}_n$ are real space lattice vectors, while d is the height along z where the lattice that is parallel to the (x, y)-plane is situated. In this work, we take the interface at $z = 0$. Exactly as in Chapter 4, $\mathbf{G}(\mathbf{r}, \mathbf{r}')$ denotes the dyadic Green function in absence of the lattice, i.e., for a single dipole, while with $\mathcal{G}$ we will denote the lattice-summed Green function. The polarizability $\boldsymbol{\alpha}$ must be chosen to represent a self-consistent scatterer in presence of the environment specified by $\mathbf{G}(\mathbf{r}, \mathbf{r}')$, meaning it must be corrected for the presence of the substrate exactly as Chapter 3, Eq. 3.2. We recall that for an interface system, the dyadic Green function can be separated as a free

space and reflected part

$$\mathbf{G}_{\text{full}}(\boldsymbol{r}, \boldsymbol{r'}) = \mathbf{G}_{\text{free}}(\boldsymbol{r}, \boldsymbol{r'}) + \mathbf{G}_{\text{refl}}(\boldsymbol{r}, \boldsymbol{r'}). \tag{5.2}$$

Therefore, also the lattice-summed Green function $\mathcal{G}^{\neq}$ can be written as a sum of a free space and a reflected part.

$$\mathcal{G}^{\neq}(\mathbf{k}_{\parallel}, \mathbf{r}) = \mathcal{G}^{\neq}_{\text{free}}(\mathbf{k}_{\parallel}, \mathbf{r}) + \mathcal{G}^{\neq}_{\text{refl}}(\mathbf{k}_{\parallel}, \mathbf{r}). \tag{5.3}$$

We will not discuss the lattice summation required to obtain $\mathcal{G}_{\text{free}}$ as it was the topic of Chapter 4. If one desires one can rewrite the problem such that one uses the bare polarizability α_0 in *absence* of the interface, noting that the required lattice sum without the term at the origin then reads

$$\mathcal{G}^{\neq}(\mathbf{k}_{\parallel}, \mathbf{r}) = \mathcal{G}^{\neq}_{\text{free}}(\mathbf{k}_{\parallel}, \mathbf{r}) + \mathcal{G}_{\text{refl}}(\mathbf{k}_{\parallel}, \mathbf{r}). \tag{5.4}$$

In terms of mirror images, the interpretation is that a given particle interacts with all the particles except itself in the physical lattice, and furthermore with all the mirror imaged scatterers *including* its own mirror image. For a lattice in the (x, y)-plane at $z = 0$ and the reflective interface at a distance d at $z = -d$ the Green function for the reflected part reads

$$\begin{aligned} \mathcal{G}_{\text{refl}}(\mathbf{k}_{\parallel}, \mathbf{r}) &= \sum_{m,n} \mathbf{G}_{\text{refl}}(\mathbf{R}_{mn} - \mathbf{r}_{\parallel}) e^{i\mathbf{k}_{\parallel}\cdot\mathbf{R}_{mn}} \\ &= \sum_{m,n} \frac{i}{2\pi} \left[\int d\mathbf{q} \frac{1}{k_z} \mathbf{M}_{\text{refl}} e^{i\mathbf{q}\cdot(\mathbf{R}_{mn}-\mathbf{r})} e^{ik_z|z+2d|} \right] e^{i\mathbf{k}_{\parallel}\cdot\mathbf{R}_{mn}} \end{aligned} \tag{5.5}$$

where the 6×6 matrix $\mathbf{M}_{\text{refl}}$ depends on the wavevector $\mathbf{q}$ and the Fresnel coefficients of the interface exactly as specified in Equations 3.4, 3.5 and 3.6 of Chapter 3. By making use of the 'completeness' of the lattice

$$\sum_{m,n} e^{i\mathbf{k}_{\parallel}\cdot\mathbf{R}_{mn}} = \frac{(2\pi)^2}{\mathcal{A}} \sum_{m,n} \delta(\mathbf{k}_{\parallel} - \mathbf{g}_{mn}), \tag{5.6}$$

one can evaluate the expression for $\mathcal{G}_{\text{refl}}$ as a sum over the reciprocal lattice, thereby avoiding the calculation of a sum over poorly converging Sommerfeld integrals entirely. Indeed it is remarkable that owing to parallel wave vector conservation, the interface lattice sum is *easier* to calculate than the interface Green function. The sum reads

$$\mathcal{G}_{\text{refl}}(\mathbf{k}_{\parallel}, \mathbf{r}) = \frac{2i\pi}{\mathcal{A}} \sum_{m,n} \frac{1}{k_z^{\mathbf{g}}} \mathbf{M}_{\text{refl}} e^{i(\mathbf{k}_{\parallel}+\mathbf{g})\cdot\mathbf{r}_{\parallel})} e^{ik_z^{\mathbf{g}}|z+2d|}. \tag{5.7}$$

Far field observables, i.e., reflection, transmission and diffraction efficiencies follow simply once the induced polarizability has been solved for, by using the far field asymptotic expansion of the reflected part of the Green function listed in Novotny and Hecht, Chapter 10 [2].

5.3 Results

Renormalized polarizabilities

In this section we study the response of two-dimensional lattices of non-magnetic resonant scatterers to the driving by a normal-incidence plane wave with an x-polarized electric field. As we assume no direct magnetic response and no cross-coupling response, the sole consequence of this driving condition is the generation of an electric dipole moment at the scatterers position. Therefore, within our point scattering theoretical treatment the static polarizability parameters read: $\{\eta_E, \eta_H, \eta_C\} = \{1, 0, 0\}$. The resonant feature is described by the following parameters: resonance frequency $\omega_0 = 1.26 \times 10^{15}\,\mathrm{s}^{-1}$ corresponding to a free space wavelength of $\lambda = 1500\,\mathrm{nm}$, an ohmic damping rate of $1.25 \times 10^{14}\,\mathrm{s}^{-1}$, and a volume of $200 \times 200 \times 30\ \mathrm{nm}^3$. The single-particle dynamic polarizability will be renormalized due to first, the presence of the interface, which we take to be a silver mirror (we use tabulated optical constants from [9]) and second, due to the presence of all other scatterers in the lattice. Through the help of Figure 5.1, we examine each of these renormalization steps.

In Figure 5.1, we compare the frequency and distance dependent imaginary part of the dynamic polarizability (x-component) for a single scatterer and lattices with different pitch in front of the silver mirror. We focus on the imaginary part of the polarizability, because for a scatterer in free space $4\pi k\,\mathrm{Im}\alpha$ can be identified with the scatterer's extinction cross section. For the chosen scatterer the imaginary part of the polarizability presents a Lorentzian peak at 1500 nm and a peak extinction cross section of $\approx 0.3\,\mu\mathrm{m}^2$, about an order of magnitude larger than the geometrical cross section indicating that our parameters correspond to an archetypical plasmonic scatterer. At any fixed distance to the mirror, the single-scatterer polarizability (Fig.5.1, a) presents a clearly defined resonance around the single particle resonance. The resonance width, center frequency and strength varies with distance due to interaction of the single scatterer with its own mirror image. For very small separations less than 100 nm, the resonances in fact red shift when approaching the mirror. However, we note that in this range the dipole approximation is not valid, as the separation is smaller than the assumed particle size. Therefore, throughout this chapter, we omit in all plots separations below 100 nm. This effect is exactly as discussed in Chapter 3. The polarizability at the resonance angular frequency is weakly oscillating with distance at a periodicity of $\approx 800\,\mathrm{nm}$. We fit a Lorentzian lineshape to the polarizability to retrieve the full-width half-maximum (FWHM) linewidth change with distance. The extracted single-particle polarizability linewidth follows the (purely electric) LDOS-lineshape

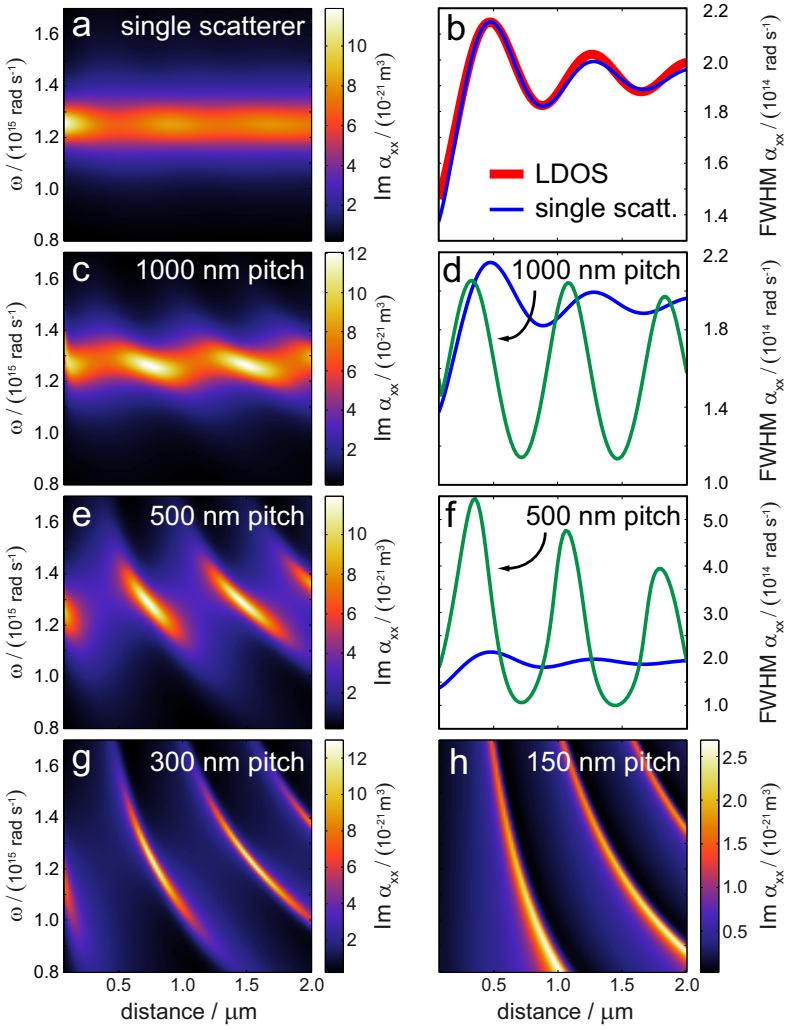

Figure 5.1: Point dipole lattice-sum calculations to retrieve the polarizability of non-magnetic ($\{\eta_E, \eta_H, \eta_C\} = \{1, 0, 0\}$) resonant scatterers ($\lambda = 1500\,\mathrm{nm}$, ohmic damping rate: $1.25 \times 10^{14}\,\mathrm{s}^{-1}$) at a distance from a silver interface driven by an x-polarized plane wave under normal incidence. The single-particle polarizability (a) varies with distance due to the interaction with its mirror image. The single-particle polarizability linewidth follows the local density of states lineshape for the vac/silver interface (b). Lattice arrangements of 1000 nm (c), 500 nm (e), 300 nm (g), and 150 nm pitch reveal the increased dispersivnes. For the single scatterer and two most dilute lattice cases it is feasible to compare the single particle linewidth to the overall lattice polarizability linewidth. For 1000 nm pitch (d), the single particle contribution is of comparable strength, while for 500 nm pitch (f), the renormalization effect stemming from the lattice dominates the linewidth.

for a vac/silver interface (Fig. 5.1, b).

Having presented the results for a single particle in free space and in front of a mirror, we now turn to the effective polarizability per object for the case of a lattice in front of a mirror. In Figure 5.1, left column, we present the lattice- and interface-normalized single particle polarizability covering a range of pitches from the dilute (1000 nm pitch) to the dense (150 nm pitch) case. Evidently, the polarizability reduces strongly and broadens significantly with increasing density. This effect is well known from Sersic et al. [10], and is due to the fact that many dipoles oscillating in phase ($k_{||} = 0$) experience superradiant damping (radiated power of N dipoles being proportional to N^2). Another viewpoint is that the extinction cross section $4\pi k \mathrm{Im}\alpha$ per object must remain below the unit cell area, limiting the per-building block α.

Going from dilute to dense lattices the polarizability is more and more dominated by a strong feature that is neither solely attributable to the interface, nor to the lattice alone. Indeed, the fringes in polarizability magnitude apparent for the single particle appear to sharpen considerably, and to become very strongly dispersive, forming features along lines of constant d/λ. The oscillation period reduces to ≈ 750 nm, i.e., half the single-particle resonance wavelength.

While for the dilute lattice the modification of the polarizability is subtle and the single particle resonance is still clearly visible at any lattice mirror separation, for the densest lattices the fringes essentially span over the entire frequency axis. This notion is consistent with the fact that for dense bare lattices, the single particle polarizability looses relevance, as the polarizabiltiy is increasingly determined by just the unit cell area. For such dense lattices, the calculated effective polarizability in effect implies that a strong dipole can be induced only whenever the lattice and the mirror satisfy a Fabry-Pérot resonance condition. It should be noted that the areal density of maximum achievabe polarization is high, especially for the 300 nm pitch lattice, which could be beneficial for, e.g., fluorescence or sensing applications.

The right column of Figure 5.1 shows accompanying graphs depicting the FWHM dependence of the lattice and interface normalized polarizability (green). The single-particle polarizability renormalized for the presence of the interface depicted in Figure 5.1, b serves as a reference in all the FWHM plots. In this way, this common contribution independent on the lattice pitch can be compared to the pure lattice renormalization. Clearly, for a dilute lattice (1000 nm lattice pitch) Figure 5.1, d the interface and lattice contribution to the linewidth is of comparable strength. For a lattice pitch of 500 nm the renormalization effect stemming from the lattice already dominates the linewidth, being about three times larger than the

interface contribution on average across the whole distance range. For even denser lattices (300 nm and 150 nm pitch) it is unfeasible to attribute a single particle polarizability linewidth.

To conclude, as in the single particle case, a renormalization of the lattice polarizability occurs when a lattice is held in front of an interface. In contrast to the case of a single particle, this modification has a period exactly $\lambda/2$, and a modulation depth that stays much stronger for larger distances. The period, and the fact that one observes an only weakly damped oscillation of absolute polarizability is indicative for the fact that backaction is now through an entire extended lattice of mirror dipoles. Importantly, while a single particle mirror image yields backaction through a spherical wave, for a mirror-image of scatterers forming a periodic array, backaction is through a reflected wave at $k_{\parallel} = 0$ stemming from combined and fixed-phase related outgoing and receiving reflected plane waves.

Point dipole lattice-sum calculations

We now turn from polarizability to an actual observable, i.e., the reflection coefficient. We discuss reflection coefficients that we have calculated through the exact Green function formalism that we set up in the Theory section. For comparison we plot the absolute squared of the frequency dependent reflection coefficient $r^{\mathrm{PD}}_{\mathrm{lattice}}$ stemming from point dipole (PD) lattice-sum calculations for the non-magnetic scatterers arranged in a 2D square lattice in *absence* of the mirror (Fig. 5.2, a) alongside calculations that contain the mirror (Fig. 5.2, b). For now, we focus on a relatively dilute lattice with a pitch of 1000 nm. The results for other lattice pitches will be presented below. We assert that for the dilute case the absolute squared value of the reflection amplitude is small in the whole frequency range, varying from 0.5% to about 5.5% at the resonance frequency. Of course, in absence of any mirror, shifting the lattice away from $z = 0$ leaves the reflection coefficient constant. Figure 5.2, b shows the reflection coefficient $\left|r^{\mathrm{PD}}_{\mathrm{stack}}\right|^2$ that we calculate for the full system. The off-resonant absolute squared value of the full stack reflection coefficient is almost 100 % throughout the distance range as expected as at these frequencies it is dominated by the reflection of the silver mirror. On-resonance, we recover a low reflectivity of less than 10 % for the most part of the distance range. Only at specific, periodically occurring distances, 'sharp' features of highly reflective r dissect the reflection dips. We note that the combined system has a *large* range of reflectivity, i.e, a large reflectivity contrast of $[1\%, 95\%]$, while the individual interfaces both feature a *small* reflectivity contrast of $[0.5\%, 5.5\%]$ for the lattice and $[98\%, 99\%]$ for the mirror for the reported angular frequency range of $[0.8, 1.7] \times 10^{15}\,\mathrm{rad\,s^{-1}}$ corresponding to a wavelength range of $[1.1, 2.4]$ µm. The fact that fringes

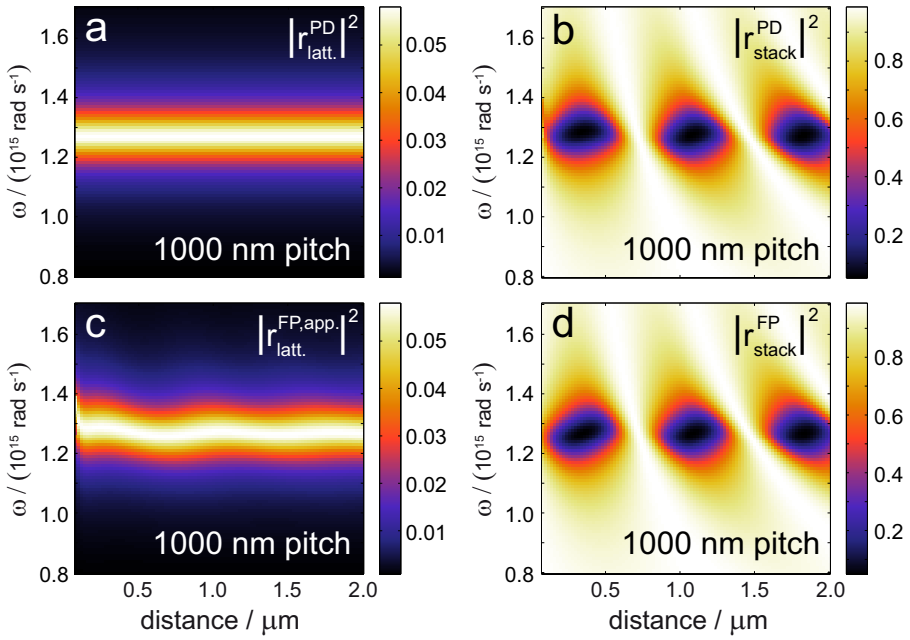

Figure 5.2: The reflection coefficient for a lattice of non-magnetic scatterers (1000 nm pitch) from lattice-sum point-dipole calculations embedded in vacuum (a); and forming a stack being at a distance to a silver mirror (b). Off-resonance, the overall reflectivity is dominated by the high reflectivity of the silver mirror. On-resonance, a low reflectivity of less than 10% is recovered, only dissected by sharp regions of high reflectivity at specific distances where the round trip path length coincides with integer multiples of a full wavelength. The low lattice reflectivity and the high reflectivity of the mirror lead to a high reflectivity contrast in the combined system. A Fabry-Pérot model for the stack retrieves the same general reflectivity dependence (d). The apparent lattice reflectivity (c) that, used in the Fabry-Pérot model, would lead to the full point-dipole lattice-sum result shows a distance dependent oscillation, revealing the backaction of mirror dipoles on the lattice.

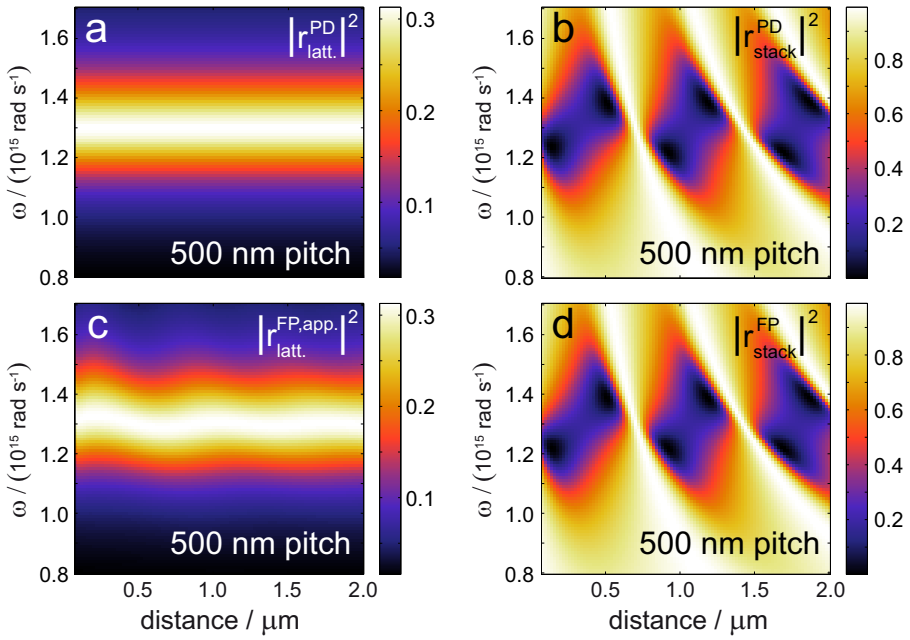

Figure 5.3: As we decrease the lattice pitch to 500 nm the free-space lattice reflectivity (a) will broaden around the single-particle resonance, which in this case increases to about 30%. The reflectivity dips for the combined system of lattice and mirror (b,d) are more frequency dispersive compared to the dilute case of 1000 nm pitch in Fig. 5.2. As in the dilute case, the apparent lattice reflectivity (c) features a distance dependent oscillation due to backaction of mirror dipoles.

occur at $\lambda/2$ intervals is entirely consistent with the idea of a Fabry-Pérot resonator which is governed by constructive interferences when the round trip accumulates a full wavelength ($2kd = m2\pi$). Also it is intuitively reasonable that the resonance bandwidth limits the frequency range over which fringes are visible. Quite remarkable is that the very weak, and partially absorbing, resonance of the metasurface translates to a big contrast in reflection in the Fabry-Pérot geometry, and concomitantly also in a very big enhancement in absorption efficiency of the scatterers.

Fabry-Pérot model

While qualitatively, the features of the reflectivity of the full system might be similar to that of a Fabry-Pérot model, here we ask in how far this similarity is quantitative. Let us assume we can set up a Fabry-Pérot (FP)

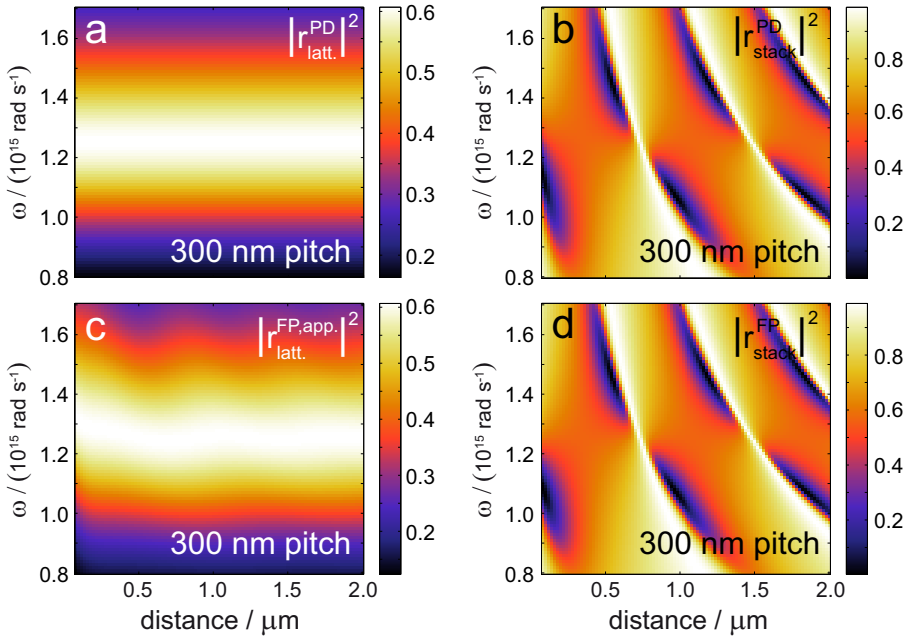

Figure 5.4: Going to even denser lattices with a pitch of 300 nm, the free-space lattice reflectivity is broadened further and reaches values $> 60\%$ (a). Mirror and lattice form a stack featuring a total reflectivity with highly dispersive lineshapes (b,d). The lattice response function undergoes a π phase flip at the lattice resonance causing the reversal of reflectivity contrast from high/low to low/high passing a dispersive feature from small to larger distances.

model for a vac/lattice/vac/mirror system with a varying thickness for the vac-layer in between the lattice and the mirror as shown in Figure 5.6). The etalon-reflectivity formula predicts

$$r^{\mathrm{FP}}_{\mathrm{stack}} = r_{12} + \frac{t_{21} r_{23} t_{12} \left(-e^{2in_2kd}\right)}{1 - r_{21} r_{23} \left(-e^{2in_2kd}\right)} \tag{5.8}$$

for the complex amplitude reflection coefficient of a system characterized by a mirror reflection amplitude coefficient r_{23}, and with r_{12}, t_{12} being the complex reflection and transmission coefficients of the first layer, i.e., the lattice in this work as calculated within the point dipole model. For the second interface, the complex amplitude reflection coefficient r_{23} of a vac/silver interface is simply the Fresnel coefficient (deduced from the tabulated complex refractive index data), exactly the same as it enters in the full point dipole model. In a standard Fabry-Pérot model, r_{12} and t_{12} of the *first*

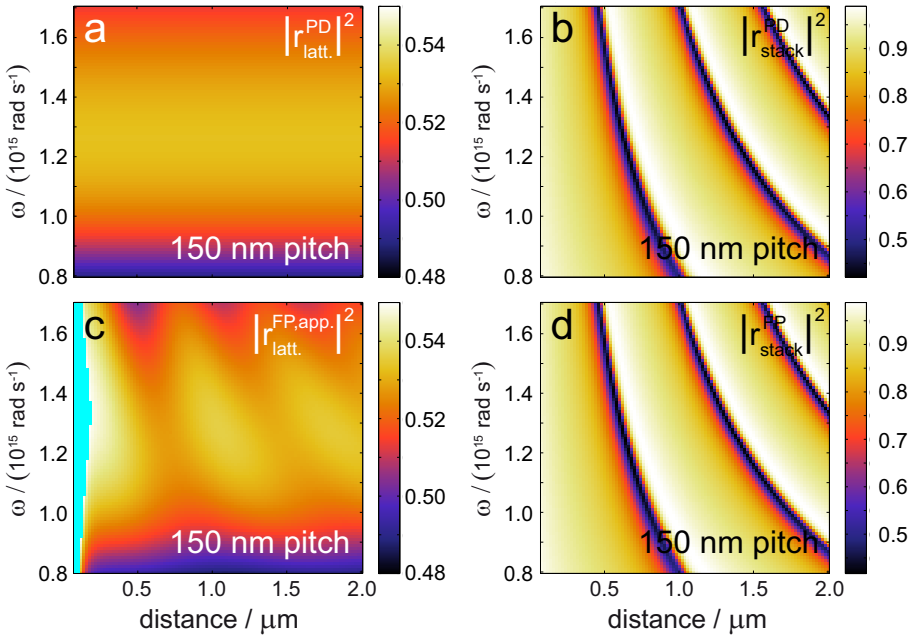

Figure 5.5: The reflection coefficient for a lattice of non-magnetic scatterers in the most dense case (150 nm pitch). The reflection coefficient from point dipole calculation for the lattice in vacuum (a) shows a significantly frequency-broadened high reflectivity of $> 50\%$, about ten times higher than for the retrieved maximum value for the most dilute case (1000 nm pitch) presented in Fig. 5.2. The total reflectivity of the combined system of lattice and mirror (b, d), is high ($> 90\%$) except for sharp reflectivity dip features ($< 50\%$) resembling those of a typical etalon; the single-particle resonance is not visible for such dense lattice arrangements. The apparent lattice reflectivity (c) however, still retains the distance dependence. Reflectivity values exceeding the presented color scale, which is the case for small distances (< 100 nm) have been omitted in order to visualize (c) and (a) on comparable scale.

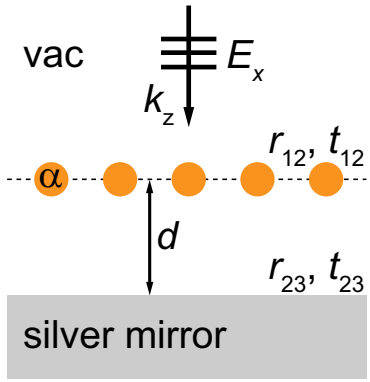

Figure 5.6: Fabry-Pérot system: a lattice (amplitude reflection coefficient for normal incidence: r_{12}) separated from a mirror (r_{23}) by a distance d

layer are *independent* of the presence of the second layer. Therefore, let us evaluate the Fabry-Pérot equation taking for the first interface the complex amplitude reflection and transmission coefficients of the vac/lattice interface from our point-dipole calculations *in absence* of the mirror. Figure 5.2, a shows the lattice reflectivity in *absence* of the mirror, while Figure 5.2, d shows $\left|r^{\mathrm{FP}}_{\mathrm{stack}}\right|^2$, the absolute squared of the amplitude reflection coefficient for the combined system according to the Fabry-Pérot model. Compared to the point dipole calculation result, we find a similar distance dependence and reflectivity contrast. However, the Faby-Pérot model fails to retrieve the resonance frequency shift for small separations and underestimates the resonance feature width.

Inverse Fabry-Pérot model

To extract exactly how the full result for the reflectivity from point dipole calculations and the simple Fabry-Pérot model differ, we ask the following question: suppose one would apply the Fabry-Pérot model, then what is the *apparent* lattice reflectivity that makes the Fabry-Pérot model match the full calculation? In essence this question boils down to asking what apparent reflectivity constant one would retrieve for the lattice given the full reflectivity and the geometry of the stack. The exact same question one could address in an experiment, provided one would acquire the necessary phase information to retrieve complex reflection coefficients, a usual requirement when attempting to retrieve the effective optical constants of metamaterials and metasurfaces. Evidently, this might result in an effective reflectivity that depends on distance between lattice and mirror. We note

that Eq. 5.8 can be inverted by very simple algebra to obtain a complex r with no ambiguity. We solve for the apparent reflection coefficient for the lattice of pitch 1000 nm, and plot the resulting $\left|r_{\text{latt.}}^{\text{FP,app.}}\right|^2$ in Figure 5.2, c. Clearly the retrieval is successful, in that the retrieved apparent reflectivity does not show the very strong fringing contrast of the composite system. Indeed, one would expect for a normal FP a completely distance independent apparent reflectivity that exactly matches that of the bare lattice. However, the apparent reflectivity *does* depend on the distance to the lattice. The resonance frequency oscillates with distance to the mirror. It should be noted that while the effective reflectivity resonance of the lattice varies in center frequency and width in a manner that is qualitatively reminiscent of the variation in polarizability, the variation is much less strong in amplitude. Qualitatively, whenever the lattice and its mirror image form a subradiant pair, their polarizability is highest due to the weak radiative damping. Yet at the same time, the overall radiated strength per unit of induced dipole moment will not be large owing to the destructive interference of the lattice and its mirror image. The converse reasoning holds for separations at which the lattice and its mirror image form a superradiant pair. From this reasoning, it is evident that variations in polarizability are much larger than those in reflection constant. This distinction should be important when utilizing meta-surfaces in near field aplications.

To conclude, the reflectivity of a stack that consists of a metasurface in front of a reflector can be interpreted very well as a Fabry-Pérot resonator, provided, however, one is willing to accept that the reflectivity of the metasurface depends on its environment due to interaction with its own mirror image. This is a backaction effect analogous to the modification of a particle polarizability due to hybridization of its own mirror image, constituting both a frequency shift and width change of the resonant response.

Different lattice density

Finally, we follow the same procedure for smaller lattice pitches of 500 nm (Fig. 5.3), 300 nm (Fig. 5.4), and 150 nm (Fig. 5.5). The smaller the lattice pitch, the larger $\left|r_{\text{lattice}}^{\text{PD}}\right|^2$ for the lattice in vacuum: namely up to 60% for 300 nm; a 10-fold increase compared to a maximum of about 6% for 1000 nm lattice pitch, roughly commensurate with the order of magnitude higher surface coverage. Furthermore, the angular frequency width of the resonance feature is larger, the smaller the lattice pitch. The increase of the reflection coefficient and the broadening of the resonance in frequency space is expected when going to denser lattices given the larger areal density of scattering objects, and the effect of superradiant damping.

For the dilute lattice in front of the mirror, we have seen the reflection coefficient being dominated by resonant absorption peaks, leading to a high reflection contrast. While the reflection coefficient contrast for stacks formed with denser lattices stays similarly high ($[5\%, 95\%]$ for 500 nm and 300 nm; $[40\%, 95\%]$ for 150 nm), sharp dispersive features in the reflection coefficient are present. For the lattice with a pitch of 300 nm, the reflectivity is qualitatively very different, having gone from absorptive features on a high background to asymmetric dispersive lineshapes. The reversal of contrast at $1.2 \times 10^{15}\,\mathrm{rad\,s^{-1}}$, i.e., whether the reflectivity is low or high to the left, or the right of the Fabry-Pérot resonance is due to the lattice resonance, whose response function goes through a π phase flip. This transition could be understood as a transition from coherent mixing of a continuum (mirror reflectivity) with a weak absorption resonance (dilute lattices, walking along paths of constant separation), to mixing of a continuum (mirror reflectivity) with a strong resonance (lattice response). Thus the lineshape change is akin to that in the families of lineshapes of the Fano interference effect that has attracted significant attention in many communities, including recently that of optical scattering [11].

Finally, we discuss our results in view of the work of Ameling et al. who calculated reflectivity in terms of the simple Fabry-Pérot model, without taking backaction into account [6, 7, 8]. It should be noted that in all cases, the differences between the full reflection constant and the simple Fabry-Pérot model are subtle. Thereby, the model of Ameling et al. is effectively validated by our full multiple scattering calculation. For all lattices, the apparent lattice reflection constant experiences backaction but observing signatures of this backaction in experiments will be difficult, as the total reflection amplitude and phase must be measured very accurately for an accurate retrieval of the effective lattice reflectivity. The most remarkable conclusion of our calculation, which adds insight beyond the Fabry-Pérot model is that, while in a Fabry-Pérot interpretation of the reflectivity, the reflectivity of the lattice varies only moderately with distance to the mirror, in fact the dipole that can be induced in each particle with a set incident field varies remarkably strongly. Therefore, sharp features would be expected in experiments that are sensitive to excitation strength in the near field. This conclusion might be relevant for instance when using particle lattices to enhance pump light absorption and fluorescence emission in white light LED scenarios, where blue LED light is upconverted using green and red emitting phosphors [12].

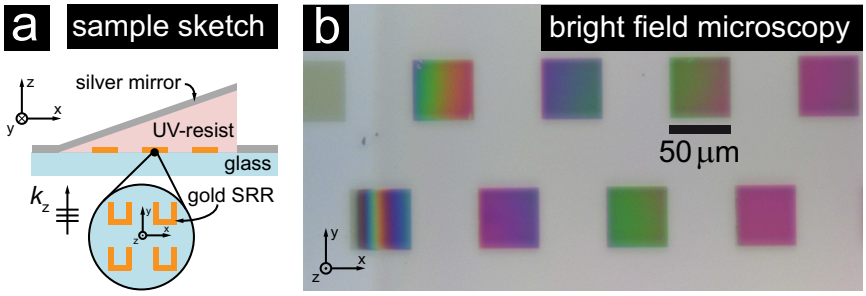

Figure 5.7: The sample sketch (a) depicts the following sample structure: lattices consisting of gold split ring resonators in a periodic arrangement on glass are separated from a silver mirror by a dielectric wedge (S1813G2 UV-resist). Under bright field illumination (b) these lattices feature a smooth color change in x-direction revealing the smooth change in lattice-mirror separation on a µm-length scale.

5.4 Experiment

Finally, we report on a pilot experiment that qualitatively reproduces features observed in the theory. These experiments were originally inspired by the proposition in Chapter 3 that the line width of a single split ring would vary as function of distance to a reflective interface, an effect that we believed would be more practically measured on arrays than on single scatterers. As the theory in this chapter shows, it is in fact impossible to measure the single particle linewidth from an array measurement. The measurement combines split rings with the wedge fabrication technique of Chapter 2 to realize a gradually varying array-reflector distance. In particular, we first fabricated split rings of 100 nm arm and base length, 30 nm height, and 70 nm gap using electron beam lithography, Au evaporation, and lift-off of a ZEP-520 e-beam resist. Next, we covered the arrays with a S1813G2 UV resist wedge by gray-scale lithography. Subsequently, the entire structure was coated with 100 nm silver. The sample structure is presented in Fig. 5.7, a together with a bright field low-magnification microscopy image Fig. 5.7, b. The silver surgace appears bright white. Periodic arrays of SRR lattices, with 150 nm periodicity are visible as darker small squares, 50 µm in size arranged in a checkerboard pattern. The wedge contour is clearly visible, coinciding with the color-onset in the second lattice from the left. The color is changing from rosé to red with increasing height of the wedge material (positive x-direction). Arrays covered by more wedge material appear darker compared to arrays covered by less wedge material.

To conduct reflectivity measurements, the sample, placed on a mechan-

ically movable (x, y)-stage, is illuminated with focused NIR-light (Nikon Plan Apo $20 \times /0.75$). A polarizer in the incoming path is aligned along x, such that the magnetic resonance condition of the split ring lattice can be realized at a certain resonance wavelength. Reflected light is collected via the same objective and sent to a fiber coupled NIR-spectrometer (Acton SP-2350i, coupled to an OMA V 1024 pixel InGaAs array). A displacement of the sample in the positive x-direction results in an increase in lattice-mirror distance. As the illumination spot size of about 5 µm diameter is ten times smaller than the lateral extend of a single lattice, we can conduct several measurements on a lattice before moving on to the next one displaced in x and y. This checkerboard arrangement additionally serves as a reference when acquiring the wedge height-profile in the profilometer as a scan along x will result in visible height dips of about 30 nm from the height difference caused by the gap of 50 µm between lattices. We plot the measured reflectivity for two different lattice pitches in Fig. 5.8, corresponding to very dense (150 nm pitch), and a more dilute (300 nm pitch) lattice. The bare split ring resonance is at around 1.6×10^{15} rad s^{-1}, i.e., around 1100 nm. This resonance wavelength is consistent with reports by de Hoogh et al. [13] who reported that the resonance of such small 100 nm sized split rings on glass shifts from 825 to 1100 nm upon capping with a high index polymer ($n = 1.65$ similar to S1613). Evidently, for the dilute lattice we retrieve a high overall reflectivity, with a set of deep minima around the single particle resonance qualitatively similar to the calculated results in Fig. 5.2 and Fig. 5.4. For the dense lattice, the reflectivity is quite different, with strong contrast across the entire spectral bandwidth, and clearly asymmetric fringes that flip asymmetry at the single particle resonance. This result is consistent with Fig. 5.4. We note that the actual densities in the experiment for the two cases are higher than in the calculation. We attribute this to the fact that the split rings in the experiment are shifted to the blue in resonance frequency as well as being less strongly scattering than assumed for the scatterers in the calculation. While being qualitatively consistent with the calculations, the measurements also point at the large difficulties in extracting the backaction effect. First, it is difficult to obtain an artifact-free measurement set since the plot is built up from spectral slices that are taken on physically different arrays. Secondly, owing to chromatic artifacts of microscope optics in this wavelength range, it would be very difficult to collect data of sufficient quality to actually *retrieve* the reflectivity of the lattice per se.

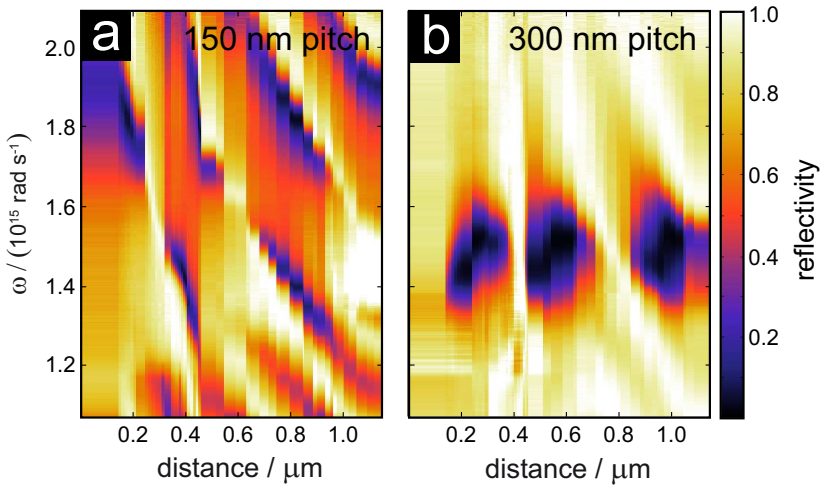

Figure 5.8: Experimental reflectivity data for split ring lattices with a pitch of (a) 150 nm and (b) 300 nm as a function of angular frequency and lattice-mirror separation. The reflectivity dips in (b) are appearing at the lattice resonance frequency around 1.5×10^{15} rad s^{-1} dissected by regions of high reflectivity. For the denser lattice (a), the low reflectivity features are highly frequency dispersive and shifted to higher frequency.

5.5 Conclusion

To conclude, we have derived a calculation method to predict the optical response of metasurfaces and particle gratings held in front of a silver interface. We have applied this model to study the backaction of the interface on the polarizability of the lattice. We conclude that while a Fabry-Pérot which takes as input the reflectivities of the substrate and lattice alone provides a reasonably satisfactory description of the joint optical response, in fact there is a surprisingly large effect of the substrate on the particle polarizability. This could significantly impact the result of such composite systems in the near field.

Finally, we note that the calculation method is easily extended to lattices embedded in any arbitrary stratified system. Indeed, for any stratified system the Green function is analytically known and always takes the form of the expression in square brackets in Eq. 5.5, albeit with different tensorial prefactor $\mathbf{M}$. However, the key point is that the difficult parallel wave vector integral always reduces to a discrete sum that is easy to evaluate. Thereby, we expect that this model will be of large utility not just for metasurface physics, but also for predicting the physics of diffractive

outcoupling structures patterned on and in LEDs and remote phosphors to improve light generation and directional extraction. Importantly, our model is not restricted to non-diffractive systems, nor to any particular incident $k_{\|}$. Thereby, it contains the full richness of grating diffraction, distributed feedback, and hybridization of lattice modes with the dispersion of any guided modes in the stratified system.

5.6 References

[1] M. Agio and A. Alù, editors, *Optical Antennas*, Cambridge University Press, Cambridge, 2013.

[2] L. Novotny and B. Hecht, *Principles of Nano-Optics*, Cambridge University Press, Cambridge, 2006.

[3] P. de Vries, D. V. van Coevorden, and A. Lagendijk, *Point scatterers for classical waves*, Rev. Mod. Phys. **70**, 447 (1998).

[4] S. Haroche, in *Les Houches Session LIII 1990, Systèmes Fondamentaux en Optique Quantique: Course 13, Cavity Quantum Electrodynamics*, Elsevier Science Publishers B.V., New York, 1992.

[5] F. J. García de Abajo, *Colloquium: Light scattering by particle and hole arrays*, Rev. Mod. Phys. **79**, 1267 (2007).

[6] R. Ameling and H. Giessen, *Cavity plasmonics: Large normal mode splitting of electric and magnetic particle plasmons induced by a photonic microcavity*, Nano Letters **10**, 4394 (2010).

[7] R. Ameling, L. Langguth, M. Hentschel, M. Mesch, P. V. Braun, and H. Giessen, *Cavity-enhanced localized plasmon resonance sensing*, Applied Physics Letters **97**, 253116 (2010).

[8] R. Ameling and H. Giessen, *Microcavity plasmonics: strong coupling of photonic cavities and plasmons*, Laser & Photonics Reviews **7**, 141 (2013).

[9] E. D. Palik, editor, *Handbook of Optical Constants of Solids*, Academic Press, London, 1998.

[10] I. Sersic, M. Frimmer, E. Verhagen, and A. F. Koenderink, *Electric and magnetic dipole coupling in near-infrared split-ring metamaterial arrays*, Phys. Rev. Lett. **103**, 213902 (2009).

[11] A. E. Miroshnichenko, S. Flach, and Y. S. Kivshar, *Fano resonances in nanoscale structures*, Rev. Mod. Phys. **82**, 2257 (2010).

[12] G. Lozano, D. J. Louwers, S. R. Rodriguez, S. Murai, O. T. Jansen, M. A. Verschuuren, and J. Gomez Rivas, *Plasmonics for solid-state lighting: enhanced excitation and directional emission of highly efficient light sources*, Light Sci Appl **2**, e66 (2013).

[13] A. de Hoogh, B. Hommersom, and A. F. Koenderink, *Wavelength-selective addressing of visible and near-infrared plasmon resonances for SU8 nanolithography*, Opt. Express **19**, 11405 (2011).

Summary

Nanoscale structures which allow for control of the emission intensity, directionality and wavelength tunability are essential for integrated optical information processing, as well as improved light emitting diodes, solar cells, and optical detectors. 'On-chip' realizations ask emitters to be incorporable with state-of-the-art processes found in today's semiconductor industry. Therefore, researchers in the field of nanophotonics are focusing on the creation of stable light sources, lossless waveguides, and highly-directional and wavelength-selective antennas. This research on the one hand requires a good understanding of 'the source', i.e., photophysics of electronic transitions and fluorophores, and on the other hand excellent control of light in passive structures through nanostructuring dielectrics and metals.

The wavelength of visible light dictates the typical length scale on which aforementioned building blocks need to be realized in an effective, reliable manner. In Chapter 2, we present a fabrication process based on gray-tone UV-lithography which allows for dielectric material to be realized in a wedge shape. Overall dimensions and surface quality of this dielectric wedge fulfill the requirements to conduct experiments following the Drexhage scheme which is a key experimental approach to calibrate photophysics of sources. Here, one is required to offer a change in the local density of photonic states (LDOS) by controlling the distance of photon sources, e.g., fluorophores or quantum dots emitting at the visible wavelength λ, to surfaces such as plain metallic mirrors or metamaterial lattices on to about $\lambda/20$. This level of accuracy allows us to measure distance dependent total decay rates of an ensemble of emitters. The total decay rate is comprised of a radiative and nonradiative part. Only the radiative decay rate is affected by a change in LDOS. As we demonstrate, our realization is feasible for effective quantification and comparison of the intrinsic quantum efficiency of different ensembles of emitters.

As fluorescence is usually dominated by electric dipole transition, the attributed LDOS is, strictly speaking, the local density of *electric field* vacuum fluctuations. This *electric field* LDOS also governs the radiative damping of purely electrically polarizable scatterers (plasmonic particles). Recently, investigation of magnetic transition dipoles in rare earth elements allowed for the observation of a *magnetic field* LDOS. That both electric *and* magnetic field LDOS can be of equal importance has been discussed in the field of thermal radiation. One archetypical object that features an electric as well as a 'spoof' magnetic response (due to its geometric shape) to driving fields is the split ring resonator (SRR)—a metamaterial building block. Such a SRR is well described as a magnetoelectric point scatterer featuring a 6×6 polarizability tensor. To quantify the strength of the electric, magnetic, and magnetoelectric response one needs to gain knowledge of all polarizability tensor components. Particularly, the cross-coupling terms are of special interest to answer the question as to how induced electric dipole moments due to driving with an electric field can in turn induce magnetic dipole moments in such a scatterer.

Following the Drexhage scheme, we examine the radiative linewidth of a SRR when varying the distance to an interface in Chapter 3. A change in the backaction of the radiated field by the scatterer on itself leads to a linewidth change and can thus serve as a calibration probe of the complex polarizability tensor. Radiation of magnetic field from an electric dipole that back-acts on a magnetic dipole is introduced via the concept of *magnetoelectric* LDOS. An experimentally accessible quantity is the extinction cross section linewidth as determined from a scattering experiment. For a magnetoelectric scatterer resonant in the microwave regime we simulate a Drexhage experiment and indeed retrieve a linewidth change that does not follow purely electric or purely magnetic LDOS indicating strong magnetoelectric cross-coupling.

The promise of unprecedented level of control of reflection, transmission and refraction of light by a planar structure composed of subwavelength scatterers that combine a strong electric and magnetic response to electromagnetic fields is the driving force in the field of metasurfaces. Any new metasurface design of, e.g., phase masks or phased array antennas requires knowledge of how exactly the collective response of two-dimensional periodic arrangements of (supposedly well understood) single building blocks comes about. Chapter 4 offers an analytical theory based on Ewald lattice summation, capable of predicting the response of diffractive as well as non-diffractive 2D periodic lattices of building blocks described within a magnetoelectric point dipole model. We show in experiment and theory how the magnetic dipole response of SRR lattices can be revealed by comparing diffraction order intensities of a lattice formed by a trivial unit cell (single-

atomic base) to a complex unit cell (two-atomic base) with alternating split ring orientation. Furthermore, we demonstrate that our calculation method not only accounts for all complex self-consistent retarded interactions in one 2D plane, but also transverse to stacked planes which form a finite 3D slab. Calculated reflection and transmission amplitudes can serve as input for retrieval algorithms that try to assign effective medium parameters for such stacked planes. Exactly how these effective parameters emerge and to what extend the spatial dispersion and bi-anisotropy is properly dealt with lies at the heart of debate in effective medium theory. We report transmission and diffraction experiments on split ring lattices. Firstly, these confirm well the developed theory. Secondly, they provide direct evidence for the magnetic nature of split rings and point at a route to avoid undesirable bi-anisotropy.

In Chapter 3, we report how the change of the environment of a single magneto-electric scatterer, e.g., by placing it in front of a mirror, affects the particle's polarizability which becomes separation dependent. Chapter 4 describes how periodic arrangements of magneto-electric scatterers cause a renormalization of their respective polarizabilities due to multiple scattering interaction with all other scatterers in the lattice. In our final Chapter 5, we address how both renormalization processes manifest themselves in the combined system of a lattice of polarizable particles above an interface. The lattice-sum formalism together with the interface Green function approach allows us to calculate the per-particle polarizability and extract reflection and transmission coefficients. Therefore, it is possible to directly compare our full analytical approach to a Fabry-Pérot model which treats the system as a mirror geometrically separated from a second interface that features a resonant response. By principle, the Fabry-Pérot model does not take near-field effects into account as solely reflection and transmission coefficients of substrate and lattice come into play. However, it provides a reasonably satisfactory description of the joint optical response. The small residual deviations can be converted back into a backaction effect in itself, however, now as a backaction correction to lattice reflectivity. We project that the notion that simple multilayer models do not describe metasurface stacks due to backaction will be very important for future metamaterial applications. Our analytical calculation method is extendable to lattices embedded in any arbitrary stratified system. Furthermore it covers non-diffractive as well as diffractive systems for arbitrary incident parallel wavevector relevant for, e.g., optimizing outcoupling structures in and on LEDs, as well as incoupling structures for solar cells.

Samenvatting

Structuren op nanometer schaal maken het mogelijk de intensiteit, richting, polarisatie, kleur, uitstraling, en absorptie van licht te manipuleren. Deze controle van intensiteit, richting en golflengte van geëmiteerd licht is essentieel voor de verwerking van optische informatie in geïntegreerde circuits, verbeterde licht emiterende dioden, zonnecellen en optische detectoren. 'On-chip'-oplossingen vragen naar nanoschaal lichtbronnen die integreerbaar zijn in moderne procestechnologie van de hedendaagse halfgeleider industrie. Om deze redenen ligt de focus voor onderzoekers in de nanofotonica op het construeren van stabiele lichtbronnen, verliesvrije golfpijpen en richtings- en golflengte-selectieve antennes. Dit onderzoeksgebied vraagd enerzijds naar een goed begrip van 'de lichtbron', dwz. fotofysica van elektronische transities in fluoroforen, zoals organische molekulen, halfgeleider quantum dots en zeldzame aard-ionen. Anderzijds is excellente controle van licht in passieve structuren door nanostructureerde dilektrica en metalen van noodzaak.

De golflengte van zichtbaar licht bepaalt de typische lengteschaal op welke de vooraf genoemde 'bouwstenen' op een effectieve, herhaalbare manier gerealiseerd moeten worden. In hoofdstuk 2 presenteren wij een fabricage procedure gebaseerd op grijs-waarde UV-litographie die het maken van dilektrische materialen met een wig-geometrie mogelijk maakt. De dimensies en oppervlakte-kwaliteit van deze diëlektrische wig voldoet aan de eisen om experimenten naar het klassieke ontwerp van Drexhage uit te kunnen voeren—een sleutel-experiment als het om het kalibreren van lichtbronnen gaat. In dit geval wordt voor een verandering van de lokale fotonische toestandsdichtheid (in het Engels: local density of states, oftewel LDOS) gezorgd door de afstand van een lichtbron, bv. fluorescente molekulen of quantum dots, die licht met de golflengte λ emitteren naar een oppervlak zoals metallische spiegels of metamateriaal roosters op $\lambda/20$ nauwkeurig in te stellen. Deze nauwkeurigheid is genoeg om afstandsafhankelijk de fluores-

cente levensduur van een ensemble van bronnen te meten. Deze levensduur is samengesteld uit een stralend en niet-stralend deel. Alleen het stralende deel wordt door een verandering in de LDOS beïnvloed. We laten zien dat onze 'manier' geschikt is voor het kwantificeren en vergelijken van intrinsieke quantum efficiënties van verschillende ensembles van lichtbronnen.

Omdat fluorescentie normaalgesproken gedomineerd wordt door elektrische dipool transities, is de bijhorende LDOS specifiek de locale toestandsdichtheid van vacuum fluctuaties van het *elektrische veld*. Dit *elektrische veld* bepaalt niet alleen de fluorescente levensduur van quantum mechanische overgangen, maar ook de stralende demping van puur elektrisch polarizeerbare verstrooiers. Een klassiek voorbeeld wordt gegeven door plasmonische deeltjes, goud of zilver nanodeeltjes met een sterke verstrooingsresonantie in het zichtbaar. Niet lang geleden leverde het onderzoek van magnetische dipoolovergangen in zeldzame aarden de observatie van *magnetisch veld* LDOS op. Dat elektrisch *en* magnetisch veld LDOS gelijkwaardige invloed op een fenomeen kunnen hebben werd ook in het vakgebied van thermische straling bediscussieerd. Een van de typische objecten die zowel elektrische als ook een effectieve ('spoof') magnetische reactie (door de geometrische vorm) op drijvende velden vertonen is de split ring resonator (SRR)—een basis element voor zogenoemde metamaterialen. Een SRR kan als magnetoelektrische punt-verstrooier met een 6×6 polarizeerbarheidstensor omschreven worden. Om de sterkte van de elektrische, magnetische en magnetoelektrische reactie te bepalen, is de kennis van alle tensor componenten noodzakelijk. Voornamelijk de kruiskoppelingsterm is interessant om de vraag te beantwoorden op welke manier elektrische dipool momenten (geïnduceerd door elektrische aandrijvende velden) magnetische dipool momenten in dit soort verstrooier kunnen induceren.

Het Drexhage idee volgend bepalen we de stralende lijnbreedte van een SRR onder variatie van de afstand naar een grensvlak in hoofdstuk 3. Een verandering in de terugkoppeling ('back-action') van het afgestraalde veld dat de verstrooier zelf uitzendt en weer terugkeert naar de strooier veroorzaakt een verandering in lijnbreedte en kan op deze manier als calibratrie voor de complexe polarizeerbaarheidstensor dienen. Afstraling van magnetische velden van een elektrische dipool die weer terugwerken op een magnetische dipool wordt door het concept van *magnetoelektrische* LDOS geïntroduceerd. Een experimenteel toegankelijke grootte is de extinctie cross-sectie lijnbreedte zoals door verstrooingsexperimenten bepaald. Voor een magnetoelektrische verstrooier resonant in het microgolf regime simuleren wij een Drexhage experiment en vinden inderdaad een lijnbreedte afhankelijkheid die niet de puur elektrische of puur magnetische LDOS volgt—indicatief voor een sterke magnetoelektrische kruiskoppeling.

De belofte van een ongekend niveau van controle voor reflectie, trans-

missie en refractie van licht door een vlakke structuur samengesteld door sub-golflengte verstrooiers die gecombineerd een sterke elektrische en magnetische reactie op elektromagnetische velden tonen is het doel van meta-oppervlakken. Ieder nieuw meta-oppervlak design, bv. fase maskers of 'phased array' antennes vraagt om kennis van het tot stand komen van de collective reactie van twee-dimensionale periodieke arrangementen van (goed begrepen) enkele bouwstenen.

Hoofdstuk 4 introduceert een analytische theorie gebaseerd op Ewald rooster sommen die geschikt is om de respons van zowel diffractieve als ook niet-diffractieve 2D-periodieke roosters van bouwstenen omschreven in een magnetoelektrisch punt dipool model te voorspellen. We laten zowel experimenteel als ook theoretisch zien hoe de magnetische dipool respons van SRR roosters te voorschijn kan komen door het vergelijken van diffractie orde intensiteiten van een rooster gebaseerd op een triviale eenheidscell (enkel-atoom basis) met een rooster gebaseerd op een complexe eenheidscell (twee-atoom basis) met alternerende split ring orientatie. Verder laten wij zien dat onze berekeningsmethode niet alleen alle complexe zelfconsistente geretardeerde interacties in één 2D vlak meetelt, maar ook transversaal op gestapelde vlakken die met elkaar uiteindelijke een 3D volume vormen. Berekende reflectie en transmissie amplitudes kunnen als uitgangspunt voor terugreken-algoritmes dienen die proberen om effectieve materiaal parameters toe te kennen aan dit soort gestapelde vlakken die een metamateriaal vormen. Op welke manier deze effectieve parameters precies verschijnen en tot hoe ver er met de ruimtelijke dispersie en bi-anisotropie rekening gehouden moet worden is een kernpunt van het debat in de theorie van effectieve medium beschrijvingen van metamaterialen. Wij stellen transmissie- en diffractie-experimenten met split ring roosters voor en stellen vast dat deze ten eerste de ontwikkelde theorie bevestigen en ten tweede een direkt bewijs voor de magnetische natuur van split rings leveren en verder laten zien op welke manier ongewenste bi-anisotropie is te voorkomen.

In hoofdstuk 3 laten wij zien hoe de verandering van de omgeving van een enkel magnetoelektrische verstrooier, b.v. door hem voor een spiegel te plaatsen, zijn polariseerbaarheid afstandsafhankelijk maakt. Hoofdstuk 4 legt uit hoe de individuele polariseerbaarheid van magnetoelektrische verstrooiers in periodieke roosters gerenormaliseerd wordt door multiple verstrooingsinteractie met alle andere verstrooiers in het rooster. In het laatste hoofdstuk 5 bespreken wij hoe beide renormalisatie stappen in een gecombineerd systeem—een rooster van polariseerbare deeltjes boven een grensvlak—optreden. Het rooster-som formalisme samen met de grensvlak-Green-functie benadering maakt het mogelijk de enkel-deeltje polariseerbaarheid te berekenen en reflectie en transmissie coefficienten te extraheren. Daardoor zijn wij in staat om onze volledig analytische, zelfconsistente be-

nadering te vergelijken met een simpel Fabry-Pérot model dat het systeem beschouwt als een spiegel nabij een gedeeltelijk transparant grensvlak met resonante respons. Het Fabry-Pérot model houdt per definitie geen rekening met respons renormalisatie door 'backaction' omdat enkel reflectie en transmissie coefficienten van het substraat en het rooster een rol spelen. Nochtans geeft het een bevredigende benadering van de gecombineerde optische respons. De kleine overgeblevene afwijkingen kunnen in een 'back-action' effect samengevat worden, in de vorm van een correctie van de reflectie van het rooster. Wij voorspellen dat de conclusie dat simpele multi-laag modellen niet strikt voldoende zijn om stapels van meta-oppervlakken te omschrijven van groot belang zal zijn voor het ontwerpen van toekomstige metamateriaal toepassingen. Onze analytische berekening is uitbreidbaar voor roosters in een willekeurig gelaagd systeem, relevant voor bijvoorbeeld uitkoppelings-structuren in en op LEDs, als ook inkoppelings-structuren voor zonnecellen.

Acknowledgments

When starting my Ph.D. research project, the AMOLF building was still brand new and moving boxes were to be found blocking hallways and offices. Luckily, this circumstance didn't prevent a good start as many experiments were already in full swing and setups ready to be used. I'm grateful for all the help provided to take my very own first steps in laser labs and cleanroom facilities at a fast pace. It is of immense value to be allowed and encouraged to gain experience right from the start—showcasing the high level of trust in students (and alarm systems in place).

AMOLF provides plenty of opportunities to discuss the latest developments of a project: coffee breaks, poster presentations, group meetings, colloquium talks. Anytime an experimental procedure or fabrication recipe turned out to be successful or a failure, experience was shared in detail. I highly value the significance given to fulfill a scientist's role as an observer—first and foremost *describing* a phenomenon without evaluation or assessment leaving the role of interpretation and putting a finding into a scientific context as a separate, second step.

The strong focus on giving presentations in a 'digestible' format for varying audiences is one of the main skills addressed in the Center for Nanophotonics; something that has given me confidence to present our work at national and international conferences. Tackling projects would not have been possible without the support from AMOLF's in-house departments: mechanical design and workshop, electronics and software design, IT-infrastructure, stockroom as well as the library service were all involved and indispensable in getting from an original idea to a published script.

I'm thankful for being given the opportunity to be involved in the 'Atelier of Light'—a space for young children to explore the phenomenon of light in a playful and creative manner. 'Thank you!' to everyone I was sharing time

with within and outside of a scientific environment to discover the cultural diversity and surprisingly different landscapes this country has to offer.